Kobe University Repository : Kernel

PDF issue: 2024-08-20

High Pressure Synthesis, Neutron Diffraction, and Metal-Insulator Transition of Iron and Ruthenium Containing Oxides

武田, 隆史

(Degree)
博士（理学）

(Date of Degree)
2000-03-31

(Date of Publication)
2015-06-19

(Resource Type)
doctoral thesis

(Report Number)
甲2088

(JaLCDOI)
https://doi.org/10.11501/3173027

(URL)
https://hdl.handle.net/20.500.14094/D1002088

※ 当コンテンツは神戸大学の学術成果です。無断複製・不正使用等を禁じます。著作権法で認められている範囲内で、適切にご利用ください。

博士論文

High Pressure Synthesis, Neutron Diffraction, and Metal-Insulator Transition of Iron and Ruthenium Containing Oxides

（鉄およびルテニウム含有酸化物の高圧合成、中性子回折と金属絶縁体転移）

平成 12 年 1 月

神戸大学大学院自然科学研究科
武田　隆史

Contents

Chapter 1

Introduction

Transition metal oxides show a wide variety of physical properties. Especially, the 3*d* transition metal oxides show various properties, because of its narrow bandwidth, electron correlation, and the influence of oxygen orbitals. Figure 1-1 shows the electronic structure of 3*d* transition metal oxides [1]. The electronic structure is controlled by coulomb energy (U), charge transfer energy (Δ) and bandwidth (W). When U is dominant, the system is Mott-Hubbard type. This applies to the early transition metals (Ti and V). On the other hand, when Δ are dominant,

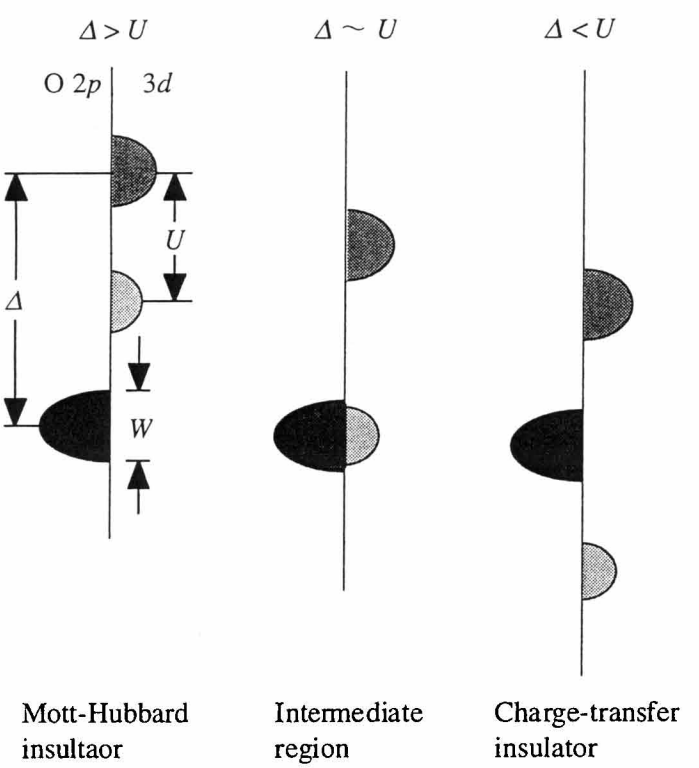

Fig. 1-1 Electronic structure of 3*d* transition metal oxides.

the system is charge-transfer type. In charge-transfer type, the oxygen can have hole and show interesting properties including superconductivity. This applies to the late transition metals (Ni and Cu). The electronic structure changes continuously from Mott-Hubbard to charge-transfer with the number of atomic number and its charge. The transition metals in the regime between Mott-Hubbard and charge-transfer also show interesting properties (charge disproportionation [2, 3], metallic ferromagnetism [4], and high-low spin transition [5]). Recently, including the freedom of spin, the freedom of orbital and lattice have attracted much attention as the origin of showing various properties and the properties which might lead to the application fields. Therefore it is very important to study the relationship between the structure and physical properties in the viewpoint of freedom and oxygen hole.

In the present study, $CaFeO_3$ (perovskite structure) and $Tl_2Ru_2O_7$ (pyrochlore structure) which have unusual properties were studied. Furthermore, the application as electrode was also studied.

Iron perovskite

The structure of transition metal oxides are composed of oxygen polyhedra which connected by corner, edge, and face sharing like perovskite, spinel, rutile, and fluorite structures. Figure 1-2 shows the cubic and orthorhombic perovskite structure. Perovskite structures are composed of metal-oxygen octahedra (BO_6) with corner sharing. In this structure, the electrical properties which range from metallic to semiconducting are related to the structural variations as follows: (i) the increase in the B-O bond length in the BO_6 octahedra, (ii) the increase in the distortion of the BO_6 octahedra, and (iii) the increases in the bend of the BO_6 zigzag chains.

The iron oxides normally contain di or trivalent iron. Some oxides synthesized under high pressure can contain tetravalent iron. Higher the oxidation state, stronger the interaction between the electron and lattice, and some interesting properties appear. $CaFeO_3$ and $SrFeO_3$ have tetravalent iron. Both oxides have

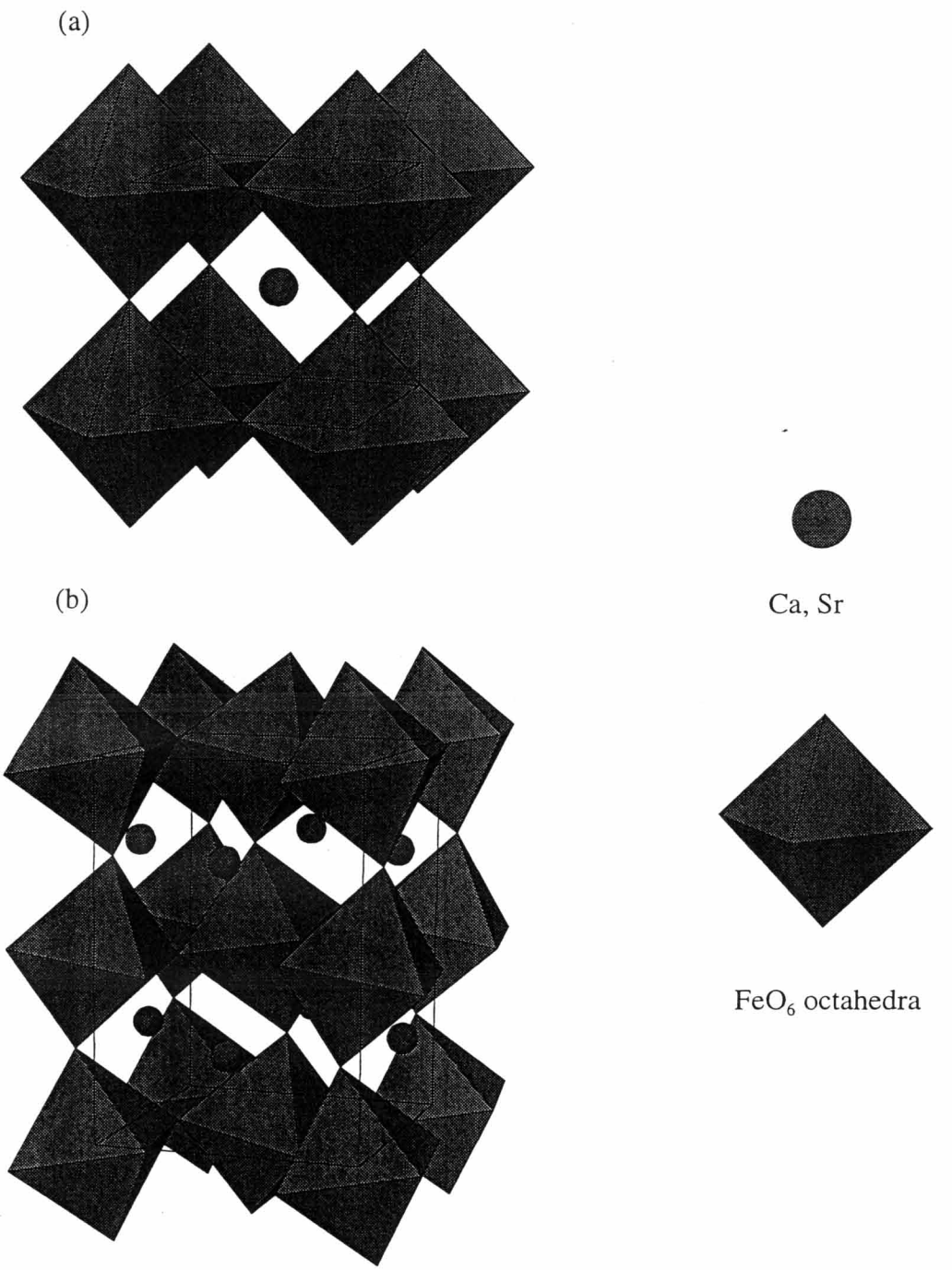

Fig. 1-2 Structure of cubic perovskite (a) and orthorhombic perovskite (b).

metallic conductivity at room temperature and show antiferromagnetic behavior [6, 7, 8]. Mössbauer studies showed tetravalent iron at room temperature, but two distinct spectra were observed at 4 K for $CaFeO_3$ [9]. Takano *et al.* proposed charge disproportionation (CD) model as follows: $2Fe^{4+} \rightarrow Fe^{3+} + Fe^{5+}$. On the other hand, $SrFeO_3$ keeps tetravalent iron to 4 K. The solid solution $Ca_{1-x}Sr_xFeO_3$ [10] was also synthesized and CD at 4 K were observed as follows: $2Fe^{4+} \rightarrow Fe^{(3+\delta)+} + Fe^{(5-\delta)+}$. $SrFeO_3$ can be synthesized under a high oxygen pressure of several hundred MPa [10]. On the other hand, the synthesis of $CaFeO_3$ requires a high oxygen pressure of 2 - 5 GPa [7]. This makes it difficult to obtain the pure sample and might be the reason why CD has not been observed in other experiment. In the present study, $Ca_{1-x}Sr_xFeO_3$ was synthesized under high oxygen pressure and the structures and physical properties especially according to CD were studied.

Thallium pyrochlore

While the 3*d* transition metal oxides show a wide variety of physical properties, 4*d* and 5*d* transition metal oxides have been thought to have less variety of physical properties because of wide bandwidth. Some oxides, however, show interesting physical properties. For example, $K_{0.3}MoO_3$ [11], $Ln_2Mo_2O_7$ (*A* = Nd, Sm, Gd) [12], and $NaWO_3$ [13] show Charge Density Wave (CDW), metallic ferromagnetism, and superconductivity, respectively. Ruthenium oxides also show interesting physical properties. Sr_2RuO_4 [14] shows superconductivity at 1.5 K and $SrRuO_3$ [15] shows metallic ferromagnetism. The Ru containing pyrochlore oxides $A_2Ru_2O_7$ show a wide variety of physical properties. $Pb_2Ru_2O_{6.5}$ [16] and $Bi_2Ru_2O_7$ [17] shows metallic and Pauli paramagnetic with resistivities of 10^{-3} Ω·cm at room temperature, and Y and rare earth pyrochlores show semiconducting properties [18, 19]. Solid solution $Bi_{2-x}Ln_xRu_2O_7$ [20] and $Bi_{2-x}Gd_xRu_2O_7$ [21] showed a change from metallic to semiconducting with dependent on substitution. The electronic structure estimated by XPS, UPS and HREELS [22, 23] showed the Pb or Bi 6*s* orbitals are close to Fermi energy (E_F). On the other hand, band calculation and UV [24] showed Pb or Bi 6*p*

orbitals are close to E_F. Although these results are against each other, it was shown that the orbitals of *A* ion affect the band structure near E_F. The relationships between structure and physical properties were reported for the solid solutions, $Bi_{2-x}Ln_xRu_2O_7$ and $Pb_{2-x}Ln_xRu_2O_{7-\delta}$ (*Ln* = Y, Pr-Lu) and the metallic-semiconducting change is related to their structural changes.

The thallium pyrochlore $Tl_2Ru_2O_7$ was first synthesized by Sleight *et al.* and it showed metallic property with nearly temperature independent resistivity [25]. Later, Jarett *et al.* reported that $Tl_2Ru_2O_{7-\delta}$ synthesized under high pressure had a metallic-semiconducting transition around 120 K [26]. They also reported the transition temperature changed with lattice parameter. However, the relationships between the structures, composition, and physical properties are not well understood. The systematic control of oxygen stoichiometry in synthesis is difficult because of the high vapor pressure of thallium oxide. The following redox-vaporization process is active above 873K: $Tl_2O_3 \rightarrow Tl_2O + O_2$. Therefore it is necessary to synthesize under high pressure in order to control oxygen stoichiometry.

The pyrochlore structure $A_2B_2O_6O'$ is derived from fluorite structure in which the special oxygen is vacant and 48*f* oxygen move to the vacancy to reduce the electrostatic repulsion between the *B* cations. In other description, pyrochlore structure can be viewed as two interpenetrating network. One is BO_6 octahedra network. The *B*-O-*B* bond angles which affect physical properties are 120-140°, which are smaller than those of the perovskite. Another network is A_2O' chain with *A* –O'-*A* angles of 109.47°. The BO_6 octahedra linkage is so strong that it is possible to form defect A and O' in pyrochlore structure, such as $A_2B_2O_6$ and B_2O_6. Some defect pyrochlores change the structure to the perovskite with pressure reflecting the lesser density. Figure 1-3 shows the two network of pyrochlore structure. There is only one oxygen positional parameter *x* for the pyrochlore structure. The *x* parameter changes from 0.3125 (perfect octahedra) to 0.375 (regular cubic) ideally. In most pyrochlores, *x* parameter shows between 0.32 and 0.34. The lattice parameter and *x* parameter determine the pyrochlore structure.

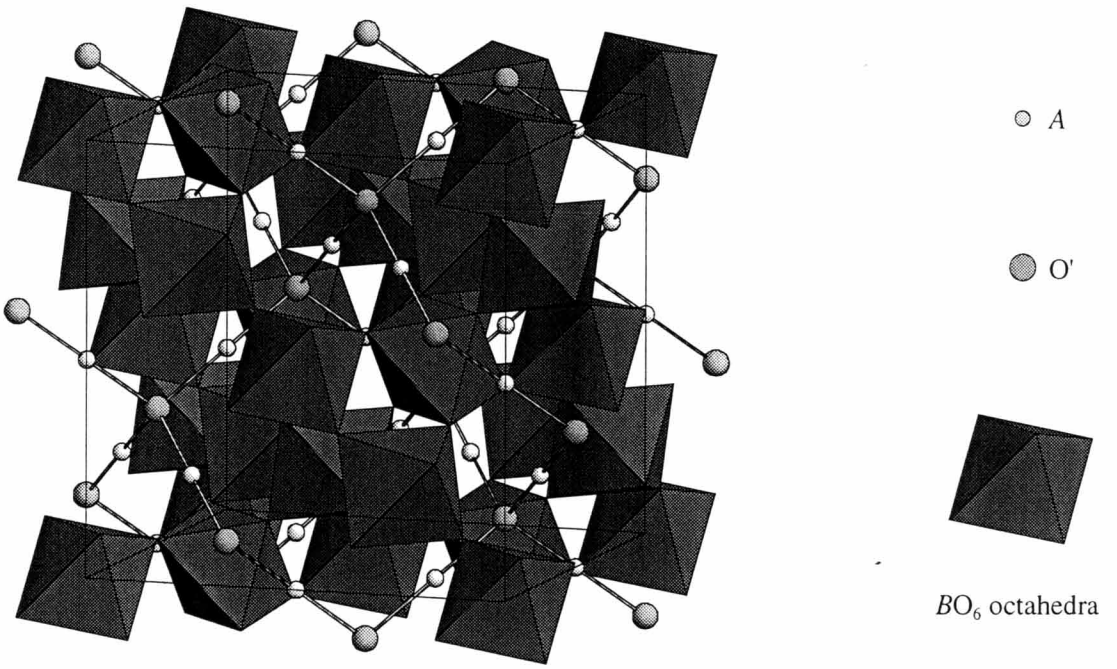

Fig. 1-3 Structure of pyrochlore $A_2B_2O_6O'$.

Pyrochlore structure can be the stage of frustrated spin system. There are two types of frustrated spin systems. One is the structurally disordered and another is the periodic lattice. The disordered alloy Fe-Au [27] is the example of a system which shows structural disorder. The 2D trirangular [28], kagomé [29] lattice, and 3D tetrahedral lattice are the examples of a periodic lattice. In pyrochlore structure, *A* (16*d*) and *B* (16*c*) ions form the tetrahedra connected by corner sharing, respectively. Figure 1-4 shows the tetrahedra network. If the exchange magnetic interaction is predominantly antiferromagnetic, the system is frustrated. This same network exists for *B* ion (16*d*) in the spinel structure AB_2O_4 [30]. Indeed some pyrochlore oxides show spin-glass like behavior [31, 32] and cluster calculation [33] also shows the spin-spin correlation length never exceed the interatomic distance. In frustrated systems, all ground states degenerate and show unusual properties such as Quantum Spin Liquid and Resonating Valence Bond (RVB) [34] which is due to quantum fluctuation effect. Therefore it is interesting to study the pyrochlore system from the viewpoint of frustration.

In the present study, thallium pyrochlore was synthesized under high pressure, and high oxygen pressure. The relationships between their structures and physical properties were studied. The structure at low temperature was also studied by low temperature neutron measurement. Furthermore, spin frustration derived from pyrochlore structure was also studied.

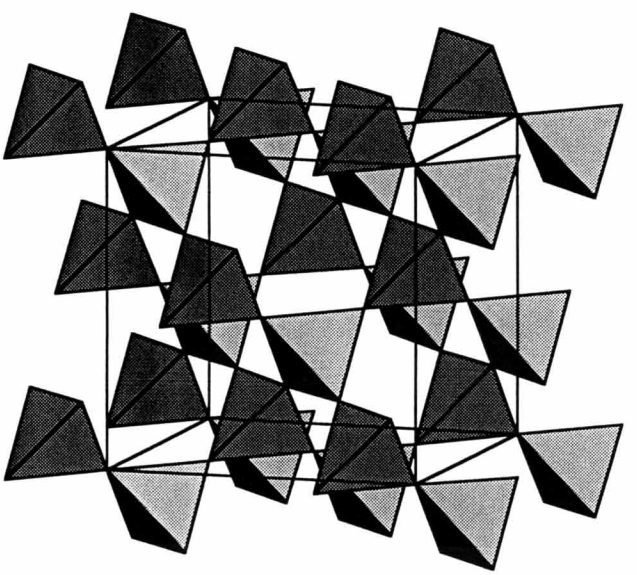

Fig. 1-4 Three dimensional network of corner sharing tetrahedra.

SOFC electrode

Transition metal oxides are also used in many application fields. Especially, dielectrics, electrodes, and catalysts are important. Transition metal can change its valence with substitution and oxide deficiency. Therefore, the catalytic activity has been studied as a substitute for rare metals.

Fuel cells have received much attention as a potentially economical, clean energy conversion system. There are several types for Fuel Cells: Phosphoric Acid Fuel Cell (PAFC), Polymer Electrolyte Fuel Cell (PEFC), Molten Carbonate Fuel Cell (MCFC), and Solid Oxide Fuel cell (SOFC). Although the concept of SOFC is simple and has high energy conversion efficiency by product heat, SOFC development is

behind other Fuel Cells. Figure 1-5 shows the operating principle of SOFC. The yttria stabilized zirconia (YSZ) is used mostly as the solid electrolyte in SOFC. The oxygen ion conductivity of YSZ become useable at high temperatures, and this limits the materials. The thermal stability, reactivity and thermal expansion are important. The transition metal oxides of the perovskite structure have been studied as cathode materials. For example, the cobalt system shows the highest conductivity and the lowest cathodic overpotential [35]. However, they reacted with YSZ to form the low-conductivity products, similarly for the manganese system [36]. Therefore, electrodes that are less reactive with YSZ and have high stability at high temperatures are required. The ruthenium pyrochlores are known as technologically important materials (catalysts [37], electrocatalysts [38], and conducting components in thick-film resistors [39]). In the present study, ruthenium pyrochlore and perovskite oxides were studied as the electrode of SOFC.

These results are described in the following chapters.

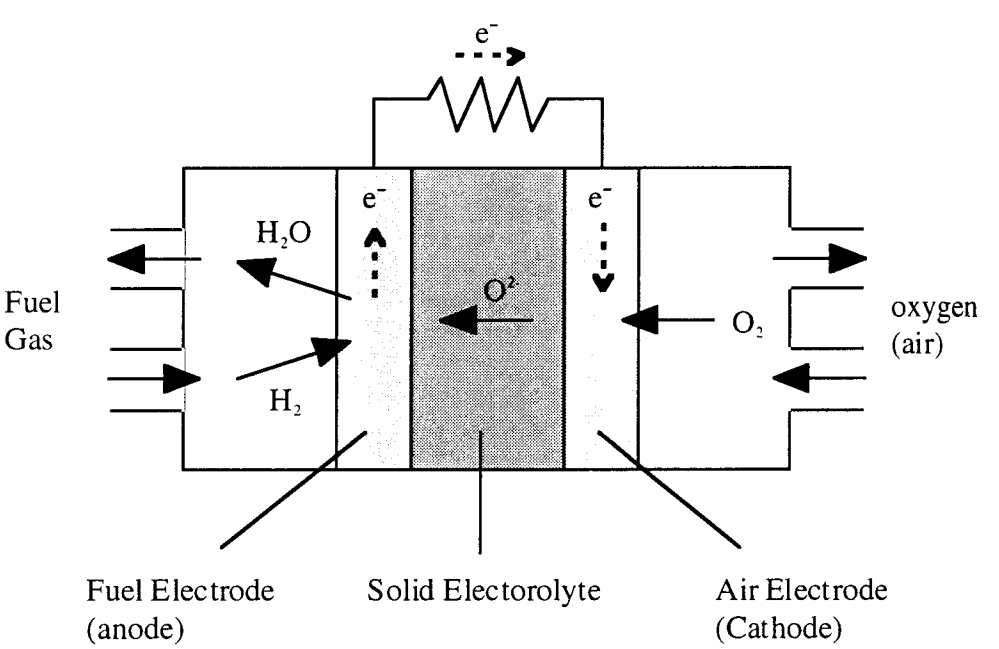

Fig. 1-5 Operating principle of SOFC.

References

[1] J. Zaanen, G. A. Sawatzky, and J. W. Allen, *Phys. Rev. Lett.*, **55**, 418 (1985)

[2] D. D. Sarma, H. R. Krisshnamurthy, Seva Nimkar, S. Ramasesha, P. P. Mitra, and T. V. Ramakrishnan, *Pramana-J. Phys.*, **38**, L531 (1992)

[3] S. E. Dann, D. B. Currie, M. T. Weller, M. F. Thomas, and D. Al-Rawwas, *J. Solid State Chem.*, **109**, 134 (1994)

[4] T. Takeda, and H. Watanabe, *J. Phys. Soc. Jpn.*, **33**, 973 (1972)

[5] W. C. Koehler, and E. O. Wolan, *J. Phys. Chem. Solids*, **2**, 100 (1957)

[6] J. B. MacChesney, R. C. Sherwood, and J. F. Poter, *J. Chem. Phys.*, **43**, 1907 (1965).

[7] F. Kanamaru, H. Miyamoto, Y. Miura. M. Koizumi, M. Shimada, and S. Kume, *Mat. Res. Bull.*, **5**, 257 (1970).

[8] Y. Takeda, S. Naka, M. Takano, T. Shinjyo, T. Takada, and M. Shimada, *Mat. Res. Bull.*, **13**, 61 (1978)

[9] M. Takano, N. Nakanishi, Y. Takeda, S. Naka, and T. Takeda, *Mat. Res. Bull.*, **12**, 923 (1977)

[10] Y. Takeda, S. Naka, and M. Takano, *J. Phys. Colloq.*, **40**, C2-331 (1979)

[11] G. Travaglini, P. Wachter, J. Marcus, and C. Schlenker, *Solid State Commun.*, **37**, 599 (1981)

[12] N. Ali, M. P. Hill, S. Labrro, and J. E. Greedan, J. Solid State Chem., 83, 178 (1989)

[13] C. Schlenker, C. Filippini, J. Marcus, J. Dumans, J. P. Pouget, and K. Kagoshima, *J. de Physique*, **C3-1757**, 44 (1983)

[14] Y. Maeno, H. Hashimoto, K. Yoshida, S. Nishizuki, T. Fujita, J. G. Bednorz, and F. Lichetenberg, *Nature*, **372**, 532 (1994)

[15] J. M. Longo, P. M. Raccah, and J. B. Goodenough, *J. Appl. Phys.*, **39**, 1327 (1968)

[16] J. M. Longo, P. M. Raccah, and J. B. Goodenough, *Mat. Res. Bull.*, **4**, 191 (1969)

[17] R. J. Bouchard, and J. L. gillson, *Mat. Res. Bull.*, **6**, 669 (1971)

[18] R. Aleonard, A. F. Berthand, M. C. Montomry, and R. Pauthenet, *J. Appl. Phys.*, **33**, 1205 (1962)

[19] A. W. Sleight, and R. J. Bouchard, NBS Spec. Publ. 364, "Solid State Chemistry",

Proceedings of 5th Materials Research Symposium" July 1972, p227

[20] A. Ehmann, and S. Kemmler-Sack, *Mater. Res. Bull.*, **20**, 437 (1985)

[21] J. B. Goodenough, A. Hamnett, and D. Telles, "Localization and Metal-Insulator Transition," (h. Fritzsche and D. Alder, Eds.), plenum, New York, 1985

[22] P. A. Cox, J. B. Goodenough, P. J. Tavener, D. Telles, and R. G. Egdell, *J. Solid State Chem.*, **62**, 360 (1986)

[23] P. A. Cox, R. G. Egdell, J. B. Goodenough, A. Hamnett, and C. C. Naish, *J. Phys. C*, **16**, 6221 (1983)

[24] W. Y. Hsu, R. V. kasowski, T. Miller, and T-C Chiang, *Appl. Phys. Lett.*, **52**, 792 (1988)

[25] A. W. Sleight and R. J. Bouchard, NBS Spec. Publ. 364, "Solid State Chemistry, Proceedings of 5th Materials Research Symposium, July 1972," p. 227.

[26] H. S. Jarrett, A. W. Sleight, J. F. Weiher, J. L. Gillson, C. G. Frederick, G. A. Jones, R. S. Swingle, D. Swartzfager, J. E. Gulley, and P. C. Hoell, "Valence Instabilities and Related Narrow-Band Phenomena" (R. D. Parks, Ed.), p. 545. Plenum, New York, 1977.

[27] V. Cannella, and J. A. Mydosh, *Phys. Rev.*, **B6**, 4220 (1972)

[28] J. N. Reimer, J. R. Dahn, J. E. Greedan, C. V. Stager, G. Liu, I. Davidson, and U. von Sacken, *J. Solid State Chem.*, **102**, 542 (1993)

[29] A. P. Ramirez, G. P. Espinosa, and A. S. Cooper, *Phys. Rev. Lett.*, **64**, 2070 (1990)

[30] D. Fiorani, J. L. Dormann, J. L. Tholence and J. L. Soubeyroux, *J. Phys. C: Solid State Phys.*, **18**, 3053 (1985)

[31] J. E. Greeden, J. N. Reimers, C. V. Stager, and S. L. Penny, *Phys. Rev.*, **B43**, 5682 (1991)

[32] J. N. Reimers, J. E. Greeden, R. K. Kremer, E. Gmelin, and M. A. Subramanian, *Phys. Rev.*, **B43**, 3387 (1991)

[33] B. Canals, and C. Lacroix, *Phys. Rev. Lett.*, **80**, 2933 (1998)

[34] P. W. Anderson, B. Halperin, and C. M. Varma, *Philos. Mag.*, **25**, 1 (1972)

[35] O. Yamamoto, Y. Takeda, R. Kanno, and M. Noda, *Solid State Ionics*, **22**, 241 (1987).

[36] Y. Takeda, R. Kanno, M. Noda, Y. Tomida and O. Yamamoto, *J. Electrochem.*

Soc., **134**, 2656 (1987).

[37] A. T. Ashcroft, A. K. Cheetham, J. S. Foord, M. L. H. Green, C. P. Grey, A. J. Murrell, and P. D. F. Vernon, *Nature*, **344**, 319 (1990)

[38] R. G. Egdell, J. B. Goodenough, A. Hamnett, and C. C. Naish, *J. Chem. Soc., Faraday Trans. 1, 79*, 873 (1983)

[39] C. E. Pike, and C. H. Seager, *J. Appl. Phys.*, **53**, 5282 (1982)

Chapter 2

Experimental

2-1 Sample preparation

2-1-1 Synthesis

The iron perovskites were synthesized by applying high oxygen pressure (2GPa) to oxygen deficient perovskites. The oxygen deficient perovskites were synthesized by heating appropriate molar ratio of starting materials $CaCO_3$ (Nakarai tesk, > 99.5% purity), $SrCO_3$ (Nakarai tesk, > 96%), α-Fe_2O_3 (Kojyundo Chemical, > 99.99%).

The ruthenium pyrochlores were synthesized under high pressure and high oxygen pressure (1 GPa) with these starting materials Tl_2O_3 (Nakarai tesk, extra pure), RuO_2 (Sumitomo Metal Mining). The other ruthenium pyrochlore was synthesized at ambient pressure, Y_2O_3 (Kojyundo Chemical, > 99.9%), Bi_2O_3 (Nakarai tesk, > 99.9%), PbO (Nakarai tesk, > 99.5%). Figure 2-1 shows a flowchart of the sample synthesis procedure.

2-1-2 High pressure synthesis

High pressure synthesis is a unique method for obtaining metastable and high pressure phases. In this study, a piston-cylinder type high pressure apparatus was used, with the sample being sealed in gold tube. The layout of the high pressure apparatus and the cell arrangement are shown in Figure 2-2. The synthesis was performed as follows; the cell was pressed to 1 - 2 GPa gradually, heated to the reaction temperature with the graphite heater, kept at temperature for 30 min, quenched to the room temperature, and released. When samples were prepared under a high oxygen pressure, $KClO_4$, was used as the oxidizing agent. The temperatures of the sample were monitored using a Pt-Rh13 thermocouple.

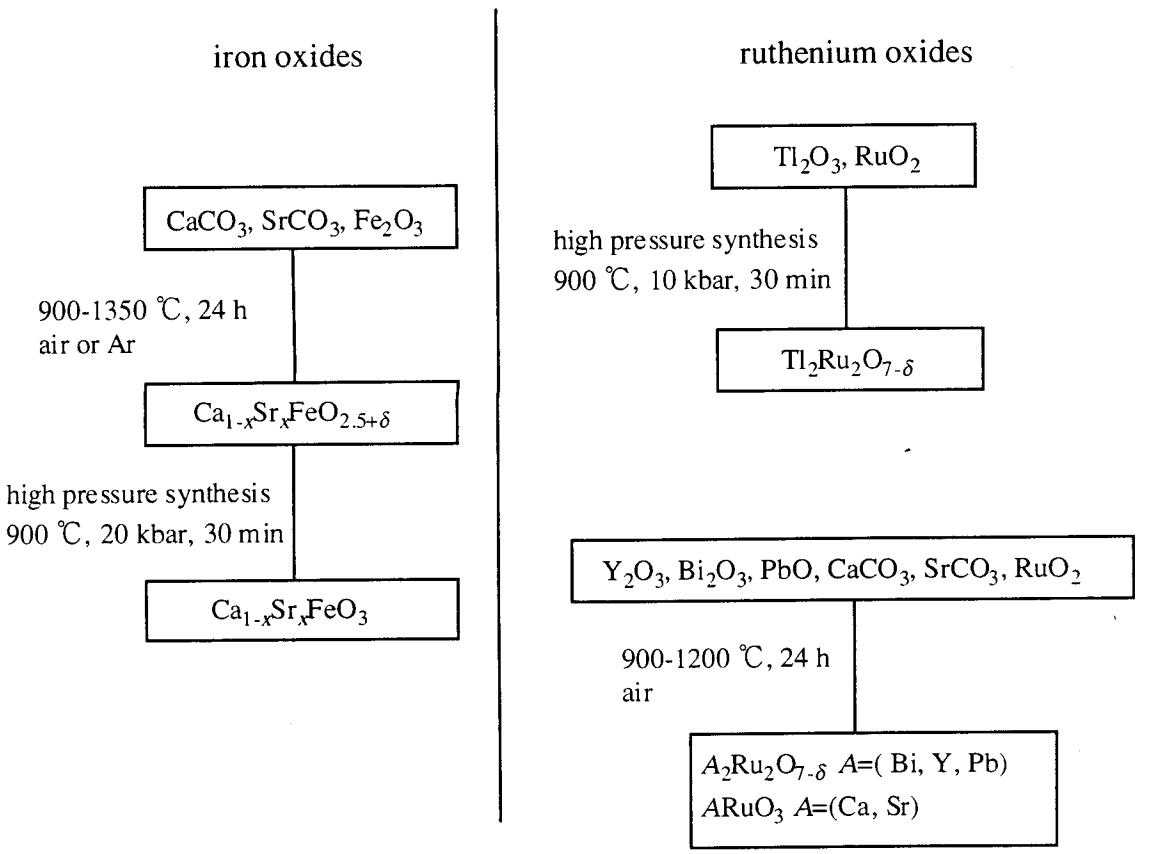

Fig. 2-1 Flowchart of synthesis.

2-2 Characterization by diffraction technique

2-2-1 X-ray diffraction measurements

X-ray diffraction measurements were used for the characterization of the samples. X-ray powder diffractometer (RIGAKU RAD-C, 12 kW rotating anode) with Cu Kα radiation was used. Diffraction data was collected for 1 s at each 0.03° step over a 2θ range of 10° to 110°.

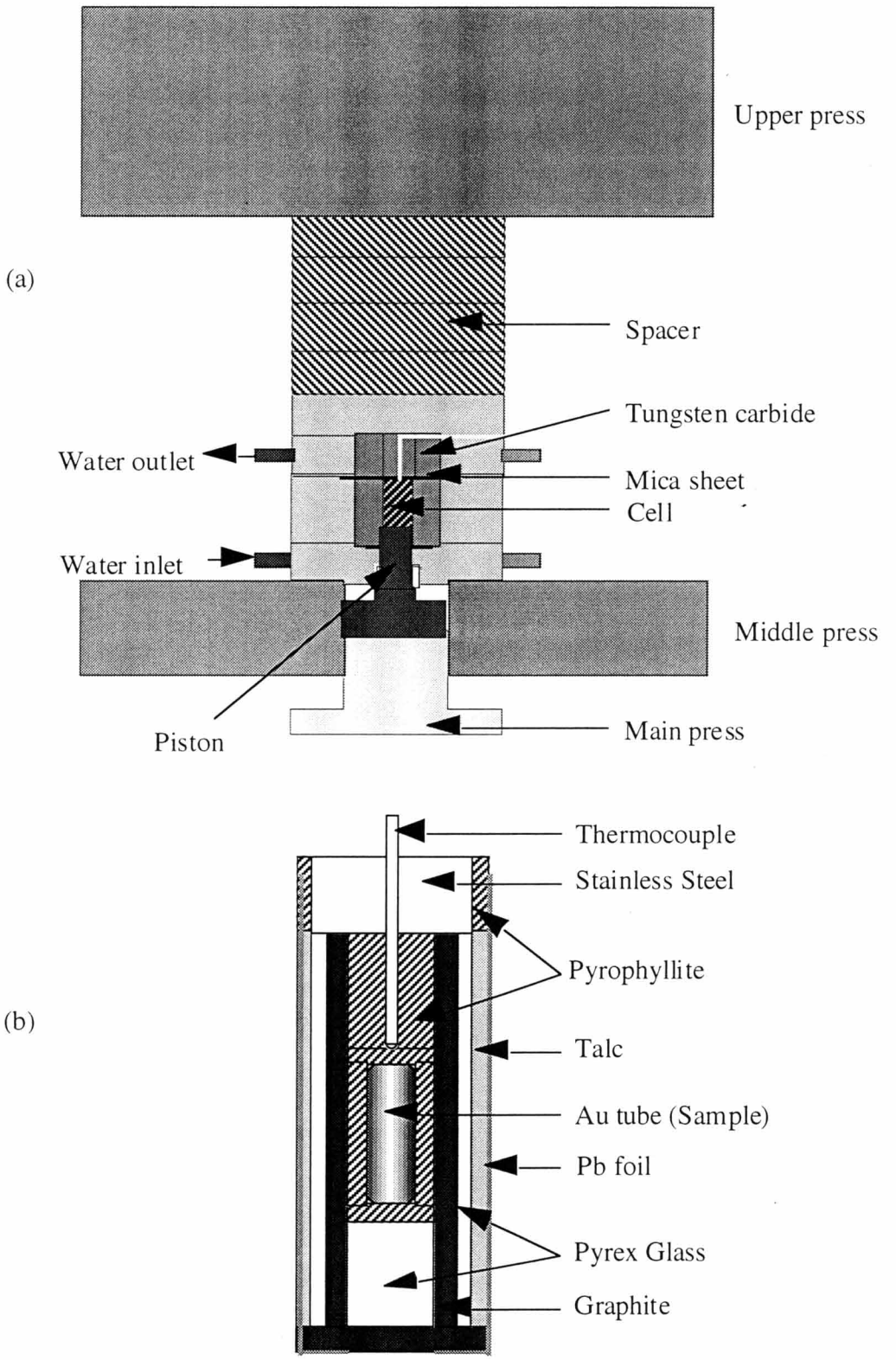

Fig. 2-2 The arrangement of (a) the piston-cylinder type high pressure apparatus, and (b) the cell for a high pressure.

2-2-2 Neutron diffraction measurements

Neutron diffraction measurements were performed to refine the structure model. Unlike X-rays which are primarily scattered by electrons, neutrons are scattered by the atomic nuclei and the scattering lengths vary irregularly with atomic number. Therefore neutrons can distinguish the atoms which have similar atomic number and small atomic number. Moreover, neutrons have a magnetic moment and magnetic structural information can be obtained. In the present study, the positions and site occupancy of oxygen and magnetic reflections have been studied.

Neutron diffraction data for the perovskites and the pyrochlores were taken on a Time-of-Flight (TOF) neutron powder diffractometer, VEGA [1], at the KENS pulsed spallation neutron source at the High Energy Accelerator Research Organization (KEK), SEPD [2], at IPNS pulsed spallation neutron source at Argonne National Laboratory in USA, and on the high resolution two-axis diffractometer, D2B [3], at the Institute Laue-Langevin (ILL) in France.

VEGA: The high energy neutrons produced in the Ta target by spallation are moderated to lower energies in solid methane moderators (20 K) surrounding the target, and moderated neutron beam is incident to the samples in vacuum through beam shutter. Time-of-flight from target to counter through samples are monitored and time-of-flight (t) are translated to planer spacing (d) by the relationship

$$d\sin\theta = \lambda / 2 = \mathrm{h}t / 2mL = t / 505.55L$$

where h, m, L are Planks constant, the neutron mass, total path length of flight from target to counter through samples, respectively. The specimen of (ca. 2 g) was contained in a cylindrical vanadium cell.

SEPD: The depleted uranium is used as target and the moderator is liquid methane (100 K). Specimen of (ca. 3 g) was used for the measurements.

D2B: The white beam of neutrons from the reactor was monochromatized to a

wavelength of 1.5949 Å with a composite focusing Ge 335 monochromator. Specimen of (ca. 1 g) was used for the measurements.

2-2-3 Rietveld analysis

Structural parameters were refined by Rietveld analysis with the computer program RIETAN97β and RIETAN96-T for the X-ray and neutron diffraction data, respectively [4], with the exception of the neutron diffraction data collect on SEPD which was fitted by the computer program GSAS [5]. The Rietveld method is a technique for refining lattice parameters and structural parameters directly from whole powder diffraction patterns without separating reflections. This method is useful (i) when single crystals cannot be grown, (ii) when only twinned samples can be prepared, and (iii) when physical and/or chemical properties of single crystal forms differ from those of polycrystalline ones.

In the Rietveld analysis, the residual S_y is minimized by a least-square refinement:

$$S_y = \Sigma\, w_i\, (y_i - y_{ci})^2$$

Where

$w_i = 1 / y_i$

y_i : observed intensity at the i th step

y_{ci} : calculated intensity at the i th step

and the sum is the overall number data points.

The calculated y_{ci} are determined from the $|F_K|^2$ values calculated from the structural model by summing of the calculated contributions from neighboring Bragg reflections plus the background:

$$y_{ci} = s\Sigma L_K |F_K|^2 \phi(2\theta_i - 2\theta_K) P_K A + y_{bi}$$

where

s : scale factor

K : Miller Indices, $h\ k\ l$, for a Bragg reflection,

L_K : Lorentz, polarization, and multiplicity factors,

Φ : reflection profile function,

P_K : preferred orientation function

A : absorption factor,

F_K : structure factor for the K th Bragg reflection,

Y_{bi} : background intensity at the i th step.

For the X-ray Rietveld analysis, reflection positions and intensities were calculated for both Cu$K\alpha_1$ and Cu$K\alpha_2$ with a factor of 0.497 applied to the calculated integrated intensities of Cu$K\alpha_2$ peaks, so that only single scale factor is obtained.

For angle-dispersive X-ray Rietveld analysis, the profile shape function is represented as the product of symmetrical profile shape function and asymmetrical profile function; a pseudo-Voigt profile shape function was used as profile shape function. The mixing parameter, g, corresponding to the ratio of the component of the Gaussian and Lorentzian functions, was included in the least-squares refinements. For TOF neutron Rietveld analysis, the sum of two exponential profile shape functions proposed by Cole and Windsor was used [6].

The Rietveld refinement process will adjust the refineable parameters until the residual is minimized. The parameters, R_{wp}, R_F, R_I, R_e, and etc, are indicators of the progress of refinemnet. Of these indicators, two indicators are important to judge whether the refinement is convoluted satisfactory. R_{wp} is the most meaningful of these R values because the numerator is the residual being minimized. Another useful numerical criterion is the goodness of fit, S (= R_{wp} / R_e). In general, a S value of 1.3 or less is usually considered to be satisfactory. Interatomic distances and bond angles are calculated from the lattice and structural parameters obtained after Rietveld analysis with the computer program ORFEE [7].

2-3 Physical property measurements

2-3-1 Electrical measurements

The electrical resistivity of the samples were measured using a DC four probe method with silver or platinum paste contacts. The temperature of the samples was measured using an AuFe thermocouple at low temperatures and Pt-Rh13 thermocouple at high temperatures, respectively. Figure 2-3 shows the arrangement of DC four-probe method. The electrical resistivities of the samples ware calculated by

$$\rho = (V/I)\ (S/l)$$

where V is a voltage across the two electrodes used for the voltage measurement, I is a constant current, S and l are a cross section area of the sample and a distance between two electrodes, respectively.

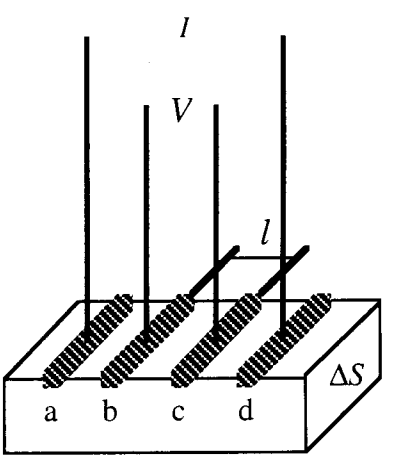

Fig. 2-3 The layout of the DC four-probe method for resistivity measurement.

2-3-2 Magnetic measurements

The magnetization was measured by a Superconducting Quantum Interference Device (SQUID) magnetometer (Quantum Design, MPMS2) between 5 and 400 K. The magnetization was measured after cooling in zero field (zfc), and then measured again down to 5 K in applied magnetic field (fc).

2-3-3 Mössbauer spectroscopy

The Mössbauer spectra were obtained using a ^{57}Co/Rh γ-ray source at room temperature for $Ca_{1-x}Sr_xFeO_3$, and low temperatures for $Ca_{0.8}Sr_{0.2}FeO_3$ and $Tl_2Ru_{1.96}{}^{57}Fe_{0.04}O_7$. The source velocity was calibrated by using pure iron metal as a standard. There are three parameters for fitting the obtained spectra (Isomer Shift (IS), Quadropole Splitting (QS), and Hyperfine Field H_{hf}). IS reflects the density of electrons, and the oxidation state of iron or degree of localization of electrons are estimated. QS shows the electrical gradient around nuclei, and the coordination state of anion or distribution of electrons are obtained. H_{hf} reflects the magnetic gradient around nuclei, and the magnitude of internal magnetic gradient or magnetic transition temperature are estimated. Figure 2-4 shows the schematic diagram of the nuclear energy level shift and splitting.

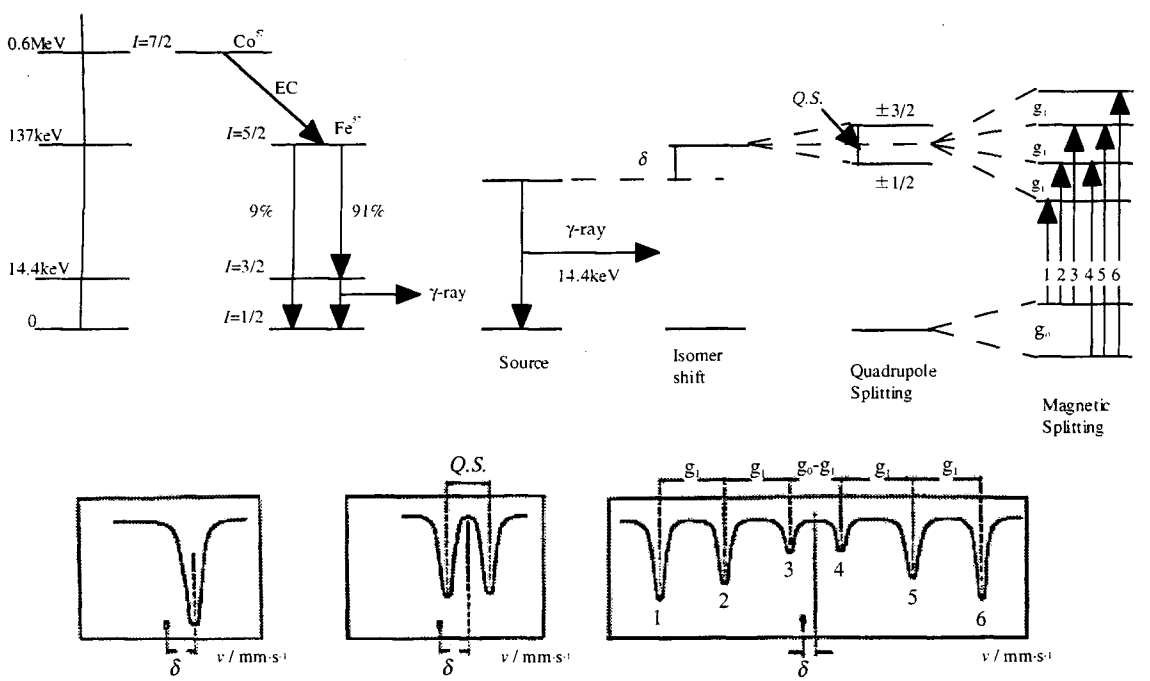

Fig. 2-4 Schematic diagram of the nuclear energy level shift and splitting as a function of (a) chemical environment, (b) electric field gradient, and (c) magnetic hyperfine field.

2-3-4 Overpotential measurements

The oxygen reduction polarization test, was prepared by heating a disk (12 mm diam, 2 mm thick) of mixed ZrO_2 and Y_2O_3 powders (from Toso, Ltd) at 1450°C for 3 h. The oxygen reduction polarization was studied on a three-electrode cell by the current interruption technique to remove the IR-drop contribution. Pyrochlore and perovskite thin films (about 3 μm thick), used as the working electrodes, were prepared on one side of the 8YSZ tablet by the RF-sputtering technique and fired at 900 - 1000°C for 2 h. Platinum paste was painted on the other side of the disk, which was divided into two parts, a counter and a reference electrode. The steady-state residual voltage (overpotential) between the working and reference was measured.

2-3-5 Thermal expansion measurements

Thermal expansion measurements were carried out from room temperature to 900°C with a Rigaku Thermoflex TAS200TM8140C using quartz as a reference. Rectangular bars of the samples were uniaxially pressed at 1500 $kg \cdot cm^{-2}$, fired at 900°C, shaped into squares using 1200 grit SiC paper and then finally fired at 900°C for 24 h.

References

[1] T. kamiyama, K. Oikawa, N. Tsuchiya, M. Osawa, H. Asano, N. Watanabe, M. Furusaka, S. Satoh, I. Fujikawa, T. Ishigaki, and F. Izumi, *Physica B*, **213-214**, 875 (1995)

[2] J. D. Jorgensen, J Faber, J. M. Carpenter, R. K. Crawford, J. R. Haumann, R. L. Hitterman, R. Kleb, G. E. Ostrowski, F. J. Rotella and T. G Worlton, *J Appl.Cryst*, **22**, 321 (1989).

[3] A. W. Hewat, *Mater. Sci. Forum*, **9**, 69 (1986)

[4] F. Izumi, "The Rietveld Method", ed. By R. A. Young, Oxford Univ. Press, Oxford, Chap. 13 (1993)

[5] A.C. Larsen and R.B. Von Dreele, Los Alamos Laboratory report, NO-LA-U-86-746 (1987).

[6] I. Cole, and C. G. Windsor, Nucl. Instrum. Methods, 171, 107 (1980)

[7] W. R. Busing, K. O. Martin, and H. A. Levy, Report ORNL-TM-306, Oak Ridge National Laboratory, Oak Ridge, TN (1964)

Chapter 3

Synthesis and properties of $Ca_{1-x}Sr_xFeO_3$

3-1 Introduction

$CaFeO_3$ was synthesized by Kanamaru *et al.* for the first time under a high oxygen pressure of 2 GPa at 1100°C, and they reported the samples to have cubic symmetry [1]. Later, Takano *et al.* synthesized $CaFeO_3$ under a pressure of 2 GPa at 1000°C and reported tetragonal symmetry and proposed charge disproportionation (CD) at 4 K, $2Fe^{4+} \rightarrow Fe^{3+} + Fe^{5+}$ [2]. Solid solution $Ca_{1-x}Sr_xFeO_3$ was also synthesized and the cubic symmetry for $x \geq 0.125$ was reported [3]. CD was observed in the following way, $2Fe^{4+} \rightarrow Fe^{(3+\delta)+} + Fe^{(5-\delta)+}$, and δ increaed to unity with Sr substitution, which means no CD was observed for $SrFeO_3$. $SrFeO_3$ was first synthesized by Gallagher *et al.* under a high oxygen pressure of 34.4 MPa at 760°C and results of Mössbauer studies were presented [4]. Later, Machesney reported metallic conductivity and antiferromagnetic behavior [5]. Neutron diffraction measurement for $SrFeO_3$ showed the screw type antiferromagnetic structure with a propagation vector parallel to the <111> direction [6]. Although many studies about structure, magnetic and electrical properties were reported for the end member $SrFeO_3$, $CaFeO_3$ and $Ca_{1-x}Sr_xFeO_3$ have not studied thoroughly reflecting the difficulties of synthesis. Recently, Morimoto *et al.* measured synchrotron X-ray diffraction for $CaFeO_3$, and reported the orthorhombic symmetry [7]. However no structural information for $CaFeO_3$ was reported. Furthermore, the changes of physical properties accompanied by CD have not been reported.

In the present study, $Ca_{1-x}Sr_xFeO_3$ was synthesized under high oxygen pressure, and their structures were determined by X-ray Rietveld analysis. The relationships between physical properties and structures were also studied.

3-2 Synthesis

The starting materials $CaCO_3$, $SrCO_3$, and α-Fe_2O_3 were mixed, pelleted, and calcined at 900 °C for 24 h. Then the pellets were reground, and pelleted, and fired at

1100 - 1350°C for 24 h in air or Ar. Figure 3-1 shows the formation diagram of the oxygen deficient perovskite $Ca_{1-x}Sr_xFeO_{2.5+\delta}$. When the samples were synthesized in air, brownmillerite and perovskite phase appeared in $0.0 \leq x \leq 0.2$ and $0.8 \leq x \leq 1.0$, respectively. The oxygen vacancies are ordered in the brownmillerite phase and disordered in perovskite phase as shown in Figure 3-2. In the region of $0.4 \leq x \leq 0.6$, two phases with the brownmillerite and the perovskite were observed. However, single phase brownmillerite was obtained for the samples synthesized in Ar above 1350 °C even for the composition region of $0.4 \leq x \leq 0.6$. Finally, the $Ca_{1-x}Sr_xFeO_{2.5+\delta}$ with the brownmillerite structure was obtained for the whole range of solid solution, $0.0 \leq x \leq 1.0$.

High-oxygen pressure treatments under 2 GPa using $KClO_4$ were carried out for samples with the brownmillerite phase and a mixture of brownmillerite and perovskite phases. However, oxygen deficient phase, which was detected by Mössbauer study, remained even after the high oxygen pressure treatment when the mixed phases were used as the starting materials. In order to obtain monophase samples of the perovskite phase, it is necessary to use the brownmillerite phase. In the brownmillerite structure, the oxygen vacancies are known to order in alternate (001) FeO_4 planes of the cubic perovskite structure, with alternate <110> rows of oxygens removed. This type of structure makes it easier to form the stoichiometric perovskite probably because of high oxygen diffusion in the oxygen vacancy row.

Figure 3-3 shows the X-ray diffraction patterns for the whole range of solid solution $Ca_{1-x}Sr_xFeO_3$ after the high oxygen pressure treatment, at room temperature. The diffraction patterns of $SrFeO_3$ were indexed by a cubic cell with a = 3.85 Å and space group $Pm\bar{3}m$, while in $CaFeO_3$, superlattice reflections were obviously observed which could be indexed by an orthorhombic cell with space group *Pnma*. X-ray diffraction patterns between 38° and 42° are also indicated in Figure 3-4. The superlattice reflection 221 which is indicative of the orthorhombic *Pnma* was recognized for $0.0 \leq x \leq 0.6$. The peak shifted to lower angles from $x = 0.0$ to $x = 0.5$ and remained constant at $x = 0.6$. The orthorhombic 220 reflection which is equivalent to the cubic 111 reflection shifted to lower angles from $x = 0.0$ to $x = 1.0$ continuously. Theses results indicate two phases with orthorhombic and cubic symmetry at $x = 0.6$.

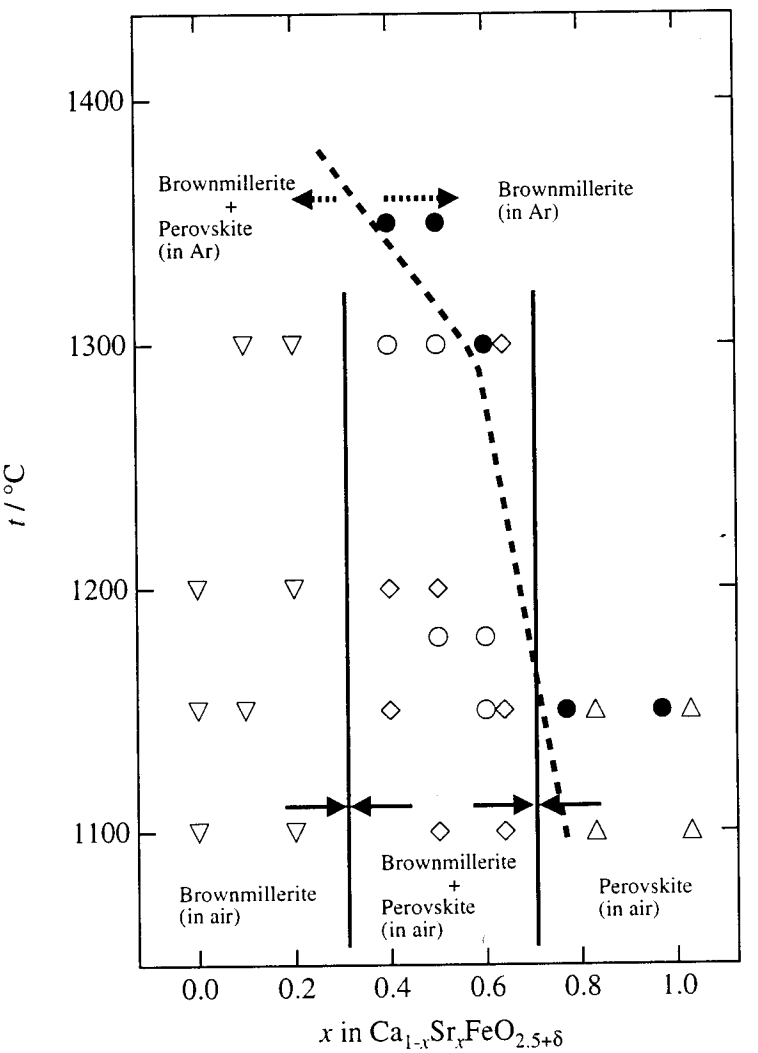

Fig. 3-1 Formation diagram of $Ca_{1-x}Sr_xFeO_{2.5+\delta}$.

▽ : brownmillerite phase (synthesized in air)

◇ : brownmillerite and perovskite phases (synthesized in air)

△ : perovskite phase (synthesized in air)

○ : brownmillerite and perovskite phases (synthesized in Ar)

● : brownmillerite phase (synthesized in Ar)

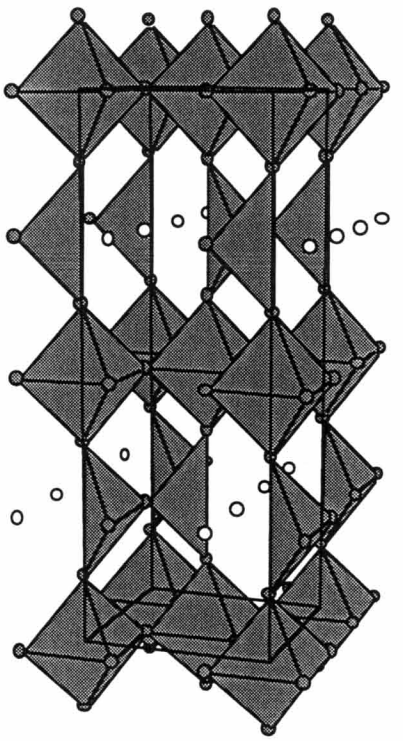

brownmillerite structure

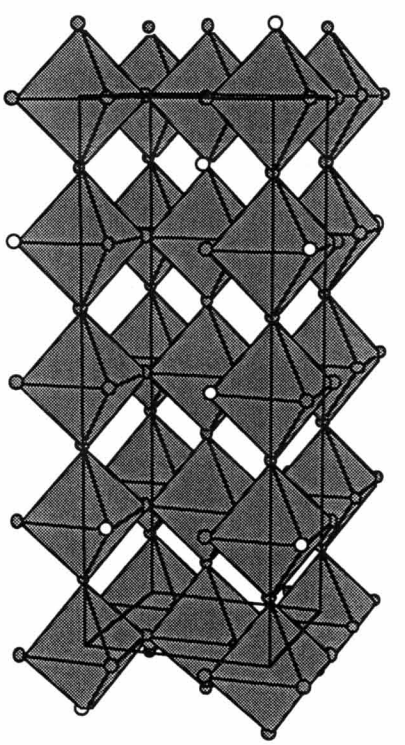

perovskite structure

Fig. 3-2 The brownmillerite structure and perovskite structure for $Ca_{1-x}Sr_xFeO_{2.5+\delta}$.

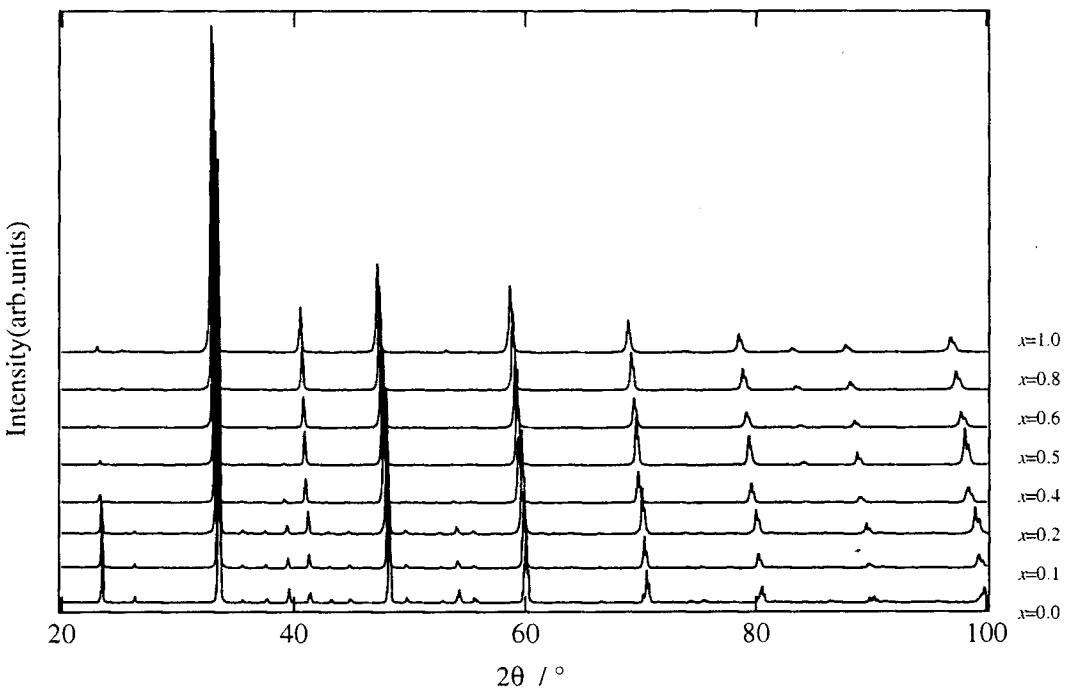

Fig. 3-3 X-ray diffraction patterns for $Ca_{1-x}Sr_xFeO_3$.

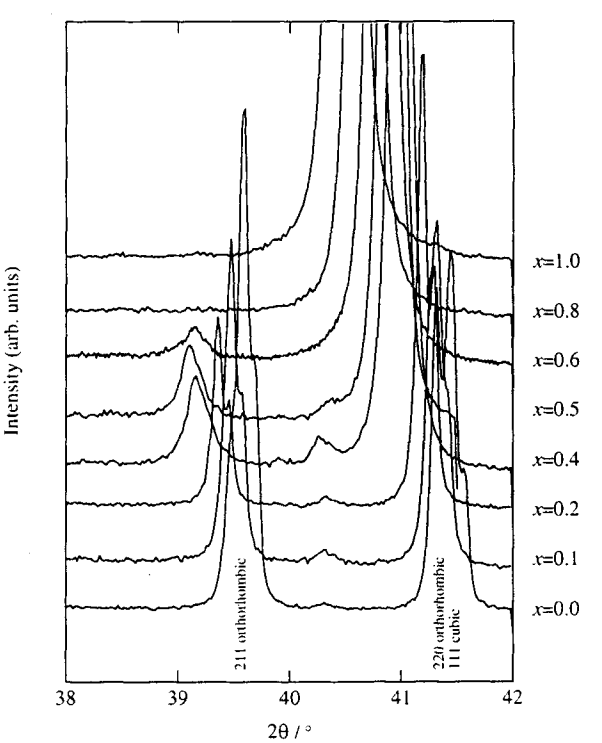

Fig. 3-4 X-ray diffraction patterns for $Ca_{1-x}Sr_xFeO_3$ between 38° and 42°.

Figure 3-5 shows the composition dependence of the lattice parameters of $Ca_{1-x}Sr_xFeO_3$ obtained from Rietveld analysis. The orthorhombic distortion decreased with increasing x from 0.0 to 0.5, and the lattice parameters increased with substituting larger cation Sr (ionic radii Ca^{2+}(XII) = 1.34 Å, Sr^{2+}(XII) = 1.44 Å) [8].

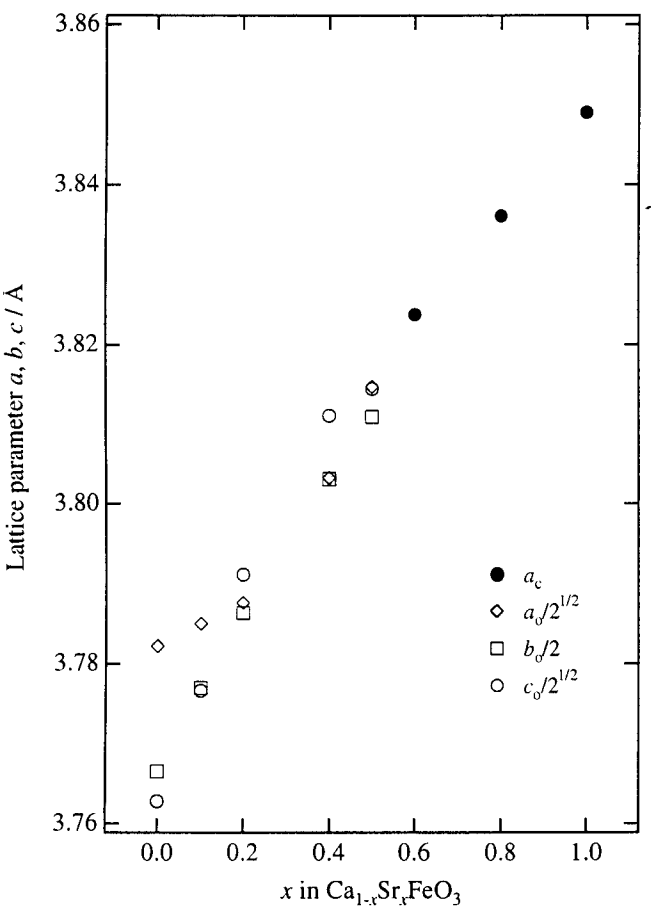

Fig. 3-5 Composition dependence of lattice parameters for $Ca_{1-x}Sr_xFeO_3$. The value obtained for x = 0.6 in the region of mixture of two phases was refined with space group $Pm\bar{3}m$.

3-3 Structure

Refinement of the structure was performed with space group *Pnma* for the sample with $0 \leq x \leq 0.5$, and $Pm\bar{3}m$ for $0.8 \leq x \leq 1.0$. Initial coordinates were taken as follows: *Pnma*, Ca(Sr) 4*c* (x, 1/4, z); Fe 4*b* (0, 0, 1/2); O(1) 8*d* (x, y, z); O(2) 4*c* (x, 1/4, z), and $Pm\bar{3}m$ Ca(Sr) 1*a* (0, 0, 0); Fe 1*b* (1/2, 1/2, 1/2); O 3*c* (1/2, 1/2, 0). The refinement was done in stages with the atomic coordinates and thermal parameters fixed in the initial calculations and subsequently allowed to vary only after the scale, background, halfwidth, and unit-cell parameters had converged to their optimum values. During the later stage of the refinements, when temperature factors were refined, the B_{eq} had to be constrained to the same value, otherwise the refinement was unstable. Table 3-1 lists final R factors, structural parameters and their estimated deviations. Table 3-2 gives interatomic distances and bond angles calculated with ORFFE. Figure 3-6 shows composition dependence of the interatomic distances and bond angles. Ideal cubic perovskite has equal twelve *A*-O distances. The twelve *A*-O distances split into the two group of eight short and four long distances and the difference between two groups becomes larger with decreasing x. On the other hand, no significant change was found for the Fe-O distances. The Fe-O-Fe angle increases from 163° to 180° with increasing x, which indicates that the bend in the zig-zag chains formed by the FeO_6 octahedra connected by corner sharing, increases with x. No significant deviation from 90° for the O-Fe-O angles and no significant changes in Fe-O distances indicate no distortion of the FeO_6 octahedra.

Table 3-1 X-ray Rietveld refinement results for $Ca_{1-x}Sr_xFeO_3$

	x=0.0	x=0.1	x=0.2	x=0.4	x=0.5
a (Å)	5.34852(12)	5.35283(17)	5.3566(2)	5.3786(2)	5.395(2)
b (Å)	7.53388(18)	7.5540(2)	7.5724(3)	7.6062(3)	7.6218(3)
c (Å)	5.32141(12)	5.34100(14)	5.3612(2)	5.3896(2)	5.394(2)
Ca(Sr)					
x	0.03445(9)	0.0291(8)	0.0236(9)	0.0104(12)	0.000(3)
y	1/4	1/4	1/4	1/4	1/4
z	-0.005(3)	-0.005(3)	-0.001(4)	-0.000(3)	0.000(9)
B (Å^2)	1.55(12)	1.70(9)	0.89	1.13(6)	0.45(9)
Fe					
x	0	0	0	0	0
y	0	0	0	0	0
z	1/2	1/2	1/2	1/2	1/2
B (Å^2)	1.01(9)	1.66(8)	0.63(10)	1.13	0.40
O(1)					
x	0.286(5)	0.282(4)	0.273(7)	0.261(7)	0.24(2)
y	0.033(3)	0.022(3)	0.024(4)	0.026(3)	-0.011(10)
z	0.717(3)	0.716(3)	0.716(5)	0.720(3)	0.76(2)
B (Å^2)	1.4(4)	1.5(4)	0.7(2)	1.13	1.3(2)
O(2)					
x	0.492(3)	0.503(3)	0.505(3)	0.497(4)	0.483(12)
y	1/4	1/4	1/4	1/4	1/4
z	0.079(5)	0.072(5)	0.061(9)	0.040(8)	0.032(18)
B (Å^2)	0.9(6)	1.5(6)	0.7	1.13	1.3
R_{wp}	10.39	11.35	14.31	14.87	14.37
R_e	8.80	9.72	9.28	11.18	10.00
R_I	3.83	3.08	4.40	5.56	7.73

	x=0.8	x=1.0
a (Å)	3.83606(8)	3.84990(7)
Ca(Sr)		
x	0	0
y	0	0
z	0	0
B (Å^2)	0.92(17)	0.86(18)
Fe		
x	1/2	1/2
y	1/2	1/2
z	1/2	1/2
B (Å^2)	0.92	0.6(2)
O		
x	1/2	1/2
y	1/2	1/2
z	0	0
B (Å^2)	0.92	0.8(5)
R_{wp}	15.42	16.71
R_e	12.46	12.21
R_I	3.25	2.90

Table 3-2 Interatomic distances (Å) and angles (°) for $Ca_{1-x}Sr_xFeO_3$

	x=0.0	x=0.1	x=0.2	x=0.4	x=0.5
Ca(Sr)-O(1) (×2)	2.378(12)	2.443(15)	2.46(2)	2.47(2)	2.67(5)
Ca(Sr)-O(1) (×2)	2.600(13)	2.578(17)	2.62(2)	2.71(2)	2.79(5)
Ca(Sr)-O(1) (×2)	2.612(12)	2.648(16)	2.65(2)	2.64(2)	2.61(5)
Ca(Sr)-O(1) (×2)[a)]	3.139(12)	3.066(15)	3.03(2)	2.97(2)	2.72(5)
Ca(Sr)-O(2)	2.32(2)	2.32(3)	2.36(5)	2.48(4)	2.52(7)
Ca(Sr)-O(2)	2.485(12)	2.573(15)	2.60(2)	2.63(2)	2.62(7)
Ca(Sr)-O(2)[a)]	2.923(12)	2.844(14)	2.80(2)	2.77(2)	2.79(7)
Ca(Sr)-O(2)[a)]	3.02(2)	3.03(3)	3.03(2)	2.91(4)	2.87(7)
Fe-O(1) (×2)	1.917(12)	1.91(2)	1.87(4)	1.85(4)	1.90(16)
Fe-O(1) (×2)	1.927(12)	1.92(2)	1.96(4)	1.99(3)	1.92(16)
Fe-O(2) (×2)	1.920(4)	1.928(6)	1.921(8)	1.913(5)	1.915(9)
O(1)-Fe-O(2)	89.4(7)	88.5(9)	89.9(19)	91.8(18)	87(4)
O(1)-Fe-O(2)	91.1(8)	91.5(9)	90.3(2)	90.4(2)	90.1(3)
O(1)-Fe-O(1)	90.65(14)	90.3(2)	87(2)	88.8(18)	89(4)
Fe-O(1)-Fe	157.4(12)	161.8(8)	163.1(15)	164.6(18)	174.2(4)
Fe-O(2)-Fe	157.8(6)	156.8(16)	160(3)	167(2)	168(5)

a) Long Ca(Sr)-O distances

	x=0.8	x=1.0
Ca(Sr)-O (×12)	2.7127(1)	2.7217(1)
Fe-O (×6)	1.9182(1)	1.9246(1)
O-Fe-O	90	90
Fe-O-Fe	180	180

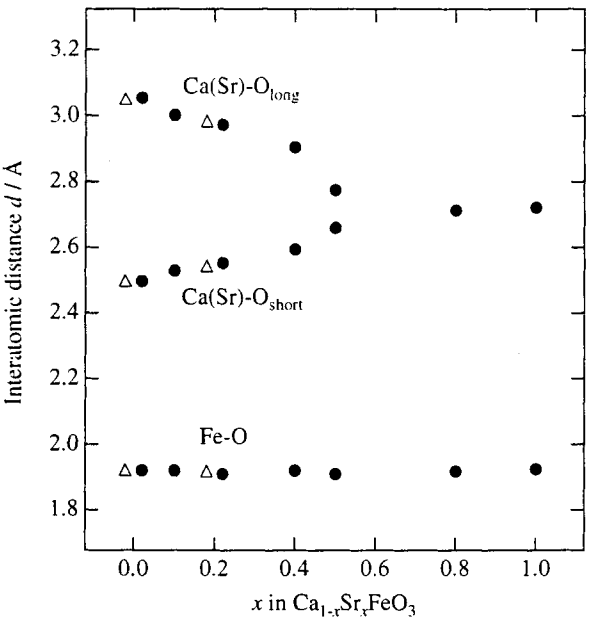

Fig. 3-6(a) Composition dependence of the interatomic distances for $Ca_{1-x}Sr_xFeO_3$. The values determined by the neutron diffraction results are indicated in the same figures (●:X-ray, △:neutron).

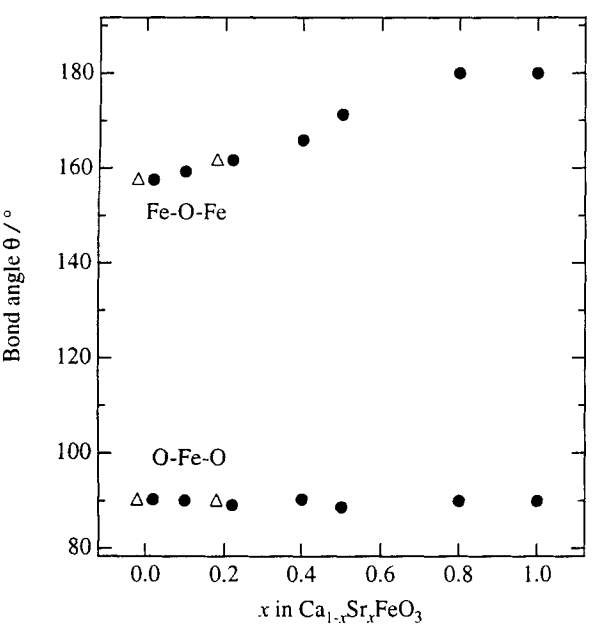

Fig. 3-6(b) Composition dependence of the interatomic angles for $Ca_{1-x}Sr_xFeO_3$. The values determined by the neutron diffraction results are indicated in the same figures (●:X-ray, △:neutron).

3-4 Mössbauer spectroscopy

Mössbauer spectra of $Ca_{1-x}Sr_xFeO_3$ were recorded at room temperature to study the oxidation state of iron. Figure 3-7 shows the spectra. The data were fitted by using Lorentian lines. Figure 3-8 illustrates isomer shift and full-width-at-half-maximum (FWHM) of the Mössbauer spectra. A sharp spectra with the isomer shift (0.043 $mm \cdot s^{-1}$ - 0.066 $mm \cdot s^{-1}$) is indicative of Fe^{4+} state with the value of isomer shift (0.054 $mm \cdot s^{-1}$) reported previously [4]. At intermediate range ($0.1 < x < 0.8$), the lines became broader, which is attributed to the local inhomogeneous distribution of Ca and Sr. Isomer shift increased from 0.043 $mm \cdot s^{-1}$ to 0.070 $mm \cdot s^{-1}$ with increasing x from 0.0 to 1.0 by substituting Sr for Ca.

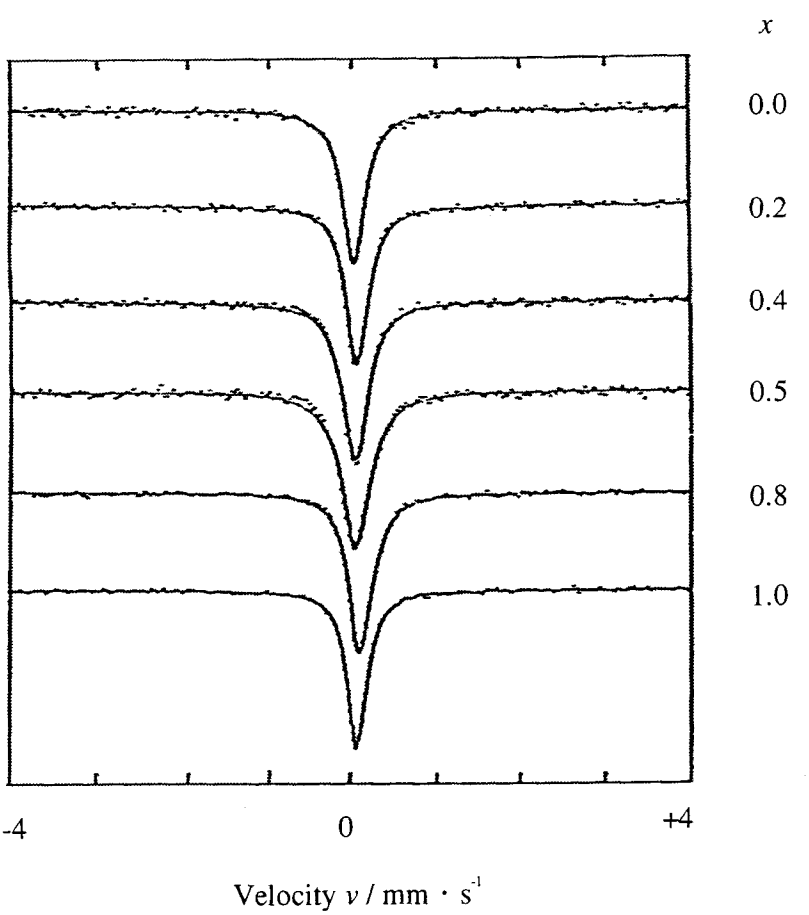

Fig. 3-8 Mössbauer spectra at room temperature for $Ca_{1-x}Sr_xFeO_3$.

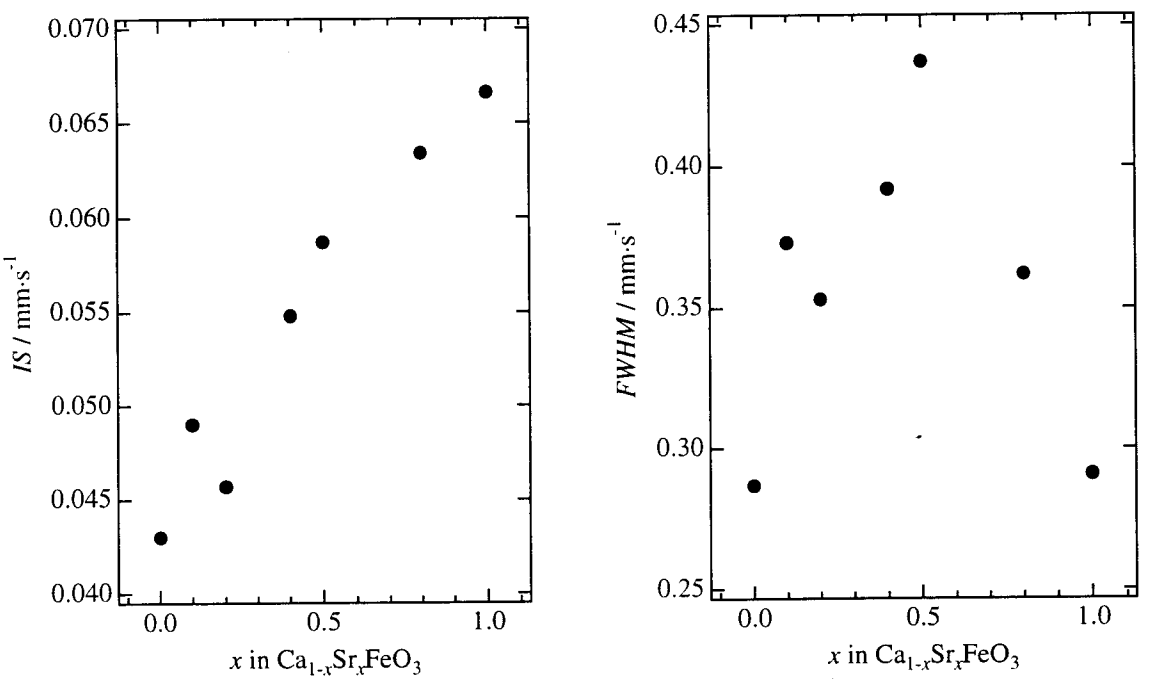

Fig. 3-7 Composition dependence of isomer shift and FWHM for $Ca_{1-x}Sr_xFeO_3$.

Previously the CD was observed in the low-temperature Mössbauer spectra measured for $CaFeO_3$ in the temperature range 4 – 300 K [9]. The spectra showed two peaks at 290 K and the splitting of the peaks became larger with decreasing temperature. This result indicated the CD begins at 290 K for $CaFeO_3$, and the oxidation states change continuously: $2Fe^{4+} \rightarrow Fe^{(3+\delta)+} + Fe^{(5-\delta)+}$. To clarify the CD of the solid solution, $Ca_{1-x}Sr_xFeO_3$, the spectra at 130 – 300 K was measured for x = 0.2 ($Ca_{0.8}Sr_{0.2}FeO_3$). Figure 3-9 shows the temperature dependence of the Mössbauer spectra. As the temperature decreased from 300 K, the linewidth became broad, two peaks were obviously observed below 215 K, and an antiferromagnetic pattern was observed at 127 K. Figure 3-10 shows the differences in isomer shift between the two peaks by fitting in two Lorentian lines with the same intensity. Splitting of the peaks

were observed at 240 K. The splitting increased with decreasing temperature, and became saturated around 150 K. The difference of the two peaks (0.28 $mm \cdot s^{-1}$) is smaller than that of $CaFeO_3$ (0.32 $mm \cdot s^{-1}$ at 4 K). These results indicate that the localization of σ^* band arising from Fe-e_g and O-2p band starts gradually from 240 K.

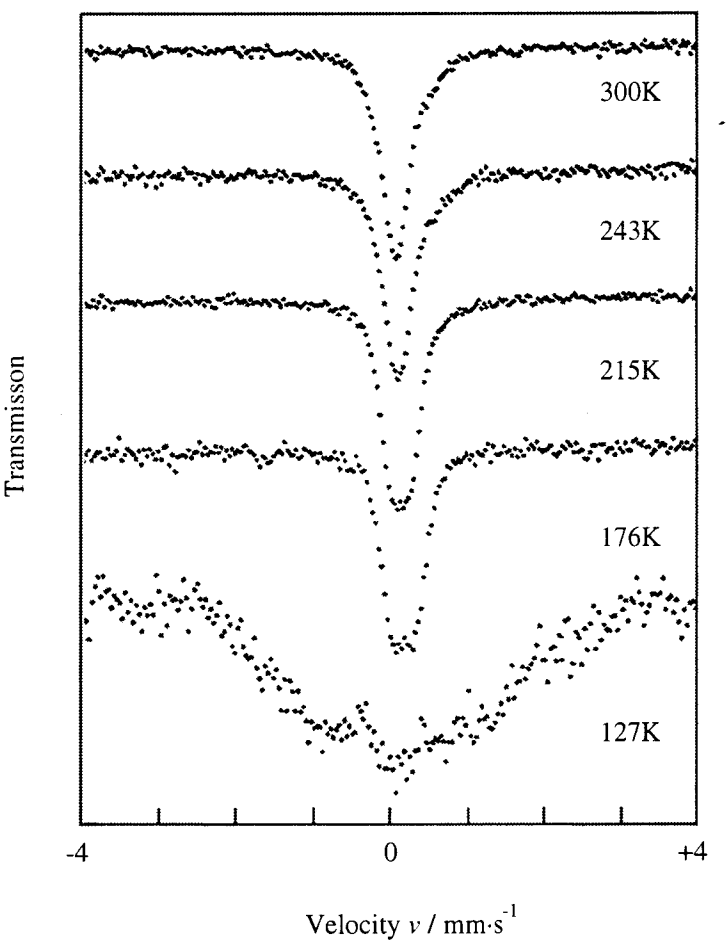

Fig. 3-9 Mössbauer spectra at low temperatures for $Ca_{0.8}Sr_{0.2}FeO_3$.

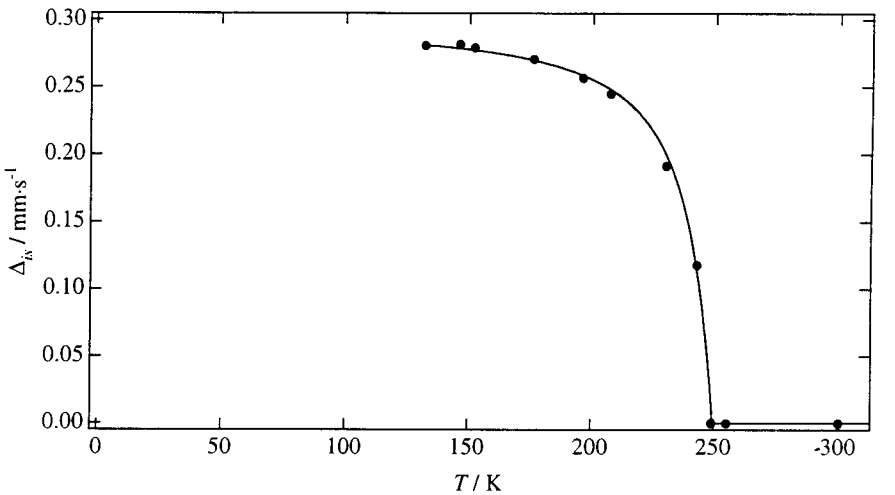

Fig. 3-10 Temperature dependence of the differences in isomer shift between the two isomer shift for $Ca_{0.8}Sr_{0.2}FeO_3$.

3-5 Electrical property

Figure 3-11 shows the temperature dependence of the electrical resistivity for $Ca_{1-x}Sr_xFeO_3$. At x = 0.0 ($CaFeO_3$) and x = 0.2 ($Ca_{0.8}Sr_{0.2}FeO_3$), the slope of the resistivity curve changed at 290 and 240 K, respectively, indicating a metallic-semiconducting transition. The transition temperature corresponds to the CD observed by Mössbauer spectra. The transition temperature observed by the resistivity measurements decreased from 290 to 200 K with increasing x, and no slope change in the resistivity curve was observed at x = 0.8. These slope changes correspond to the beginning of CD. On the other hand, the sample with x = 1.0 ($SrFeO_3$) showed metallic property. The structural changes that the Fe-O-Fe angle increases with x in $Ca_{1-x}Sr_xFeO_3$ are well consistent with the electrical property changes from semiconducting to metallic. The effect of larger Fe-O-Fe angles is to increase the overlap between Fe 3*d* and O 2*p* orbital. The relationships between the structure and physical properties of the $GdFeO_3$-type structures are reported. The structures are composed of framework corner-sharing MO_6 octahedra, and the variation of the *M*-O-*M*

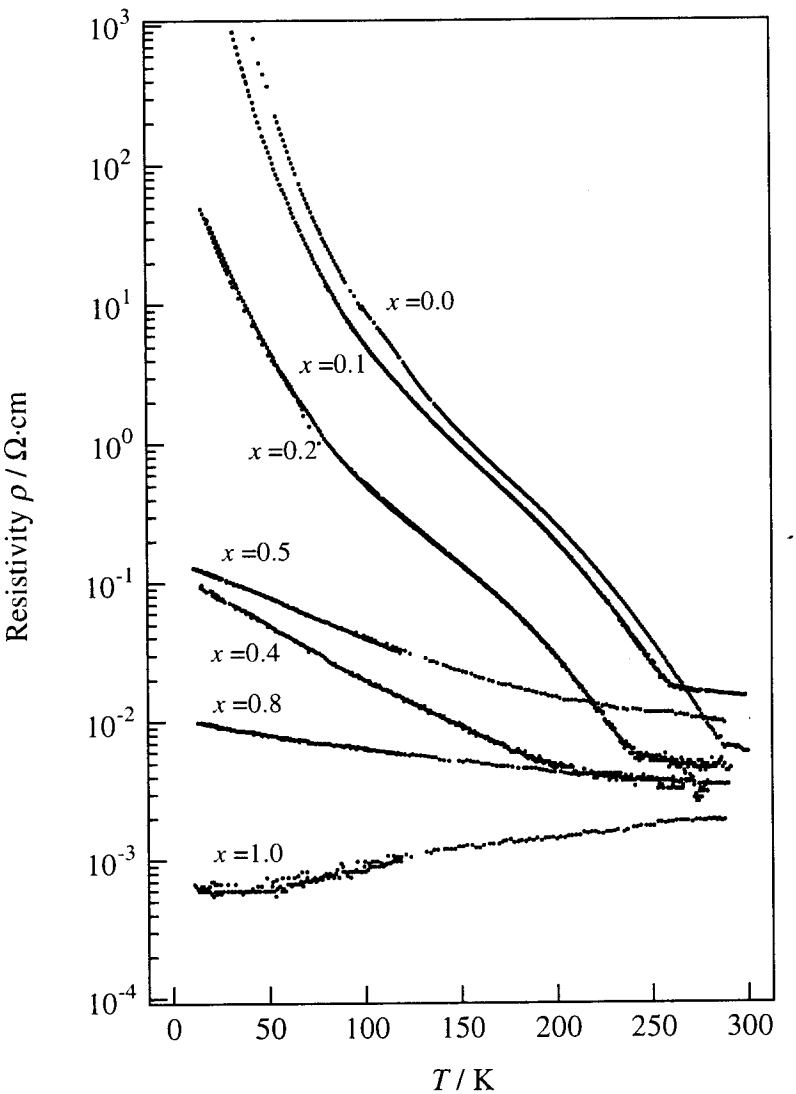

Fig. 3-11 Temperature dependence of the electrical resistivity for $Ca_{1-x}Sr_xFeO_3$.

angles affects their physical properties. The electrical property changes from metallic to semiconducting are related to the structural variations as follows: (1) the increase in the *M*-O bondlength in the MO_6 octahedra, (2) the increase in the distortion of the MO_6 octahedra, and (3) the increase in the bend of MO_6 octahedra connection (*M*-O-*M* angle). The $RRuO_3$ (*R* = Ca, Sr, La Pr) perovskites [10], the $RNiO_3$ (*R* = La, Pr, Nd, Sm) perovskite [11], $RTiO_3$ perovskites (*R* = La, Ce, Nd, Sm, Gd, Y) [12] are the examples

of the geometric effects. The results obtained in the $Ca_{1-x}Sr_xFeO_3$ are consistent with the structure-property relationship described above.

3-6 Magnetic property

Magnetic susceptibility (M) was measured as a function of temperature at fixed fields of 1 kOe. Figure 3-12 shows the temperature dependence of magnetic susceptibility of $Ca_{1-x}Sr_xFeO_3$. All the compositions synthesized in this study exhibited

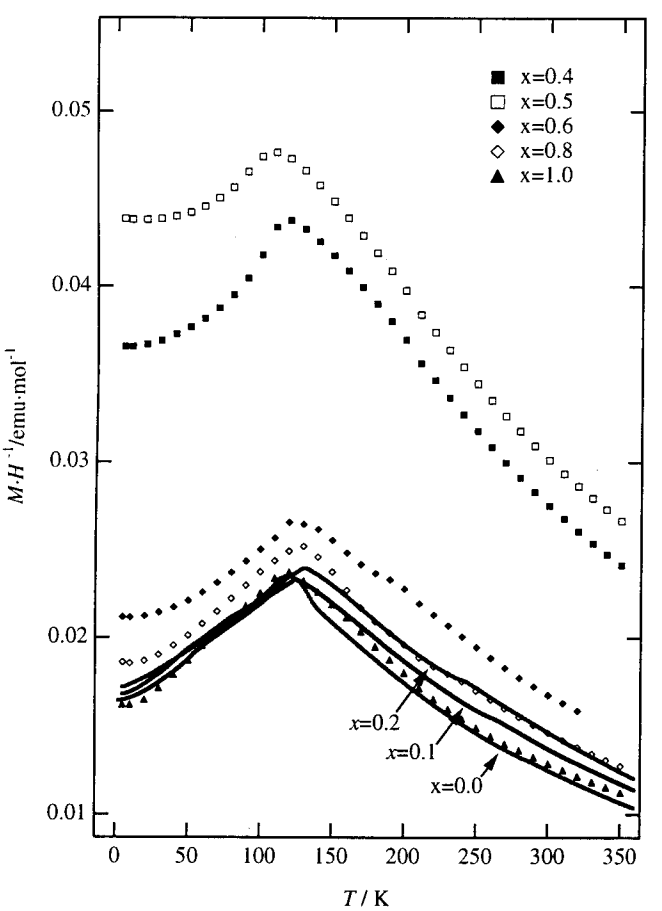

Fig. 3-12 Temperature dependence of the magnetic susceptibility for $Ca_{1-x}Sr_xFeO_3$.

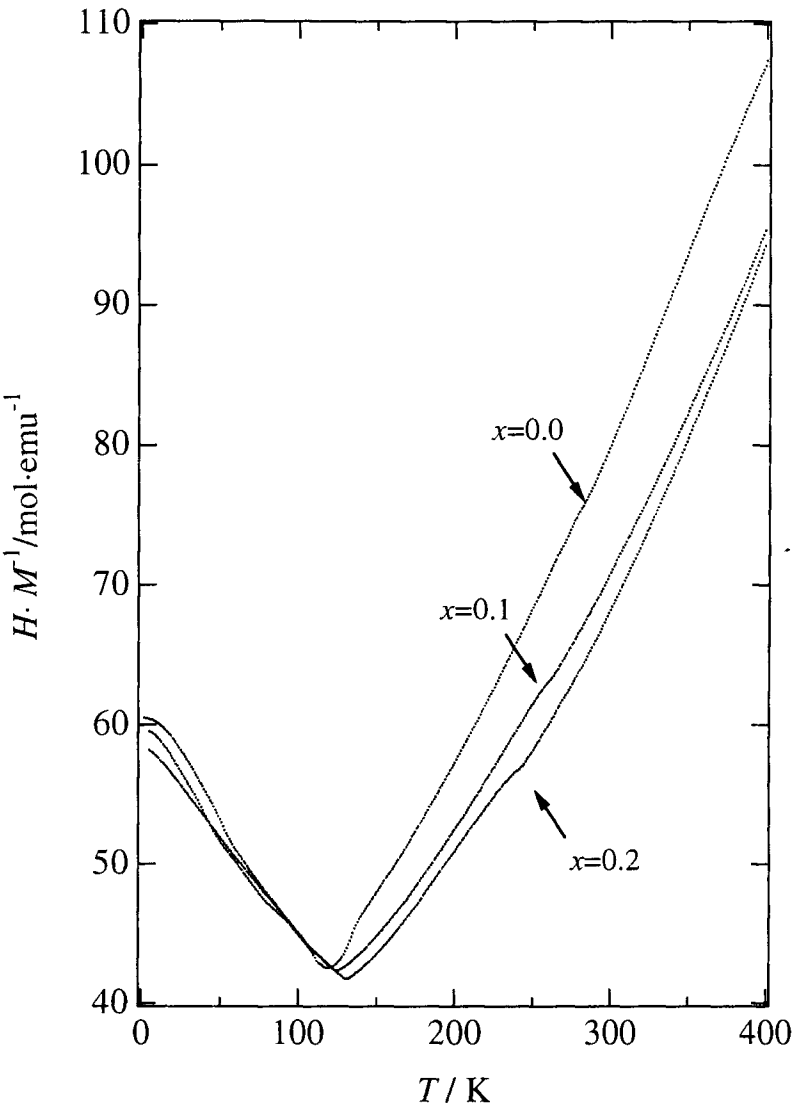

Fig. 3-13 Temperature dependence of the inverse magnetic susceptibility for $Ca_{1-x}Sr_xFeO_3$.

antiferromagnetic transition with transition temperature, T_N = 110 - 130 K. Figure 3-13 shows the temperature dependence of the inverse susceptibility for the samples with x = 0.0 - 0.2. The value of effective magnetic moment (5.39 - 5.52 μ_B) was larger than the expected spin - only moment of 4.9 μ_B. $SrFeO_3$ is an antiferromagnet with a screw spin structure of ferromagnetic nearest-neighbor interaction and antiferromagnetic second - and fourth - neighbor interaction [6]. From similar magnetic behavior in the $Ca_{1-x}Sr_xFeO_3$ solid solution to $SrFeO_3$, the magnetic structure in $Ca_{1-x}Sr_xFeO_3$ is assumed

to be analogous to that for $SrFeO_3$. The positive Weiss constant with antiferromagnetic behavior indicates that the nearest ferromagnetic exchange interaction is strong above the T_N, while below the T_N they order antiferromagnetically.

The changes in slope were observed at the temperatures 290 K, 260 K, and 240 K for the samples with x = 0.0, 0.1, and 0.2, respectively. These temperatures correspond to the electrical resistively changes and changes in isomer shift in Mössbauer study. The difference in isomer shift at 4 K becomes smaller with Sr substitution, which means the CD is expressed in the following way, $2Fe^{4+} \rightarrow Fe^{(3+\delta)+} + Fe^{(5-\delta)+}$, and δ increased to unity with Sr substitution. However, the degree of slope change for $Ca_{0.8}Sr_{0.2}FeO_3$ in magnetic susceptibility is larger than that for $CaFeO_3$. This suggests that the magnetic interactions depend on the Fe-O-Fe angles.

3.7 Conclusion

$Ca_{1-x}Sr_xFeO_3$ with no oxygen vacancy was synthesized at high oxygen pressure using $Ca_{1-x}Sr_xFeO_{2.5+\delta}$. The bend of the FeO_6 octahedra connection changed from 160° to 180° with Sr substitution. This change corresponded to the CD behavior, electrical and magnetic behavior. For the composition $x \leq 0.4$, the electrical and magnetic properties showed slope changes, and these changes corresponded to the beginning of CD measured by Mössbauer study.

Reference

[1] F. Kanamaru, H. Miyamoto, Y. Miura. M. Koizumi, M. Shimada, and S. Kume, *Mat. Res. Bull.*, **5**, 257 (1970).

[2] Y. Takeda, S. Naka, M. Takano, T. Shinjo, T.Takeda, and M. Sjimada, *Mater. Res. Bull.*, **13**, 61 (1978).

[3] Y. Takeda, S. Naka, and M. Takano, *J. Phys. Colloq.*, **40**, C2-331 (1979)

[4] J. B. MacChesney, R. C. Sherwood, and J. F. Poter, *J. Chem. Phys.*, **43**, 1907 (1965).

[5] P. K. Gallagher, J. B. MacChesney, and D. N. E. Buchanan, *J. Chem. Phys.*, **41**, 2429 (1964).

[6] T. Takeda, Y. Yamaguchi, and Y. Watanabe, *J. Phys Soc. Jpn.*, **33**, 967 (1972).

[7] S. Morimoto, T. Yamanaka, and M. Tanaka, *Physica B*, **66-67**, 237 (1997).

[8] R. D. Shannon and C. T. Prewitt, *Acta Crystallogr.*, **B25**, 925 (1969).

[9] M. Takano and Y Takeda, Bull. Inst. Chem. Res., Kyoto Univ., 61, 406 (1983).

[10] H. Kobayahi, M. Nagata, R. Kanno, and Y. Kawamoto, *Mat. Res. Bull.*, **29**, 1271 (1994).

[11] J. B. Torrance, P. Lacorre, A. I. Nazzal, E. J. Ansaldo, and Ch. Niedermayer, *Phys. Rev.*, **B45**, 8209 (1992).

[12] J. E. Greedan, *J. Less-Commom Met.*, **111**, 335 (1985).

Chapter 4

Structural changes of $CaFeO_3$ at low temperatures

4-1 Introduction

Charge disproprotionatoin (CD) have been observed for other iron perovskite oxides ($Sr_{1-x}La_xFeO_3$ [1] and $Ba_{1-x}La_xFeO_3$ [2]) and the related oxide ($Sr_3Fe_2O_7$ [3]). Battle *et al.* performed low temperature neutron diffraction studies on $Sr_2LaFe_3O_{8.94}$ [4] and $BaLaFe_2O_{5.91}$ [5]. Although no changes in crystal structure corresponding to CD were observed, they assigned the magnetic peaks as being due to ordered layers of Fe^{3+} and Fe^{5+} arranged in the ratio of 2:1 for $Sr_2LaFe_3O_{8.94}$, and showed the random arrangement of Fe^{3+} and Fe^{5+} in the ratio of 3:1 for $BaLaFe_2O_{5.91}$. They explained the disordered arrangement of Sr and La may quench a periodic structural variation. Dann *et al.* also performed low temperature neutron diffraction on $Sr_3Fe_2O_7$, which has no cation disorder [3]. However no changes in crystal structure corresponding to CD were observed. They explained the time scale of CD is too slow to be observed by neutron diffraction.

$Sr_{0.7}La_{0.3}FeO_3$ shows CD and magnetic transition at the same temperature at 200 K. Therefore, it is very difficult to extract only the crystal structural changes from neutron diffraction data if it is so small. Recently, transmission electron microscopy for $Sr_{0.7}La_{0.3}FeO_3$ single crystal grown by the floating zone method revealed the same structural modulation [6] that was observed for neutron diffraction magnetically. This shows the structural changes take place at CD transition not only magnetically but also crystallographically.

Recently, Morimoto *et al.* reported the structural changes observed by difference Fourier map using synchrotron X-ray data for $CaFeO_3$ [7]. However no structural data was reported. For $CaFeO_3$, the transition temperature in CD and magnetic transition temperature is 290 K and 117 K, respectively. Therefore, the crystal structural change might be observed by measuring in the temperature between 290 K and 117 K. If the Fe^{3+} and Fe^{5+} exist in the low temperature phase, an expansion and contraction of the FeO_6 octahedra might be expected.

In the present study, low temperature neutron diffraction measurements for

$CaFeO_3$ and $Ca_{0.8}Sr_{0.2}FeO_3$ were performed to study the structural changes corresponding to CD.

4-2 Neutron diffraction

To clarify the relationship between CD and structural changes, the structures at low temperatures were refined using neutron powder diffraction data for the samples $CaFeO_3$ and $Ca_{0.8}Sr_{0.2}FeO_3$ on a time-of-flight (TOF) neutron powder diffractometer, VEGA, at KEK. Intensity data for interplaner spacings between 0.5 and 4.97 Å were used for Rietveld analysis, but those in regions 1.375 – 1.384, 1.397 – 1.408, 1.511 – 1.516, 2.132 – 2.152 Å were excluded in the refinement owing to the appearance of very weak peaks due to the sample holder. The diffraction patterns showed no apparent changes in the temperature range, 130 - 340 K. In the initial refinement, structural parameters were refined with the space group *Pnma* using the structural model used in X-ray diffraction study. Figure 4-1 illustrates the profile fit and difference pattern at 305 K. The solid line is calculated intensities, dots overlying them are observed intensities, and Δy_i is the differences between observed and calculated intensities. The calculated pattern fits the observed one very well. The site occupation parameters g for all atoms refined at 305 K were found to be stoichiometric (g(Ca) = 0.998(4), g(Fe) = 1.0001(18), g(O(1)) = 1.004(4), g(O(2)) = 0.998(7), respectively). Table 4-1 lists final R factors, structural parameters and their estimated deviations.

Temperature dependence of the lattice parameter and unit cell volume are shown in figure 4-2. Around 290 K, a change in slope was observed, which corresponds to the beginning of the CD. It is possible that the symmetry lowered in the CD transition because of the separation of iron. Space group *Pnma* has the seven non-isomorphic subgroups; $P2_12_12_1$, $P112_1/a$, $P12_1/m1$, $P2_1/n11$, $Pnm2_1$, $Pn2_1a$, and $P2_1ma$. These space groups were used for the low temperature phase in the next refinement. At 130 K, the splitting of CD is saturated, and magnetic transition is not observed. Therefore the data at 130 K is appropriate for determining the structural

Table 4-1 Structural parameters for $CaFeO_3$ in *Pnma* at 305K

(a=5.35115(6)Å, b=7.53902(7) Å ,c=5.32546(5) Å

R_{wp}=4.72%, R_p=3.55%, R_R=7.37%, R_e=5.84%, R_I=1.79%, R_F=0.99%, S=R_{wp}/R_e=0.809)

Atom	Site	g	x	y	z	B_{eq} / Å^2
Ca	4*c*	1.0	0.0336(3)	1/4	-0.0046(9)	0.815
Fe	4*b*	1.0	1/2	0.0	0.0	0.245
O(1)	8*d*	1.0	0.2867(2)	0.0337(2)	0.7134(2)	0.507
O(2)	4*c*	1.0	0.4893(4)	1/4	0.0656(4)	0.659
Atom	U_{11} / Å^2	U_{22} / Å^2	U_{33} / Å^2	U_{12} / Å^2	U_{13} / Å^2	U_{23} / Å^2
Ca	0.0114(9)	0.0076(13)	0.119(12)	0	-0.0027(12)	0
Fe	0.0036(3)	0.0021(6)	0.0036(6)	0.0001(4)	-0.0004(5)	0.0029(9)
O(1)	0.0063(4)	0.0065(6)	0.0064(5)	0.0009(5)	0.0005(4)	0.0005(5)
O(2)	0.0093(9)	0.0077(11)	0.0080(11)	0	0.0004(8)	0

Note. Numbers in parentheses are estimated standard deviations of the last significant digit.

The form of the anisotropic temperature factor is

$$\exp\left[-2\pi^2\left(h^2a^{*2}U_{11}+k^2b^{*2}U_{22}+l^2c^{*2}U_{33}+2hka^*b^*U_{12}+2hla^*c^*U_{13}+2klb^*c^*U_{23}\right)\right].$$

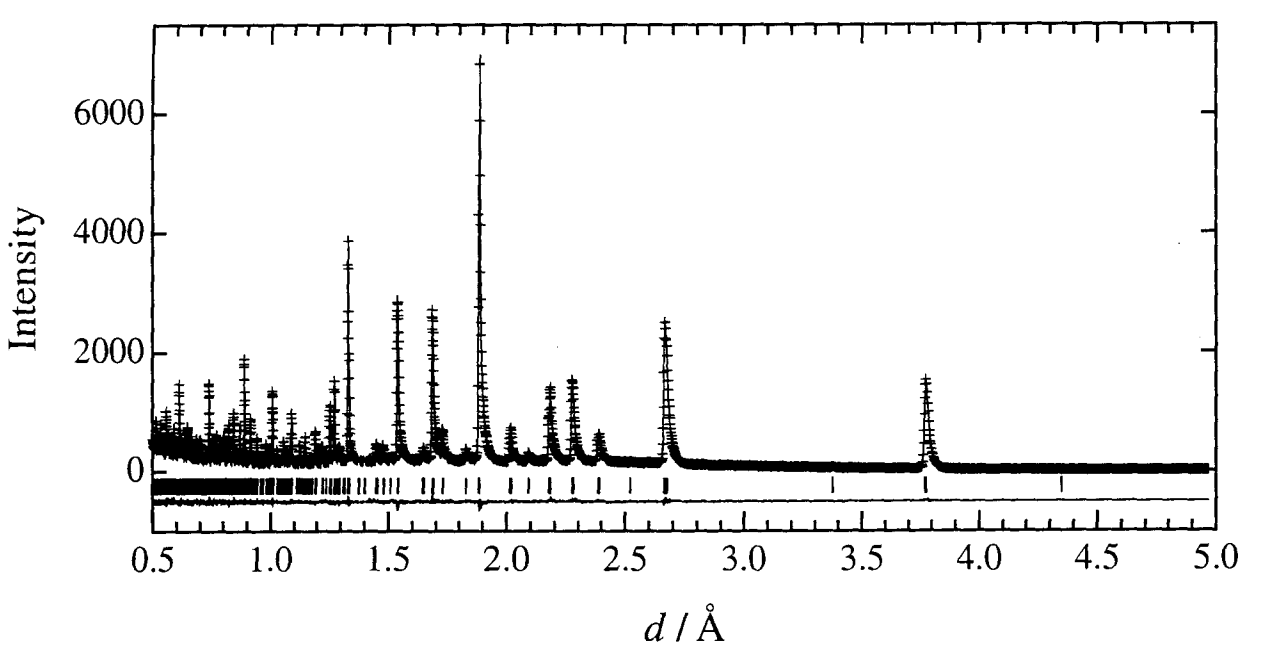

Fig. 4-1 Observed, caluculated, and difference plots for $CaFeO_3$ at 305K.

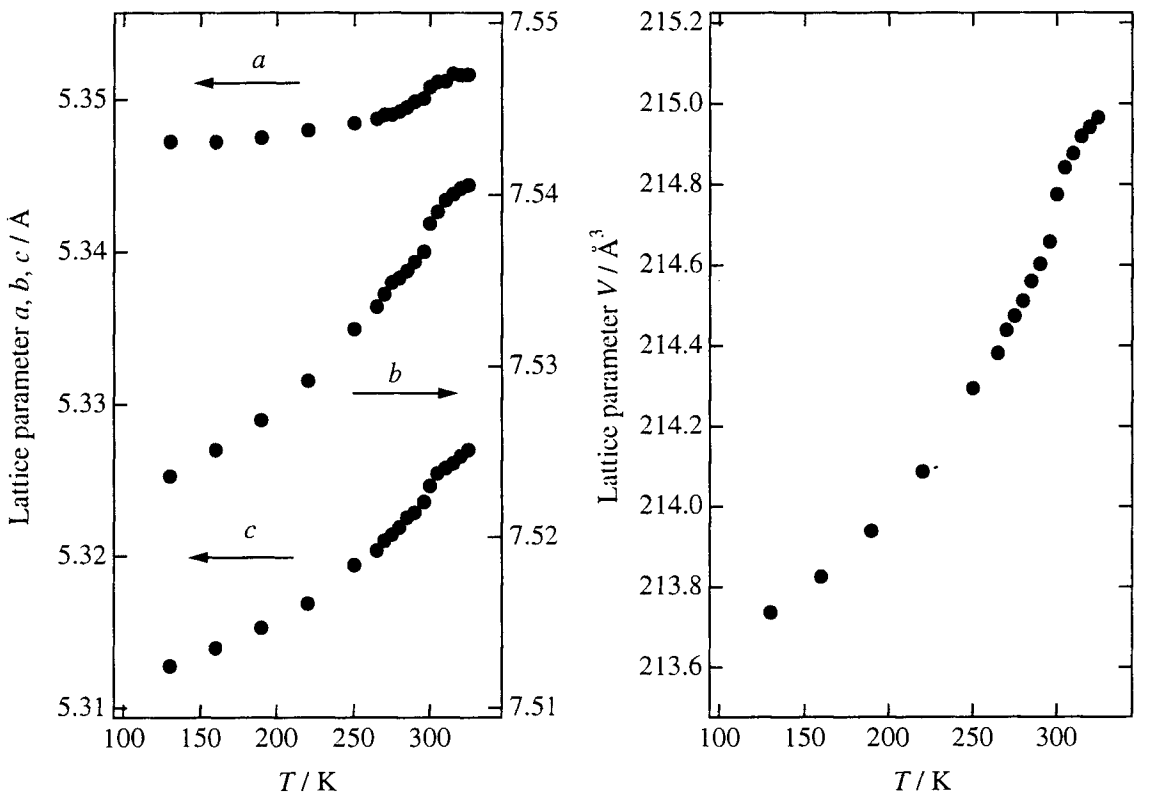

Fig. 4-2 Temperature dependence of the lattice parameter and volume for $CaFeO_3$.

change accompanied by CD. The final R_{wp} factors refined using subgroups model at 130 K are 5.27 ($P2_12_12_1$), 5.28 ($P112_1/a$), 5.22 ($P12_1/m1$), 5.12 ($P2_1/n11$), 5.26 ($Pnm2_1$), 5.24 ($Pn2_1a$), and 5.25 ($P2_1ma$), respectively. The lowest R_{wp} factor was obtained with the $P2_1/n$ monoclinic space group. Below 290 K, the structures were refined with the $P2_1/n$ monoclinic space group, which was reported by Morimoto *et al.* previously [7]. Table 4-2 lists final R factors and Figure 4-3 illustrates the profile fit and difference pattern. Table 4-3 gives interatomic distances from 290 K to 130 K. Figure 4-4 illustrates the structure of $CaFeO_3$ with the space group $P2_1/n$. In this structure, two iron sites exist, Fe(1) and Fe(2), and $Fe(1)O_6$ octahedra are surrounded by six $Fe(2)O_6$

Table 4-2 Structural parameters for $CaFeO_3$ in $P2_1/n$ at 130 K

(a=5.31301(5)Å, b=5.34719(5) Å, c=7.52351(6) Å, β=90.063(2)

R_{wp}=5.12%, R_p=3.86%, R_R=7.39%, R_e=5.58%, R_I=1.70%, R_F=0.94%, $S=R_{wp}/R_e$=0.917)

Atom	Site	g	x	y	z	B_{eq} / Å^2
Ca	4*e*	1.0	-0.0066(6)	0.0369(3)	0.2489(17)	0.59(2)
Fe(1)	2*d*	1.0	1/2	0.0	0.0	0.14(8)
Fe(2)	2*c*	1.0	0.0	1/2	0.0	0.25(8)
O(1)	4*e*	1.0	0.7155(9)	0.2899(12)	0.0355(8)	0.32(8)
O(2)	4*e*	1.0	0.7102(9)	0.2851(13)	0.4663(8)	0.51(9)
O(3)	4*e*	1.0	0.0669(4)	0.4889(3)	0.2476(9)	0.43(2)

Note. Numbers in parentheses are estimated standard deviations of the last significant digit.

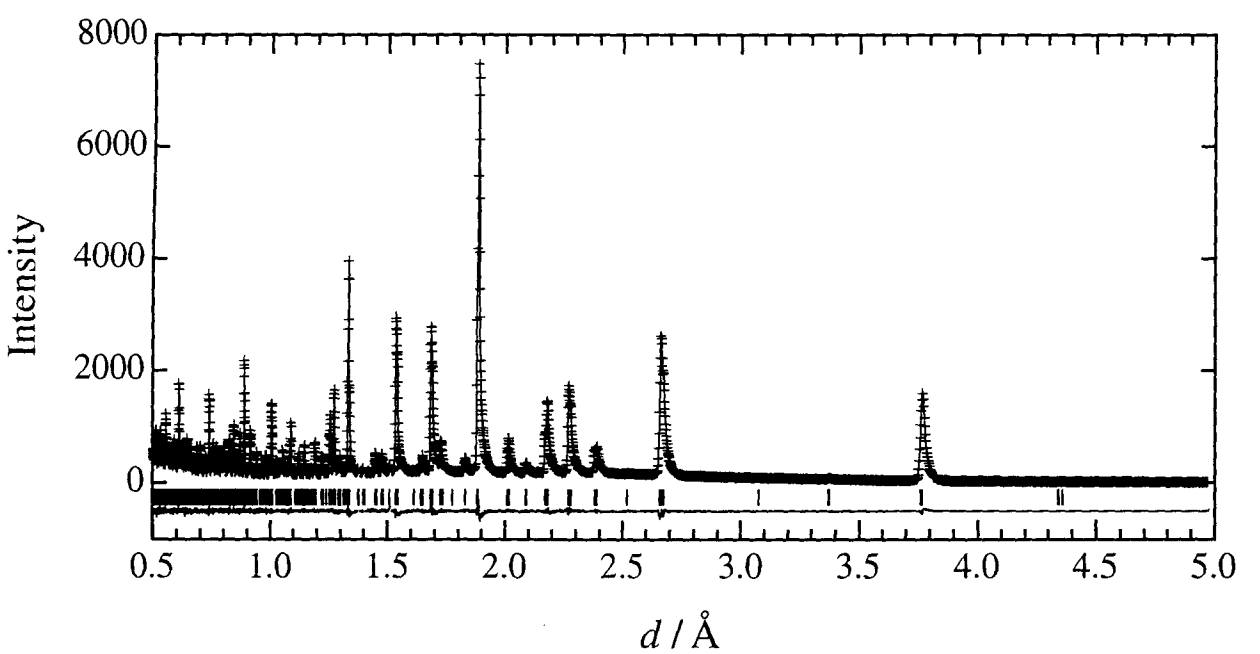

Fig. 4-3 Observed, calculated, and difference plots for $CaFeO_3$ at 130 K.

Table 4-3 Interatomic distances (Å) for $CaFeO_3$ at low temperature

Temperature	Fe(1)-O(1)	Fe(1)-O(2)	Fe(1)-O(3)	Average Fe(1)-O
290	1.92(3)	1.92(3)	1.93(4)	1.92(4)
285	1.93(3)	1.94(2)	1.91(3)	1.93(3)
280	1.933(17)	1.928(18)	1.94(2)	1.933(19)
275	1.93(4)	1.92(4)	1.92(4)	1.92(4)
270	1.93(3)	1.93(3)	1.93(3)	1.93(3)
265	1.94(2)	1.92(2)	1.947(19)	1.94(2)
250	1.942(10)	1.934(9)	1.935(13)	1.937(11)
220	1.947(16)	1.947(15)	1.93(3)	1.940(19)
190	1.93(2)	1.92(2)	1.941(19)	1.93(2)
160	1.948(13)	1.946(12)	1.92(2)	1.937(15)
150	1.950(6)	1.944(6)	1.931(9)	1.942(7)
130	1.948(8)	1.940(8)	1.933(12)	1.941(9)
Temperature	Fe(2)-O(1)	Fe(2)-O(2)	Fe2-O(3)	Average Fe(2)-O
290	1.93(3)	1.92(3)	1.91(4)	1.92(4)
285	1.91(2)	1.92(3)	1.92(3)	1.92(3)
280	1.918(18)	1.917(18)	1.90(2)	1.92(3)
275	1.92(4)	1.93(4)	1.91(4)	1.92(4)
270	1.92(3)	1.92(3)	1.91(4)	1.92(4)
265	1.91(2)	1.93(2)	1.89(2)	1.91(2)
250	1.907(9)	1.912(10)	1.898(13)	1.906(11)
220	1.900(15)	1.901(17)	1.90(3)	1.901(19)
190	1.92(2)	1.92(2)	1.888(19)	1.91(2)
160	1.897(12)	1.902(13)	1.913(12)	1.904(13)
150	1.898(6)	1.902(7)	1.899(9)	1.900(7)
130	1.900(7)	1.904(8)	1.897(11)	1.900(9)

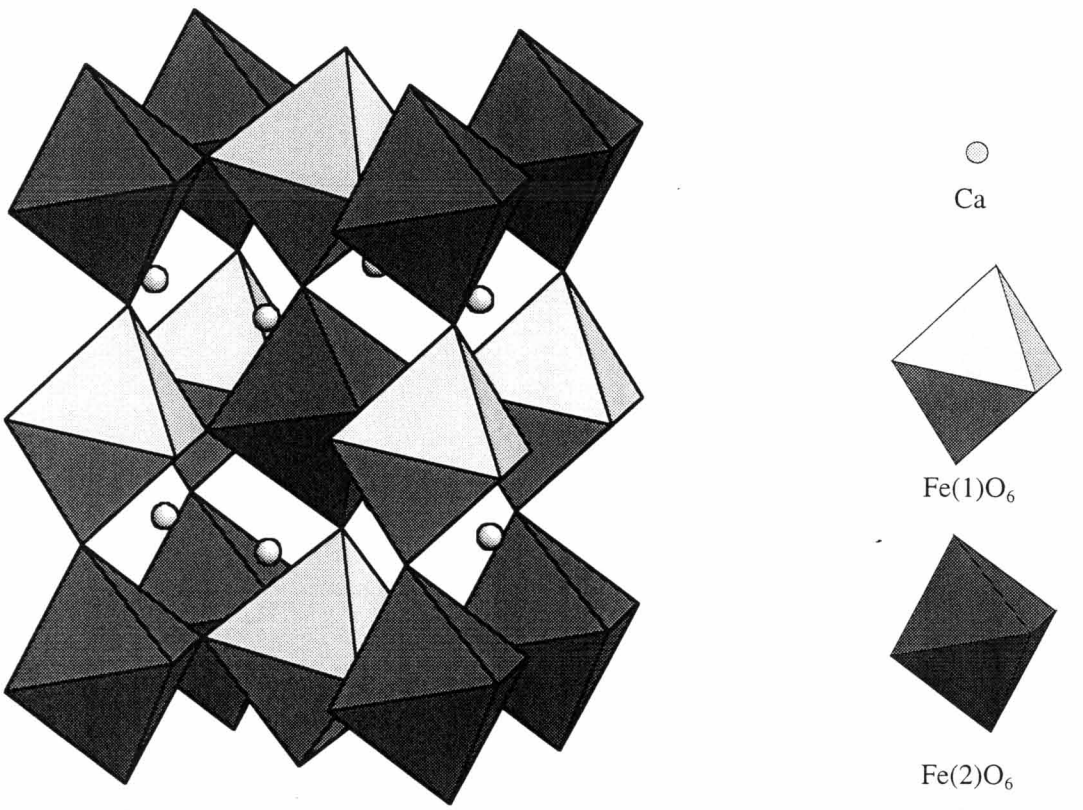

Fig. 4-4 Structure of $CaFeO_3$ ($P2_1/n$).

octahedra and vice versa. Figure 4-5 shows the temperature dependence of the average Fe-O bonds in the $Fe(1)O_6$ and $Fe(2)O_6$ octahedra. The average Fe-O bonds split into two, longer Fe(1)-O(average) and shorter Fe(2)-O(average) at the CD transition temperature, which corresponds to the lower and higher oxidation states of iron, respectively. Figure 4-6 shows the variation in the valence bond sums calculated using the program EUTAX [8] for each atom as a function of temperature. The valence sum of iron at 305 K is 3.856, and two values of iron atom at 130 K is 3.673 and 4.095, respectively. These results indicate the difference of charge is smaller than the values expected from the ionic model. Figure 4-7 shows the monoclinic beta angle. It deviates from 90° suddenly around 290 K and changes slightly with decreasing

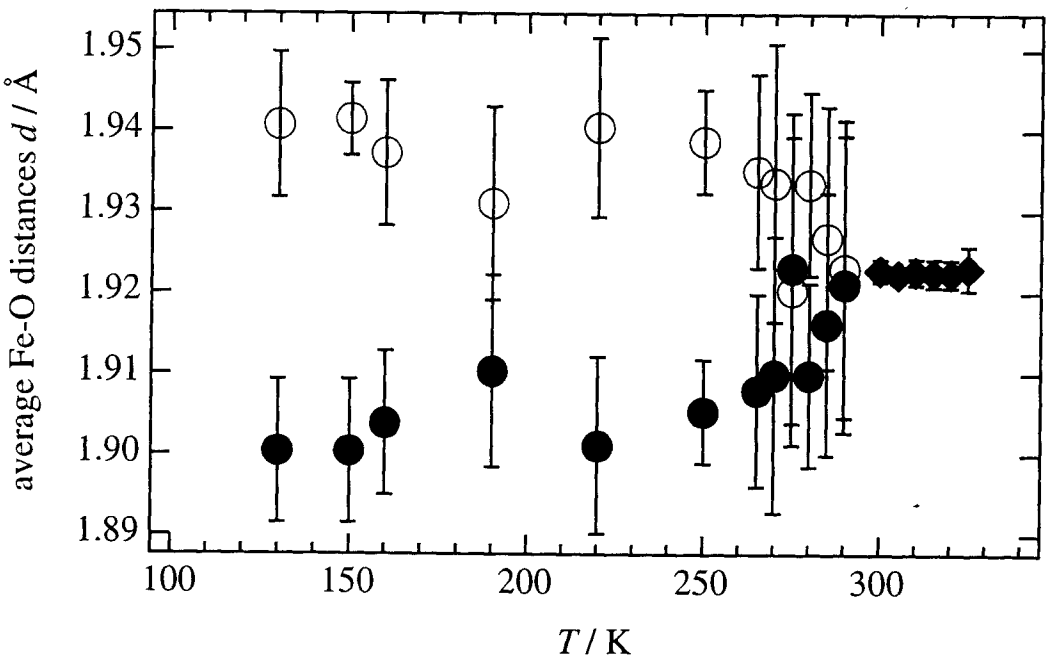

Fig. 4-5 Temperature dependence of the average Fe-O distances.
○:Fe(1)-O, ●:Fe(2)-O

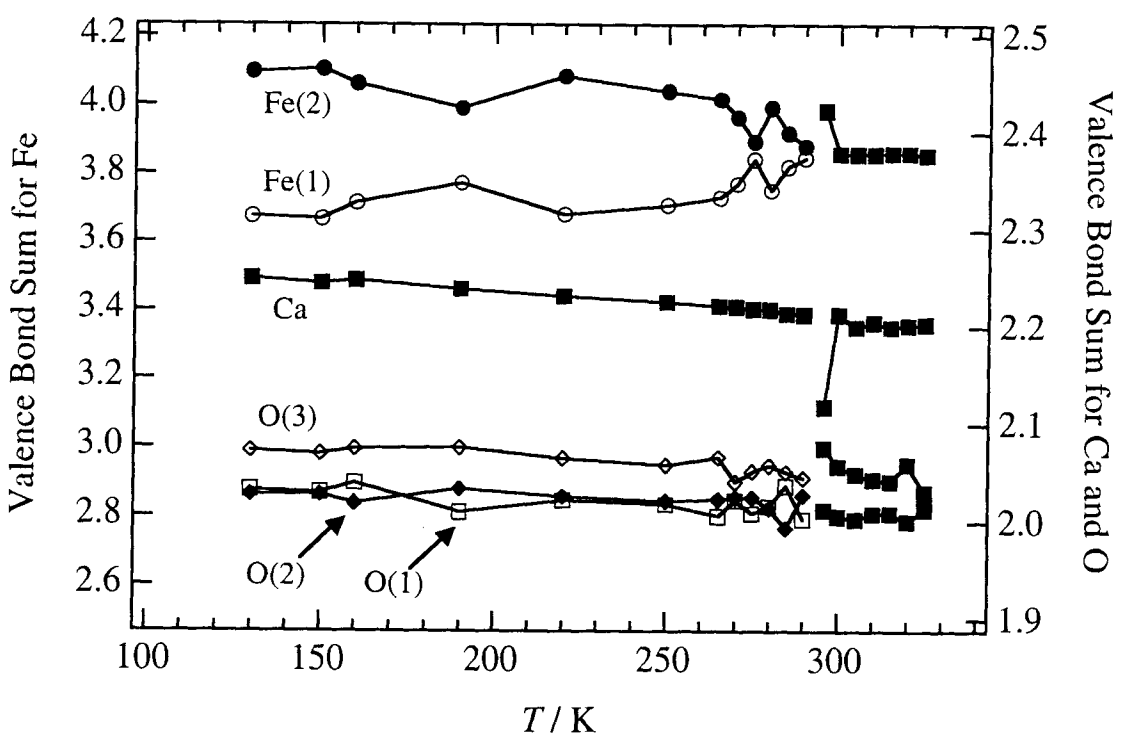

Fig. 4-6 Temperature dependence of the valence bond sums.

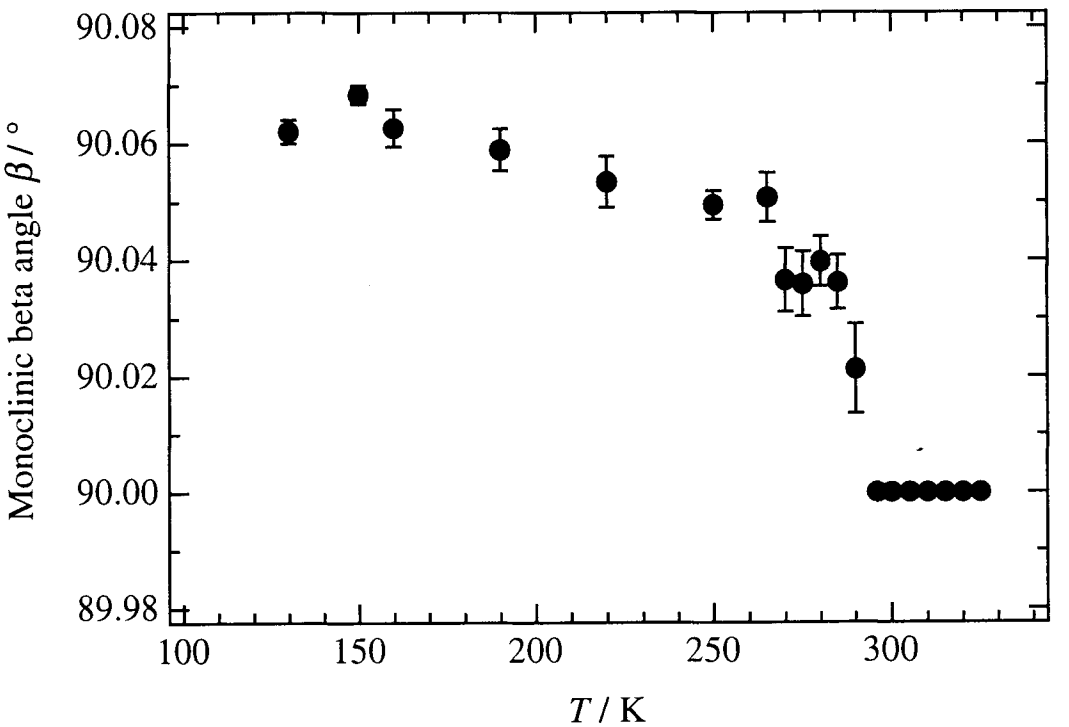

Fig. 4-7 Temperature dependence of the monoclinic beta angle.

temperature. This behavior is similar to that observed by Mössbauer spectroscopy.

For $Ca_{0.8}Sr_{0.2}FeO_3$, low temperature neutron powder diffraction were also performed and refined in the same way. Figure 4-8 shows the temperature dependence of the lattice parameters and unit cell volume. Around 240K, a change in slope was observed in the unit cell volume change, which corresponds to CD, however no apparent changes were observed in the lattice parameter.

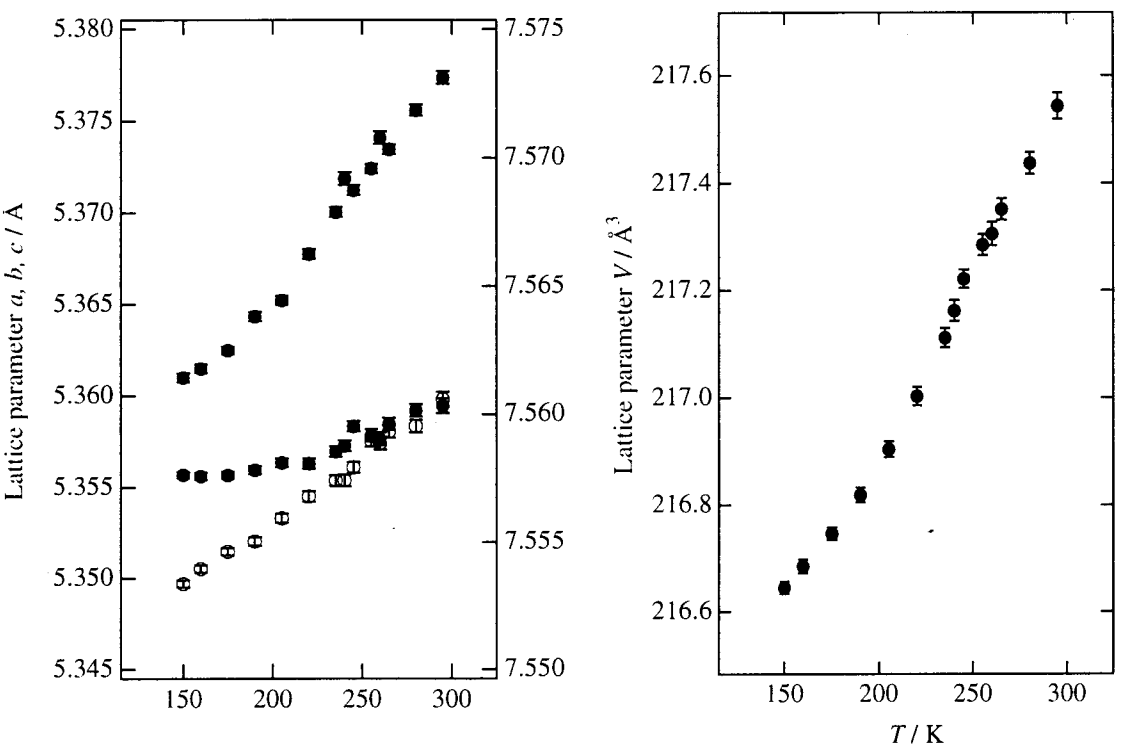

Fig. 4-8 Temperature dependence of the lattice parameters and volume for $Ca_{0.8}Sr_{0.2}FeO_3$.

4-3 Discussion

Photoelectron spectroscopy studies reported by Bocquet *et al.* [9] revealed the Fe^{3+}, Fe^{4+}, and Fe^{5+} ion states to be d^5, $d^5\underline{L}$, and $d^5\underline{L}^2$ accompanying oxygen hole $\underline{L}$, respectively. The distribution of d electron is d^5 and CD is expressed as follows: $2d^5\underline{L} \rightarrow d^5 + d^5\underline{L}^2$. As indicated in the present study, the differences in the two iron – oxygen bond distances was smaller than expected. This suggests that the Fe - O bonding has more covalent than ionic character which is consistent with the above CD mechanism determined by XPS studies.

References

[1] M.Takano, J.Kawachi, N.Nakanishi, and Y.Takeda, *J. Solid State Chem.*, **39**, 75 (1981).

[2] T.C.Gibb, and M. Matsuo, *J. Solid State Chem.*, **81**, 83 (1989).

[3] S.E.Dann, M.T.Weller, D.B.Currie, M.F.Thomas, and A.D.Al-Rawwas, *J. Mater. Chem.*, **3**, 1231 (1993)

[4] P.D.Battle, T.C.Gibb, and P.Lightfoot, *J. Solid State Chem.*, **84**, 271 (1990).

[5] P.D.Battle, T.C.Gibb, P.Lightfoot, and M.Matsuo, *J. Solid State Chem.*, **85**, 38 (1990).

[6] J.Q.Li, Y.Matsui, S.K.Park, and Y.Tokura, *Phys. Rev. Lett.*, **79(2)**, 297 (1997)

[7] S. Morimoto, T. Yamanaka, and M. Tanaka, *Physica B*, **66-67**, 237 (1997)

[8] M. O'Keeffe, "EUTAX", Version 1.3" EMlab Software, Phoenix, AZ, 1993

[9] A. E. Bocquet, A. Fujimori, T. Mizokawa, T. Saitoh, H. Namatame, S. Suga, N. Kimizuka, Y. Takeda, and M. Takano, *Phys. Rev. B*, **45**, 1561 (1992)

Chapter 5

Synthesis and structure of $Tl_2Ru_2O_{7-\delta}$

5-1 Introduction

Thallium pyrochlores synthesized under high pressure were reported to show metallic-semiconducting transition at 120 K [1]. However, it is difficult to get reproducible results on the metallic-semiconducting transition, and the relationships between the structure, the composition, and physical properties are still ambiguous. Due to the high vapor pressure of thallium oxide, it is very difficult to control the stoichiometry. Previously, thallium pyrochlores were synthesized under ambient pressure [2]. High temperature phase $Tl_2Ru_2O_{6.71}$ (synthesized at 1173 K) showed metallic behavior and low temperature phase $Tl_2Ru_2O_7$ (synthesized at 773 K) showed semiconducting behavior. However, no metallic–semiconducting transition was observed. The low temperature phase with nearly stoichiometric composition might be different from those reported by Jarrett *at al.* [1]. Synthesis above 1173 K at atmospheric pressure is difficult because of a complete decomposition from $Tl_2Ru_2O_{7-\delta}$ to RuO_2 and Tl_2O. Therefore high pressure techniques are necessary to control the reaction.

In the present study, $Tl_2Ru_2O_{7-\delta}$ were synthesized under high oxygen pressure and high pressure, and structure, composition, and physical properties were studied by neutron diffraction. Pyrochlore oxides are often known to be nonstoichiometry and the composition of $Tl_2Ru_2O_{7-\delta}$ has oxygen vacancies. From the crystallographic aspect, the pyrochlore structure with $Fd\bar{3}m$ symmetry has only one positional parameter x for oxygen. Neutron diffraction is very powerful probe to determine both the x parameter and the amount of vacancies. In this study, TOF neutron diffraction was performed to determine the structures.

5-2 Synthesis and physical properties

The thallium pyrochlores were synthesized under high pressure and high oxygen pressure. Figure 5-1 shows the temperature dependence of the electrical

resistivity and magnetic susceptibility for both samples. The sample synthesized under high oxygen pressure showed metallic-semiconducting transition and magnetization drop at 120 K, and the magnetic susceptibility increased below 20 K. The sample synthesized under high pressure showed metallic-semiconducting transition and spin-glass like behavior at 50 K.

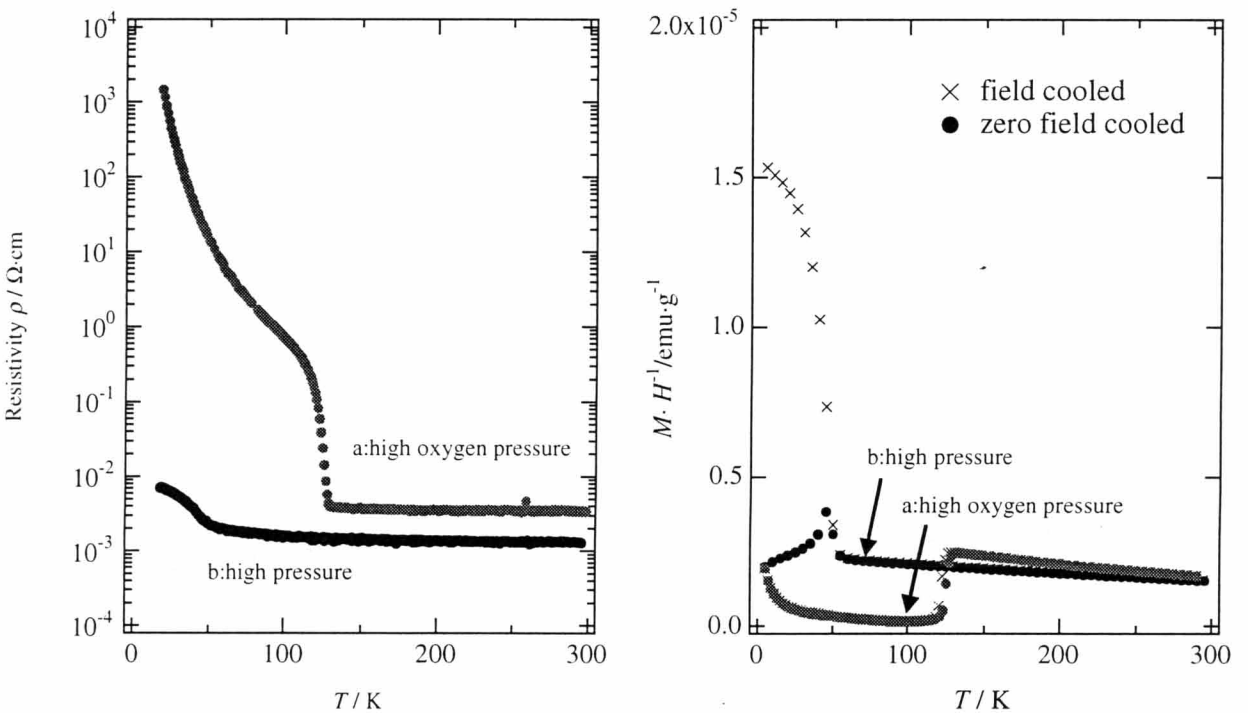

Fig. 5-1 Temperature dependence of the electrical resistivity and magnetic susceptibility for thallium pyrochlores synthesized under high oxygen pressure (a) and high pressure (b).

5-3 Neutron diffraction

Figure 5-2 shows the temperature dependence of the electrical resistivity for the thallium pyrochlores synthesized under high oxygen pressure (a), high pressure (b), ambient pressure (LT phase) (c), and ambient pressure (HT phase) (d). Each sample shows typical behavior of (a) metallic-semiconducting transition at 120 K, (b) metallic-semiconducting transition at 50 K, (c) semiconductig, and (d) metallic, respectively. Previous neutron diffraction studies on the samples synthesized under ambient pressure

[2] indicated that the compositions were $Tl_2Ru_2O_7$ and $Tl_2Ru_2O_{6.71}$ for the LT and HT phase, respectively. The structural studies indicated that these pyrochlores are situated on a borderline between the metallic [3] and semiconducting [4] behavior as described later. It is therefore important to determine the compositions and structures of the samples synthesized under high oxygen pressure and high pressure to clarify the physical property changes.

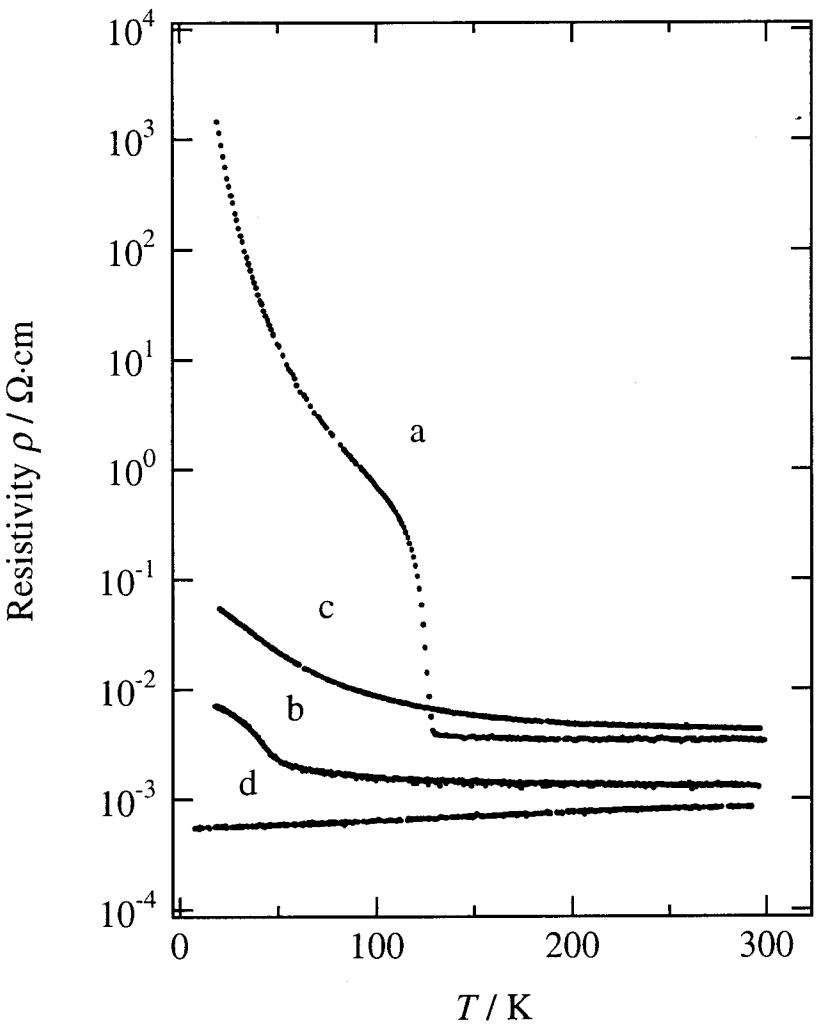

Fig. 5-2 Temperature dependence of the electrical resistivity for the thallium pyrochlores synthesized under high oxygen pressure (a), high pressure (b), ambient pressure (LT phase) (c), and ambient pressure (HT phase) (d).

Neutron diffraction data were taken at room temperature on a time-of-flight (TOF) neutron powder diffractometer, VEGA, at KEK. The structure was refined with the space group $Fd\bar{3}m$ using the initial coordinates, Tl at 16*d* (1/2, 1/2, 1/2), Ru at 16*c* (0, 0, 0), O(1) at 48*f* (*x*, 1/8, 1/8) $x \sim 0.32$, O(2) at 8*b* (8/3, 8/3, 8/3). Table 5-1 lists final *R* factors, lattice, structural parameters, and their estimated standard deviations. The site occupancy for O(2) was refined to be stoichiometric (1.00) and 0.96(3) for the samples synthesized under high oxygen pressure and high pressure, respectively. Table 5-2 gives interatomic distances and bond angles. Figure 5-2 illustrates the profile fit and difference patterns.

Table 5-1(a) Structural parameters for $Tl_2Ru_2O_{7-\delta}$ in $Fd\bar{3}m$

(synthesized under high oxygen pressure, metallic-semiconducting transition at 120 K)

(a=10.1865(2) Å, R_{wp}=9.55%, R_p=6.96%, R_R=13.50%, R_e=7.75%, R_I=3.08%, R_F=3.66%, $S=R_{wp}/R_e$=1.23)

Atom	Site	g	x	y	z	B_{eq} / Å^2
Tl	16*d*	1.0	1/2	1/2	1/2	1.46
Ru	16*c*	1.0	0.0	0.0	0.0	1.28
O(1)	48*f*	1.0	0.3256(4)	1/8	1/8	1.68
O(2)	8*b*	1.0	3/8	3/8	3/8	1.63
Atom	U_{11} /Å^2	U_{22} / Å^2	U_{33} / Å^2	U_{12} / Å^2	U_{13} / Å^2	U_{23} / Å^2
Tl	0.0184(16)	$= U_{11}$	$= U_{11}$	-0.0012(17)	$= U_{12}$	$= U_{12}$
Ru	0.0162(15)	$= U_{11}$	$= U_{11}$	0.000(2)	$= U_{12}$	$= U_{12}$
O(1)	0.024(2)	0.0199(16)	$= U_{22}$	0	0	0.04(2)
O(2)	0.021(3)	$= U_{11}$	$= U_{11}$	0	0	0

RuO_2[a)]

(a=4.4890(2) Å, c=3.1049(4) Å, R_I=8.61%, R_F=5.73%)

Atom	Site	g	x	y	z	B_{eq} / Å^2
Ru	2*a*	1.0	0.0	0.0	0.0	1.4(5)
O	4*f*	1.0	0.309(2)	$= x$	0.0	0.5(3)

[a)] Refinement using space group $P4_2/mmm$

Table 5-1(b) Structural parameters for $Tl_2Ru_2O_{7-\delta}$ in $Fd\bar{3}m$

(synthesized under high pressure, metallic-semiconducting transition at 50 K)

(a=10.1831(2) Å, R_{wp}=6.86%, R_p=5.36%, R_R=20.66%, R_e=6.13%, R_I=3.74%, R_F=3.04%, $S=R_{wp}/R_e$=1.12)

Atom	Site	g	x	y	z	B_{eq} / Å^2
Tl	16*d*	1.0	1/2	1/2	1/2	1.46
Ru	16*c*	1.0	0.0	0.0	0.0	1.34
O(1)	48*f*	1.0	0.3247(4)	1/8	1/8	1.61
O(2)	8*b*	0.96(3)	3/8	3/8	3/8	1.45
Atom	U_{11} / Å^2	U_{22} / Å^2	U_{33} / Å^2	U_{12} / Å^2	U_{13} / Å^2	U_{23} / Å^2
Tl	0.0185(14)	$=U_{11}$	$=U_{11}$	-0.0006(16)	$=U_{12}$	$=U_{12}$
Ru	0.0170(14	$=U_{11}$	$=U_{11}$	0.000(2)	$=U_{12}$	$=U_{12}$
O(1)	0.023(2)	0.0189(16)	$=U_{22}$	0	0	0.04(2)
O(2)	0.018(4)	$=U_{11}$	$=U_{11}$	0	0	0

Note. Numbers in parentheses are estimated standard deviations of the last significant digit.

The form of the anisotropic temperature factor is

$$\exp\left[-2\pi^2\left(h^2a^{*2}U_{11}+k^2b^{*2}U_{22}+l^2c^{*2}U_{33}+2hka^*b^*U_{12}+2hla^*c^*U_{13}+2klb^*c^*U_{23}\right)\right].$$

Table 5-2 Interatomic distances and bond angles for $Tl_2Ru_2O_7$ synthesized under high oxygen pressure and $Tl_2Ru_2O_{6.96}$ synthesized under oxygen pressure

Coordinate triplets: i)x, y+1/2, z+1/2; ii)x-1/4, y+1/4, -z;
iii)-x+1/4, -y+1/4, z; iv)-x+1/4, y, -z+1/4; v)-x, -y+3/4, -z+3/4
vi)x, y-1/2, z-1/2; vii)-x+3/4, y, -z+3/4; viii)-z, x-1/4, y-1/4

Phase	$Tl_2Ru_2O_7$	$Tl_2Ru_2O_{6.96}$
Distances	d / Å	
Tl-O(1^{i}) (×6)	2.530(3)	2.535(3)
Tl-O(2) (×2)	2.2054(1)	2.2047(1)
Ru-O(1^{ii}) (×6)	1.9586(18)	1.9543(17)

Angles	θ / °	
Ru^{iii}-O(1)-Ru^{iv}	133.7(2)	134.2(2)
Tl^{v}-O(1)-Tl^{iv}	90.78(15)	90.48(14)
Tl^{v}-O(2)-Tl^{vii}	109.4712	109.4712
O(1^{ii})-Ru-O(1^{viii})	95.09(17)	94.75(15)

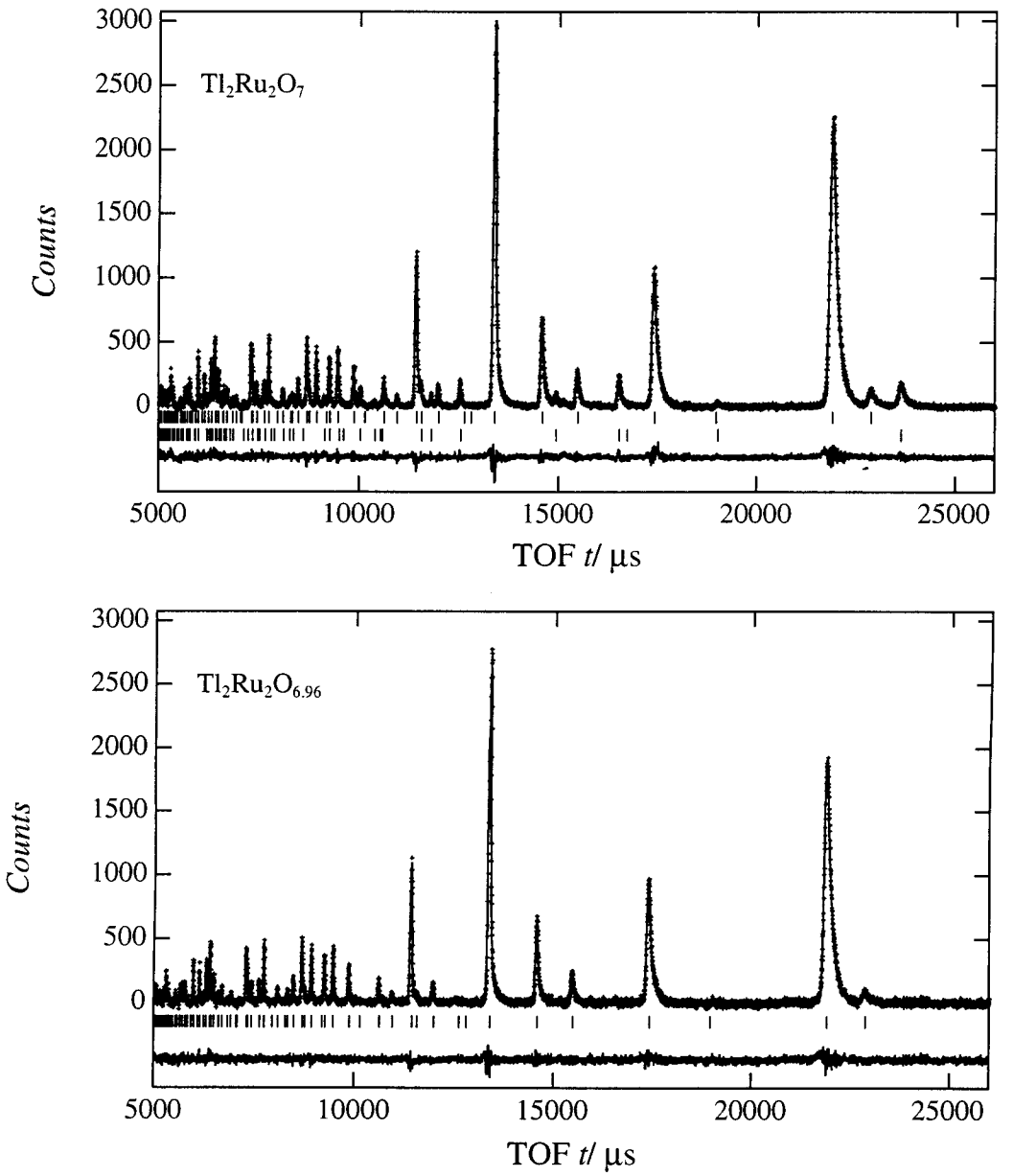

Fig. 5-2 Observed, calculated, and difference plots for $Tl_2Ru_2O_7$ and $Tl_2Ru_2O_{6.96}$. The refinement of $Tl_2Ru_2O_7$ was carried out using two-phase model with RuO_2.

To clarify the relations between the structures and physical properties, the bond distances and angles are summarized for the compositions and synthesis comditions.

(i) $Tl_2Ru_2O_7$ (120MS, high oxygen pressure phase with stoichiometric composition),

(ii) $Tl_2Ru_2O_{6.96}$ (50MS, high pressure phase with small amount of oxygen vacancies),

(iii) $Tl_2Ru_2O_7$ (LT, low-temperature phase at ambient pressure condition),

(iv) $Tl_2Ru_2O_{6.71}$ (HT, high-temperature phase with oxygen vacancies).

Like the cubic-perovskite structure, the pyrochlores $A_2B_2O_6O'$ have a BO_3 array of corner-sharing octahedra, but the *B*-O-*B* angles are reduced from 180° to about 130°. Reduction of the *B*-O-*B* angles from 180° reduces the *B*-O-*B* overlap integrals; the electrical properties of the pyrochlores might thus be affected by a small change in the *B*-O-*B* angles. Figure 5-4 shows the relationship between the bond distances and bond angles of four samples indicated above (i), (ii), (iii), and (iv). With increasing Ru-O(1) distances, O(1)-Ru-O(1) angles split from 90°, the Ru-O(1)-Ru angle decreases, and the Tl-O(1) distance decreases. The increase in the Ru-O(1) bond lengths leads to the distortion of RuO_6 octahedra, and the reduction of Ru-O(1)-Ru angles, which tends to localize electrons due to the reduced Ru-O(1) interaction. The pyrochlore structure is viewed as being made up of two networks, $(Tl_2O)_\infty$ and $(RuO_3)_\infty$, which interpenetrate with each other. The bridging oxide ions, O(1), are connected to both Tl and Ru ions, and the Tl-O(1) bond strength might strongly affect the Ru-O(1) bond. These two interactions are competitive; the stronger the Tl-O(1) bond, the weaker the Ru-O(1) bond. The fact that the Tl-O(1) distance decreases with increasing Ru-O(1) distance corresponds to the change from semiconducting to metallic character, through the metallic-semiconducting transition. The relationship between the electrical properties and the structures has been reported for the $Bi_{2-x}Ln_xRu_2O_7$ and $Pb_{2-x}Ln_xRu_2O_{7-\delta}$ (*Ln* = Pr-Lu, Y) solid solutions [4, 5, 6]. The resistivity increases with x, and the metallic property changes to semiconducting between x = 1.2 and 1.4. With increasing *Ln* content, the Ru-O(1) bond lengths increase, the distortion of the RuO_6 octahedra increases, and the bend in the RuO_6 zigzag chains increases from x = 0 to 2.0. These structural changes are quite similar to those found in the thallium pyrochlores. Figure 5-5 summarizes the Ru-O(1) bond distances and the Ru-O(1)-Ru angles for the Ru-containing pyrochlores. The metallic region is obviously separated from the

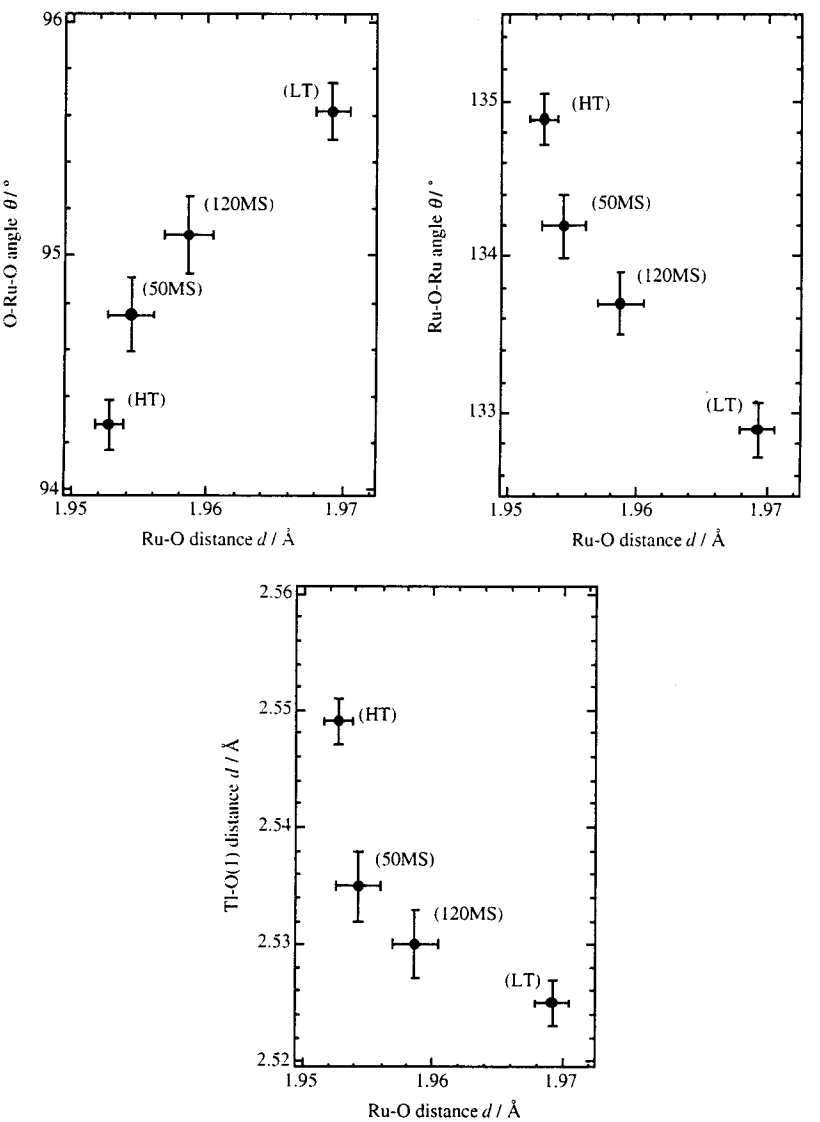

Fig. 5-4 Relations between the Ru-O distances, O(1)-Ru-O(1) angles, Ru-O(1)-Ru angles, and Tl-O(1) distances angles for the thallium pyrochlores.

semiconducting region; the compounds with Ru-O(1) distances of 1.94-1.97 Å and Ru-O(1)-Ru angles of 134-139° show metallic behavior, and those with Ru-O(1) distances of 1.97-2.00 Å and Ru-O(1)-Ru angles of 129-134° show semiconducting behavior. The bond distances and bond angles determined for $Tl_2Ru_2O_{7-\delta}$ correspond to the borderline between metallic and semiconducting behavior. Recently, the importance of the Ru-O-Ru angle was also confirmed by neutron diffraction studies on $Ln_2Ru_2O_7$ [7]. They indicated that the angles greater than 133° are necessary to facilitate metallic conductivity, which is consistent with the present results.

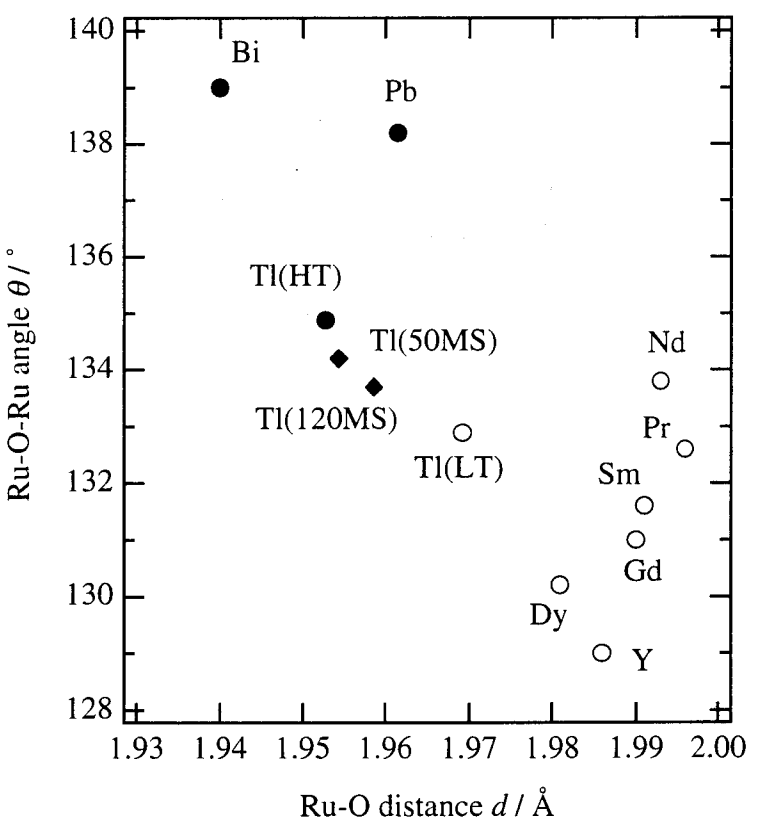

Fig. 5-5 Relations between the Ru-O distances and Ru-O-Ru angles in $A_2Ru_2O_{7-\delta}$. ●:samples showing metallic property, ◆ :samples showing metallic-semiconductting transition, ○:samples showing semiconducting property

Figure 5-6 shows the relations between ionic radii of *A* ions [8] and *A*-O(1), *A*-O(2), and the average of eight *A*-O distances in the ruthenium pyrochlores. The data is taken from previous X-ray Rietveld refinement results [4, 5] and also from the recent results on neutron diffraction experiments [7]. The bond distances obtained from the X-ray and neutron diffraction experiments are consistent with each other with exception of the bismuth pyrochlore. This might be caused by the difference in the sample stoichiometry; the sample used for the structure analysis using neutron diffraction contains O(2) deficiency and the composition was $Bi_2Ru_2O_{6.92}$ [9]. The Pb-O distances are also shorter than the value expected from other lanthanum series, which might be caused by the different valence, $Pb^{2.5+}$, and oxygen deficiency [3]. In the stoichiometric pyrochlores ($A_2Ru_2O_7$ with *A* = Y, Dy, Gd, Sm, Nd, Pr, Bi, and Tl), the *A* –O distances increase with increasing ionic radii of the lanthanum ions from Y to Pr, and the Bi-O distances obtained by the X-ray data are consistent with those expected from the extrapolation from Y to Pr. The dashed line, *A*-O(average), is obtained from the sum of the ionic radii of lanthanum ions and oxygen ions and the line is consistent with the *A*-O(average) plots determined from the X-ray and neutron diffraction experiments. However, the Tl-O distances significantly deviate from the values expected from the relationship. This indicates that the ionic radii used for thallium [8] is too short in the pyrochlore structure and a reasonable value for Tl^{3+}(VIII) is estimated from this figure to be 1.08 - 1.09 Å.

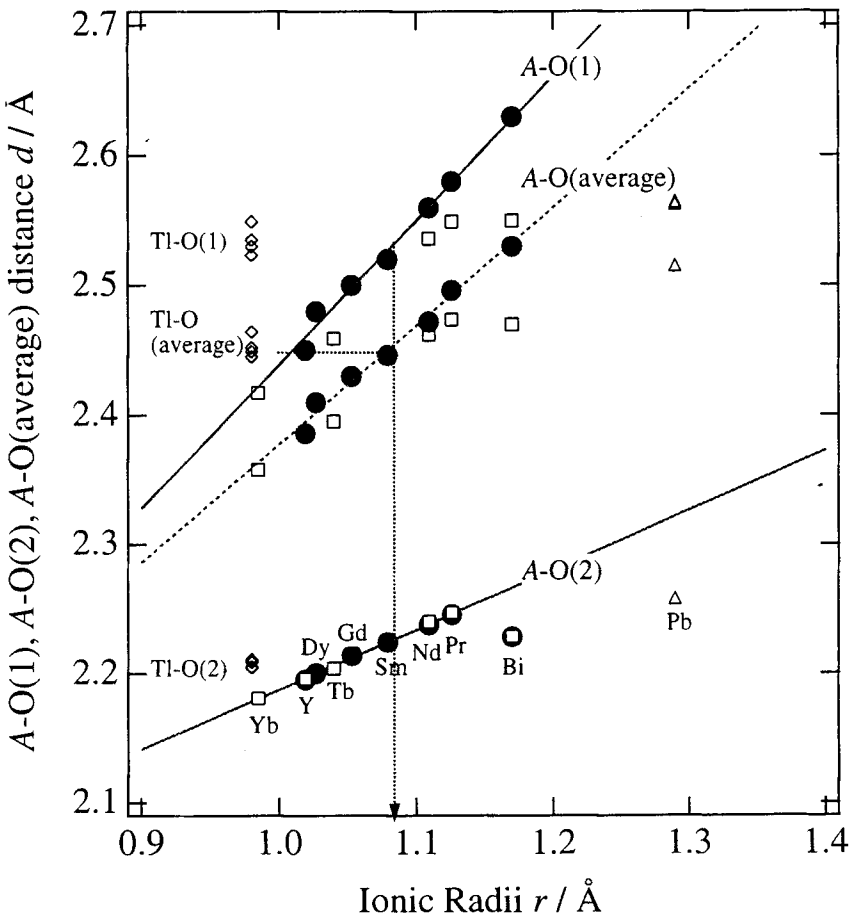

Fig. 5-6 Relations between ionic radii and *A*-O bond distances. Bond distances are taken from X-ray [4, 5] (●), neutron (this study) (◇), neutron [3] (△), and neutron [7] (□) diffraction experiments. Straight lines in the *A*-O(1) and *A*-O(2) distances indicate the least squares fit of the bond distances from $A_2Ru_2O_7$ (*A* = Yb - Pr, Y). The dashed line is calculated from the sum of the ionic radii of A^{3+}(VIII) ions and O^{2-}(IV) ions.

5-4 Conclusion

Systematic synthesis in high pressure condition was carried out to elucidate the relationship between synthesis condition and physical properties. Two categories of electrical properties were found: metallic-semiconducting transition at 120 K (high oxygen pressure synthesis), and metallic-semiconducting transition at 50 K (high pressure synthesis). Magnetic measurements also showed the different behavior depending on the synthesis condition. The sample synthesized under high oxygen pressure showed the magnetization drop at metallic-semiconducting transition temperature 120 K and an increase below 20 K. The sample synthesized under high pressure showed spin-glass like behavior at metallic-semiconducting transition temperature 50 K.

Neutron diffraction study clarified the compositions and structures for both samples. While a small amount of oxygen vacancy ($Tl_2Ru_2O_{6.95}$) was observed for the sample synthesized under high pressure, the stoichiometric composition ($Tl_2Ru_2O_7$) was found for the sample synthesized under high oxygen pressure. The structure determined for $Tl_2Ru_2O_{7-\delta}$ correspond to the borderline between metallic and semiconducting behavior, and a small change in structure has much effect on the physical properties.

References

[1] R. Kanno, J. Huang, and A. W. Sleight, JAERI-M 93-228 Vol. 2 "Proceedings of the Fifth International Symposium on Advanced Nuclear Energy Research, Neutron as Microscopic Probes, March 1993," p. 347.

[2] H. S. Jarrett, A. W. Sleight, J. F. Weiher, J. L. Gillson, C. G. Frederick, G. A. Jones, R. S. Swingle, D. Swartzfager, J. E. Gulley, and P. C. Hoell, "Valence Instabilities and Related Narrow-Band Phenomena" (R. D. Parks, Ed.), p. 545. Plenum, New York, 1977.

[3] R. A. Beyerlein, H. S. Horowitz, J. M. longo, and M. E. Leonowicz, *J. Solid State Chem.*, **51**, 253 (1984)

[4] R. Kanno, Y. Takeda, T. Yamamoto, Y. Kawamoto, and O. Yamamoto, J. *Solid State Chem.* **102**, 106 (1993).

[5] T. Yamamoto, R. Kanno, Y. Takeda, O. Yamamoto, Y. Kawamoto, and M. Takano, *J. Solid State Chem.* **109**, 372 (1994).

[6] H. Kobayashi, R. Kanno, Y. Kawamoto, T. Kamiyama, F. Izumi, and A. W. Sleight, *J. Solid State Chem.* **114**, 15 (1995).

[7] B. J. Kennedy and T. Vogt, J. *Solid State Chem.*, **126**, 261 (1996)

[8] R. D. Schannon and C. T. Prewitt, *Acta Crystallogr*, **B25**, 925 (1969)

[9] G. R. Facer, M. M. Elcombe, and B. J. Kennedy, *Aust.. J. Chem.*, **46**, 1897 (1993)

Chapter 6

Metallic–semiconducting transition at 120 K in thallium pyrochlore

6-1 Introduction

Stoichiometric thallium pyrochlore $Tl_2Ru_2O_7$ shows the metallic–semiconducting transition and magnetization drop at 120 K. However, the mechanism of metallic–semiconducting transition and magnetization drop is not clear. In this study, neutron diffraction measurement was performed to study the structure below the transition temperature.

6-2 Neutron diffraction at low temperatures

Neutron diffraction data were taken at 150, 100, and 2 K on an angle dispersion neutron powder diffractometer, D2B, at the ILL. The diffraction pattern at 150 K indexed as a cubic cell and the parameters were refined with space group $Fd\bar{3}m$. The site occupation parameters, g, of the Tl, and O(2) sites were also refined; no significant deviation from the stoichiometric composition was observed for the Tl (g = 1.000(2)), and O(2) (g = 1.000(6)) sites. In the final refinement cycle, anisotropic thermal parameters were assigned for all the sites. No correction was made for preferred orientation. The refinement results are indicated in Table 6-1. Bond distances and angles are shown in Table 6-2.

The diffraction pattern at 100 K also indicated a cubic cell with a = 10.17 Å, similar to that of 150 K. However, small reflections were observed and are indexed by the same cell as the parent cubic cell. No extinction rules were observed in this cubic cell. Previously, the superlattice reflections was observed by low-temperature X-ray diffraction measurements [1], and the reflections were consistent with those observed in the neutron diffraction measurements. This indicates a first order crystallographic phase transition. The refinements were carried out using several structural models with lower symmetry such as $P4\bar{3}m$ and $P\bar{4}m2$. However, these models did not lead to low R-values. Several structural models have been proposed based on the ordering

Table 6-1 Structural parameters for $Tl_2Ru_2O_{7-\delta}$ in $Fd\bar{3}m$ at 150 K

(synthesized under high oxygen pressure, metallic-semiconducting transition at 120 K)

(a=10.17528(5) Å, R_{wp}=3.08%, R_p=2.33%, R_R=9.33%, R_e=2.25%, R_I=2.04%, R_F=1.40, S=R_{wp}/R_e=1.3728)

Atom	Site	g	x	y	z	B_{eq} / Å^2
Tl	16*d*	1.0	1/2	1/2	1/2	0.48
Ru	16*c*	1.0	0.0	0.0	0.0	0.24
O(1)	48*f*	1.0	0.32684(10)	1/8	1/8	0.48
O(2)	8*b*	1.0	3/8	3/8	3/8	0.50
Atom	U_{11} / Å^2	U_{22} / Å^2	U_{33} / Å^2	U_{12} / Å^2	U_{13} / Å^2	U_{23} / Å^2
Tl	0.0061(3)	= U_{11}	= U_{11}	0.0002(3)	= U_{12}	= U_{12}
Ru	0.0030(3)	= U_{11}	= U_{11}	-0.0006(4)	= U_{12}	= U_{12}
O(1)	0.0095(5)	0.0043(3)	= U_{22}	0	0	0.0011(4)
O(2)	0.0063(8)	= U_{11}	= U_{11}	0	0	0

RuO_2[a)]

(a=4.48814(17) Å, c=3.10589(16) Å, R_I=5.85%, R_F=3.91%)

Atom	Site	g	x	y	z	B_{eq} / Å^2
Ru	2*a*	1.0	0.0	0.0	0.0	0.32(17)
O	4*f*	1.0	0.3054(6)	= x	0.0	0.21(17)

Note. Numbers in parentheses are estimated standard deviations of the last significant digit.

The form of the anisotropic temperature factor is

$$\exp\left[-2\pi^2\left(h^2a^{*2}U_{11}+k^2b^{*2}U_{22}+l^2c^{*2}U_{33}+2hka^*b^*U_{12}+2hla^*c^*U_{13}+2klb^*c^*U_{23}\right)\right].$$

[a)] Refinement using space group $P4_2/mmm$

Table 6-2 Interatomic distances and bond angles for $Tl_2Ru_2O_7$ synthesized under high oxygen pressure at 150 K

Coordinate triplets: i)x, y+1/2, z+1/2; ii)x-1/4, y+1/4, -z; iii)-x+1/4, -y+1/4, z; iv)-x+1/4, y, -z+1/4; v)-x, -y+3/4, -z+3/4 vi)x, y-1/2, z-1/2; vii)-x+3/4, y, -z+3/4; viii)-z, x-1/4, y-1/4	
Phase	$Tl_2Ru_2O_7$
Distances	d / Å
Tl-O(1^{i}) (×6)	2.530(3)
Tl-O(2) (×2)	2.2054(1)
Ru-O(1^{ii}) (×6)	1.9586(18)
Angles	θ / °
Ru^{iii}-O(1)-Ru^{iv}	133.7(2)
Tl^{v}-O(1)-Tl^{iv}	90.78(15)
Tl^{v}-O(2)-Tl^{vii}	109.4712
O(1^{ii})-Ru-O(1^{viii})	95.09(17)

in the metal ions in the pyrochlore structure. For example, one dimensional ordering of the metal ions sites was reported for the fluoride pyrochlores, $NH_4Fe_2F_4$, where the Fe^{3+} and Fe^{2+} ions are ordered one dimensionally along the 010 and 100 directions, respectively, in the orthorhombic cell with space group *Pnma* [2, 3]. This model was then considered for the low-temperature structure. In the space group *Pnma*, both Tl and Ru sites split into two, and these two sites order one dimensionally. The 48*f* O site is divided into four sites. The relationship between the cubic and the new orthorhombic cell is as follows: $a_o \approx b_o \approx a_c/2^{1/2}$. Refinements using this structural model led to a significant reduction in the *R*-values, and all superlattice reflections were explained by this model. In the final refinement, the refinement on the *B* parameters was unstable and the *B* parameters of the oxygen sites had to be constrained to the same

value. The diffraction pattern at 2 K also shows the same superlattice reflections as that of 100 K, and no magnetic reflections were observed. The refinements were carried out with the same structural model.

Figure 6-1 shows the profile fit and difference patterns of $Tl_2Ru_2O_7$ at 150, 100, and 2 K. The refinement results at 100, and 2 K are indicated in Table 6-3. Bond distances and angles are shown in Table 6-4. The temperature dependence of the lattice parameters for the thallium pyrochlores with the results obtained for X-ray diffraction are shown in Figure 6-2. A large increase in the lattice parameters was observed at the transition temperature, 120 K. This is explained by a first order crystallographic phase transition. Figure 6-3 shows the temperature dependence of the atomic distances and angles. The average values of Tl(1)-O, Tl(2)-O, Ru(1)-O, and Ru(2)-O distances are indicated for the low-temperature phase. The Ru-O distances increase slightly from 1.9619(4) to 1.969 Å from 150 to 100 K, and the increase in the Ru-O distance corresponds to the metallic to semiconducting transition. On the other hand, the Tl-O distances decrease slightly from 2.449 to 2.439 Å from 300 to 150 K, and then split into two, shorter (2.422 Å) and longer (2.466 Å) distances below the metallic-semiconducting transition temperature. Larger splitting for the Tl sites may indicate charge disproportionation of the Tl ions. To address the electronic implications of these structural changes, valence bond sums and Madelung site potentials have been calculated using the program EUTAX [6-4]. Figure 6-4 illustrates the variation in the valence bond sums for Tl, Ru, and O(1), and O(2) as a function of temperature. The results obtained at 300 K were calculated from the TOF neutron diffraction data. Below the metallic-semiconducting transition temperature of 120 K, Tl and Ru sites divided into two sites. At 100 K, two Tl sites were 2.6 and 2.9, respectively, while the two Ru sites gave almost similar valence values. The valence sum calculation also suggests the charge disproportionation for the Tl at the metallic-semiconducting transition with $2Tl^{3+} \rightarrow Tl^{(3+)-\delta} + Tl^{(1+)+\delta}$. Figure 6-5 shows the structure of $Tl_2Ru_2O_7$ at 100 K. In this structure, Tl and Ru sites are divided into two sites with a 1:1 ratio. Two Tl sites correspond to $Tl^{(3+)-\delta}$ and $Tl^{(1+)+\delta}$ which are ordered one dimensionally.

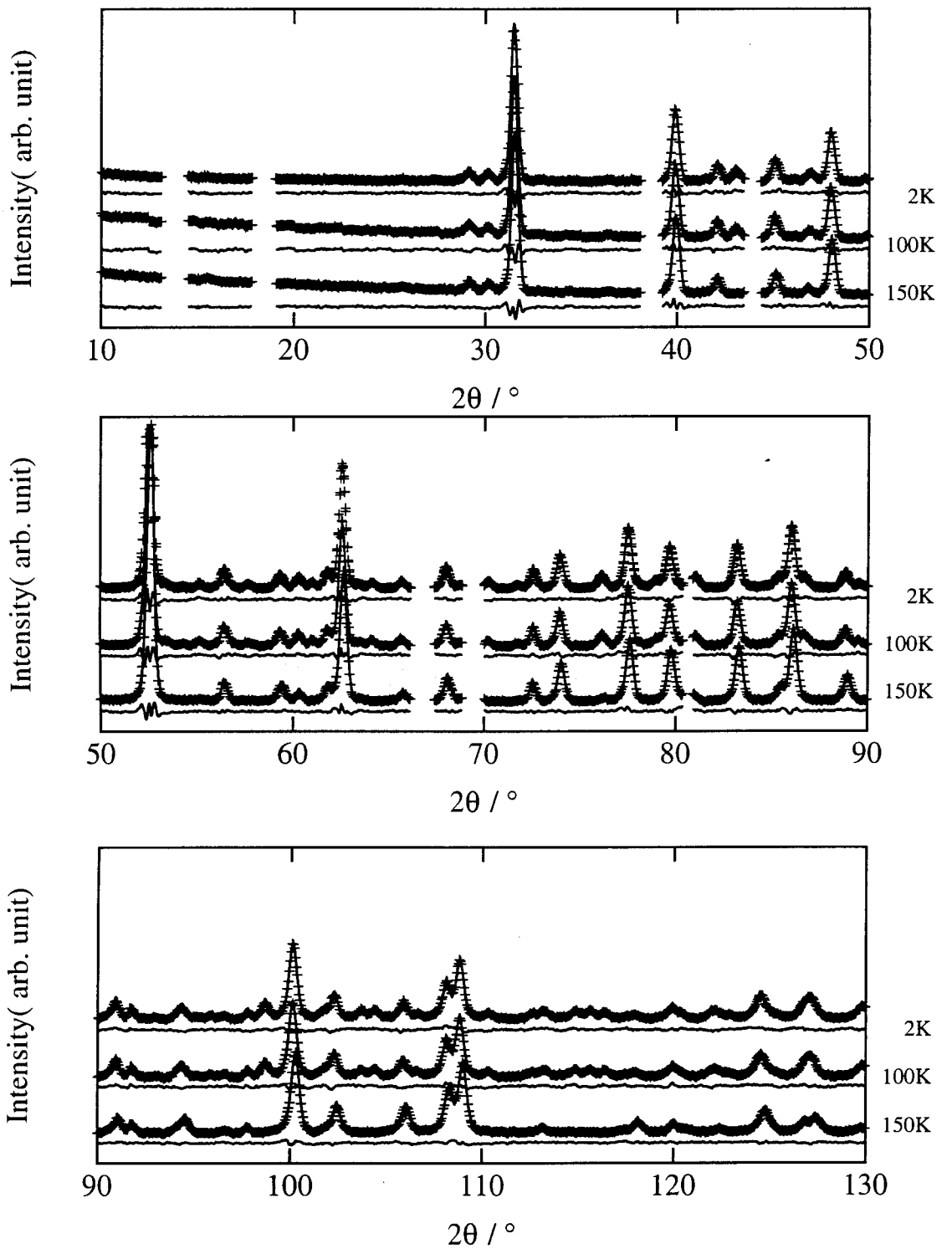

Fig. 6-1 Observed, calculated, and difference plots for the neutron Rietveld analysis for $Tl_2Ru_2O_7$ at 150 K, 100 K, and 2 K.

Table 6-3 Structural parameters for $Tl_2Ru_2O_7$ in *Pnma* at 100 K
(synthesized under high oxygen pressure, metallic-semiconducting transition at 120 K)

a=7.2022(4) Å, b=7.2051(5) Å, c=10.1815(7) Å, R_{wp}=3.47%, R_p=2.68%, R_R=10.57%
R_e=2.20%, R_I=2.50%, R_F=1.70%, $S=R_{wp}/R_e$=1.5746

Atom	Site	g	x	y	z	B_{eq} / Å^2
Tl(1)	4*a*	1.0	0	0	0.5	0.60(7)
Tl(2)	4*c*	1.0	0.2497(7)	0.25	0.7709(5)	0.24(10)
Ru(1)	4*a*	1.0	0.0	0.0	0.0	0.21(8)
Ru(2)	4*c*	1.0	0.2315(13)	0.25	0.2550(5)	0.51(11)
O(1)	4*c*	1.0	-0.0180(11)	0.25	0.3524(9)	0.27(3)
O(2)	4*c*	1.0	0.0064(12)	0.25	0.9274(9)	=O(1)
O(3)	8*d*	1.0	0.1761(6)	0.4395(8)	0.1342(7)	=O(1)
O(4)	8*d*	1.0	0.7792(8)	0.4538(8)	0.1222(6)	=O(1)
O(5)	4*c*	1.0	0.5173(10)	0.25	0.8745(12)	=O(1)

Structural parameters for $Tl_2Ru_2O_7$ in *Pnma* at 2 K
(synthesized under high oxygen pressure, Metallic-semiconducting transition at 120 K)

a=7.2022(3) Å, b=7.2060(5) Å, c=10.1802(6) Å, R_{wp}=3.70%, R_p=2.91%, R_R=9.68%
R_e=2.40%, R_I=2.35%, R_F=1.47%, $S=R_{wp}/R_e$=1.5404

Atom	Site	g	x	y	z	B_{eq} / Å^2
Tl(1)	4*a*	1.0	0	0	0.5	0.61(6)
Tl(2)	4*c*	1.0	0.2483(5)	0.25	0.7719(5)	0.10(8)
Ru(1)	4*a*	1.0	0.0	0.0	0.0	0.06(6)
Ru(2)	4*c*	1.0	0.2296(11)	0.25	0.2539(4)	0.33(9)
O(1)	4*c*	1.0	-0.0201(10)	0.25	0.35478)	0.15(3)
O(2)	4*c*	1.0	0.0063(10)	0.25	0.9301(7)	=O(1)
O(3)	8*d*	1.0	0.1748(6)	0.4416(7)	0.1342(6)	=O(1)
O(4)	8*d*	1.0	0.7798(7)	0.4561(7)	0.1218(6)	=O(1)
O(5)	4*c*	1.0	0.5172(9)	0.25	0.8759(10)	=O(1)

Table 6-4(a) Interatomic distances and bond angles for $Tl_2Ru_2O_7$

Temperature	100K	2K
Distances	*d* / Å	
Ru(1)-O(2) (×2)	1.948(3)	1.938(3)
Ru(1)-O(3) (×2)	1.914(7)	1.911(6)
Ru(1)-O(4) (×2)	2.046(7)	2.042(6)
average Ru(1)-O	1.969	1.964
Ru(2)-O(1)	2.052(12)	2.069(11)
Ru(2)-O(1)	2.110(13)	2.121(11)
Ru(2)-O(3) (×2)	1.880(7)	1.878(6)
Ru(2)-O(4) (×2)	1.959(7)	1.978(7)
average Ru(2)-O	1.973	1.984
Angles	*θ* / °	
O(2)-Ru(1)-O(4)	84.3(3)	84.5(3)
O(2)-Ru(1)-O(3)	87.4(2)	87.5(2)
O(3)-Ru(1)-O(4)	87.5(3)	87.7(2)
O(1)-Ru(2)-O(3)	97.5(5)	98.1(4)
O(1)-Ru(2)-O(4)	81.1(2)	81.0(2)
O(1)-Ru(2)-O(3)	81.0(4)	80.7(3)
O(1)-Ru(2)-O(4)	100.4(4)	100.2(3)
O(3)-Ru(2)-O(4)	84.9(3)	84.3(2)
O(3)-Ru(1)-O(3)	93.1(4)	94.4(3)
O(4)-Ru(1)-O(4)	97.1(4)	97.0(4)
Ru(1)-O(2)-Ru(1)	135.3(4)	136.7(4)
Ru(2)-O(1)-Ru(2)	119.9(5)	118.6(4)
Ru(1)-O(3)-Ru(2)	140.6(4)	139.8(3)
Ru(1)-O(4)-Ru(2)	130.3(3)	130.5(3)

Table 6-4(b) Interatomic distances and bond angles for $Tl_2Ru_2O_7$

Temperature	100K	2K
Distances	*d* / Å	
Tl(1)-O(1) (×2)	2.349(6)	2.333(5)
Tl(1)-O(3) (×2)	2.739(5)	2.746(4)
Tl(1)-O(4) (×2)	2.388(6)	2.390(5)
Tl(1)-O(5) (×2)	2.212(7)	2.207(6)
average Tl(1)-O	2.422	2.419
Tl(2)-O(2)	2.368(10)	2.377(9)
Tl(2)-O(2)	2.738(9)	2.766(8)
Tl(2)-O(3) (×2)	2.688(6)	2.682(5)
Tl(2)-O(4) (×2)	2.405(6)	2.390(5)
Tl(2)-O(5)	2.197(12)	2.207(10)
Tl(2)-O(5)	2.235(10)	2.238(8)
average Tl(2)-O	2.466	2.467

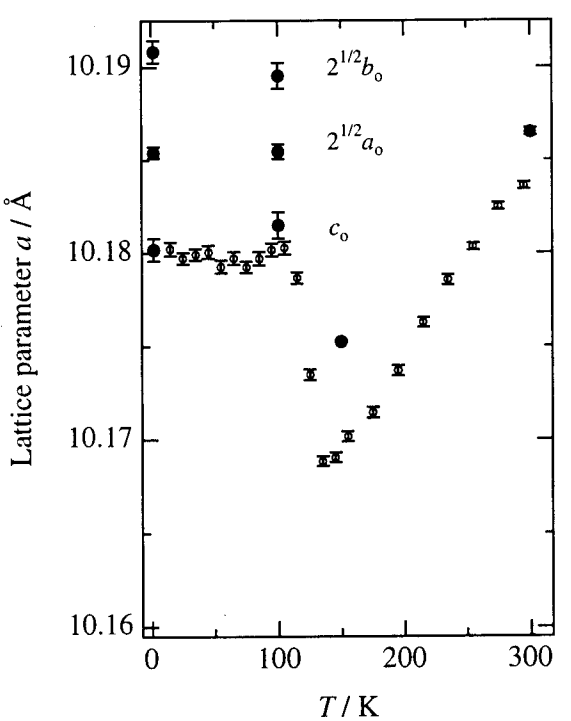

Fig. 6-2 Temperature dependence of the lattice parameters determeined by the X-ray (○) and neutron (●).

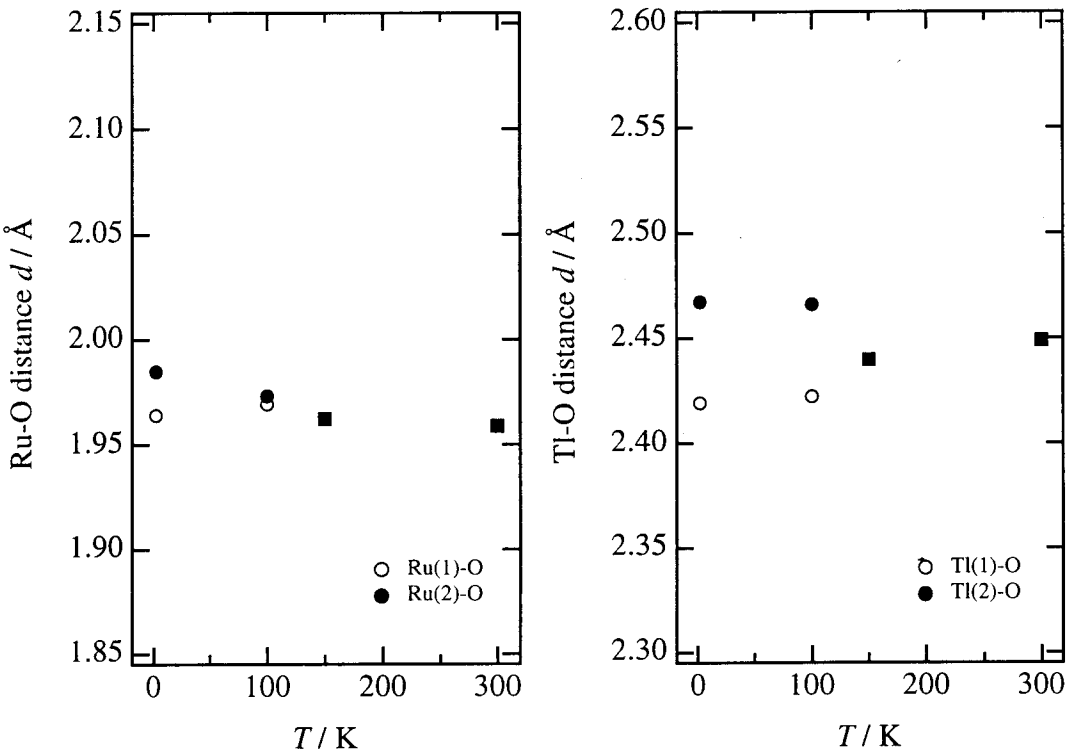

Fig. 6-3 Temperature dependence of the average bond distances.

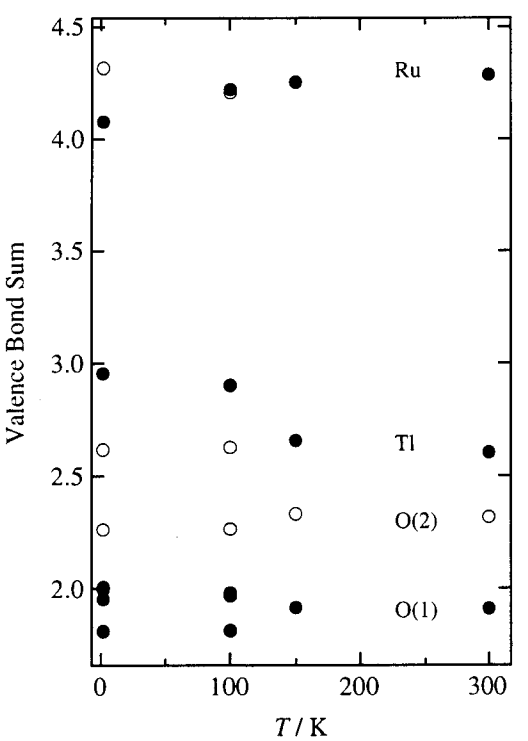

Fig. 6-4 Temperature dependence of the valance bond sums.

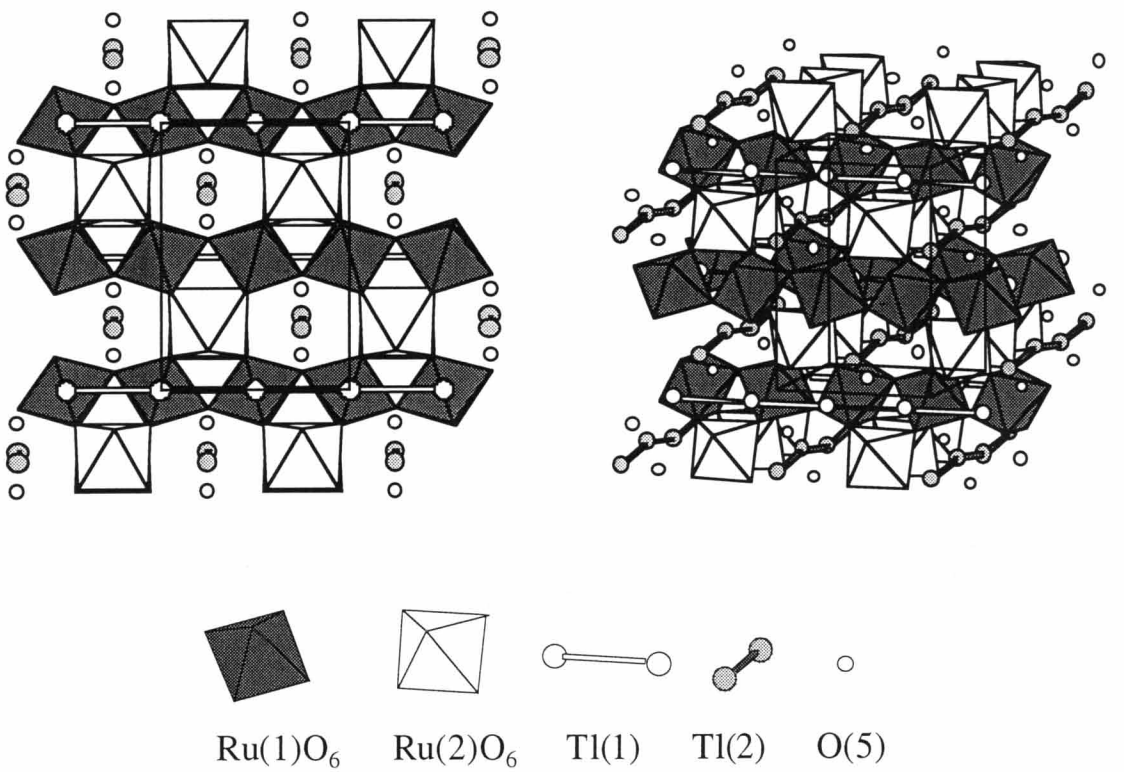

Fig. 6-5 Structure of $Tl_2Ru_2O_7$ at 100 K.

6-3 Discussion

Low temperature neutron diffraction measurements clarified the structural changes from $Fd\bar{3}m$ to *Pnma* at the transition temperature for $Tl_2Ru_2O_7$ synthesized under high oxygen pressure. The average bond distances and valence bond sums indicated that the thallium plays an important role in metallic-semiconducting transition. However, the magnetic interactions at the transition are not still clear. In order to investigate whether the transition is related to the magnetic interaction in the Ru sublattice, low temperature Mössbauer and μSR studies were performed. For the Mössbauer spectroscopy , a ^{57}Fe doped sample was used for the measurements. The composition of the sample was $Tl_2Ru_{1.96}{}^{57}Fe_{0.04}Ru_2O_7$. X-ray diffraction pattern of the sample indicated a single phase of the pyrochlore and no impurity phase was observed. The electrical resistivity and magnetric measurements showed the same behavior as $Tl_2Ru_2O_7$. Figure 6-6 shows the Mössbauer spectra for $Tl_2Ru_{1.96}{}^{57}Fe_{0.04}Ru_2O_7$ between 300 and 100 K. The spectra showed no magnetic peak below the transiton

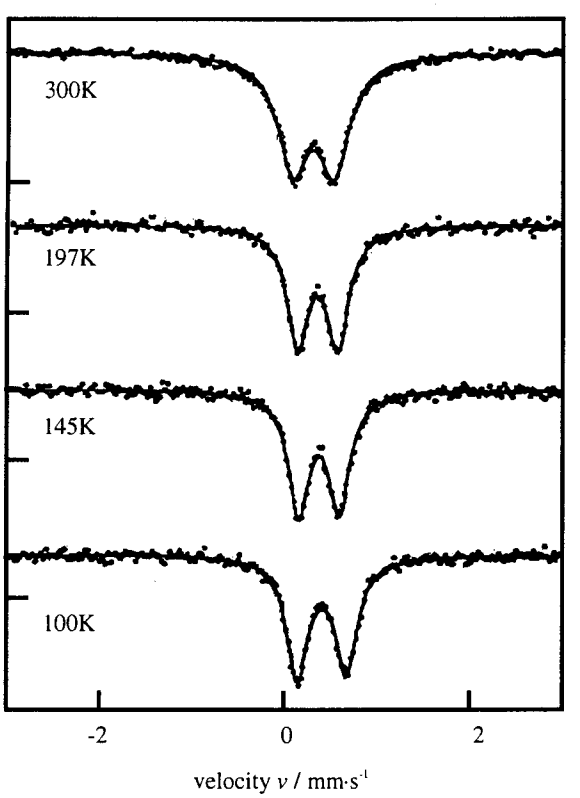

Fig. 6-6 Mössbauer spectra for $Tl_2Ru_{1.96}{}^{57}Fe_{0.04}Ru_2O_7$

temperature 120K. This indicated no magnetic transition occurred at the transition temperature 120 K. However, the quadropole splitting shown in Figure 6-7 increased at the transition temperatutre, which indicates symmetry reduction surrounding the iron, and this is consistent with the structural change from $Fd\bar{3}m$ to *Pnma* observed by neutron diffraction measurements. Isomer shift increased continuously with decreasing temperature.

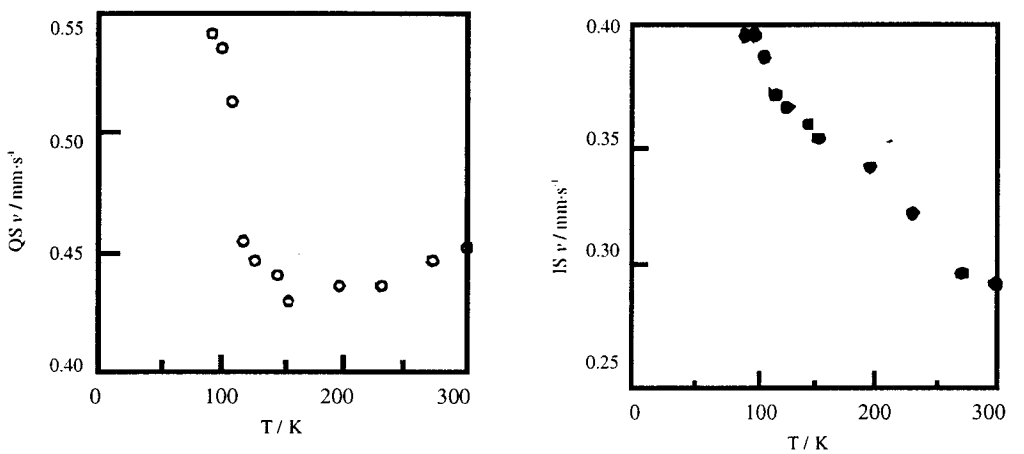

Fig. 6-7 Temperature dependence of the quadrupole splitting and isomer shift for $Tl_2Ru_{1.96}{}^{57}Fe_{0.04}Ru_2O_7$.

μSR is a powerful probe for determination of magnetic structure. When muon is put into the materials, it loses energy and stop in the lattice. After the average lift time of 2.2 μsec, muon disintegrates to positron e^+. The time dependence of the distribution of e^+ is measured, and the distribution is reflected by the internal magnetic field of that. For $Tl_2Ru_2O_7$, μSR spectra was measured between 295 K to 5 K at RIKEN-RAL muon facility at Rutherford Appleton Laboratory (RAL) in UK [5]. Figure 6-8 shows the spectra obtained at 295, 115, 20, and 5 K. Figure 6-9 shows the temperature dependence of the asymmetry. The asymmetry showed no apparent changes at the transition temperature of 120 K. However, it changed below 20 K. This indicated the transition at 120 K is not magnetic one, and below 20 K a new magnetic interaction occurs.

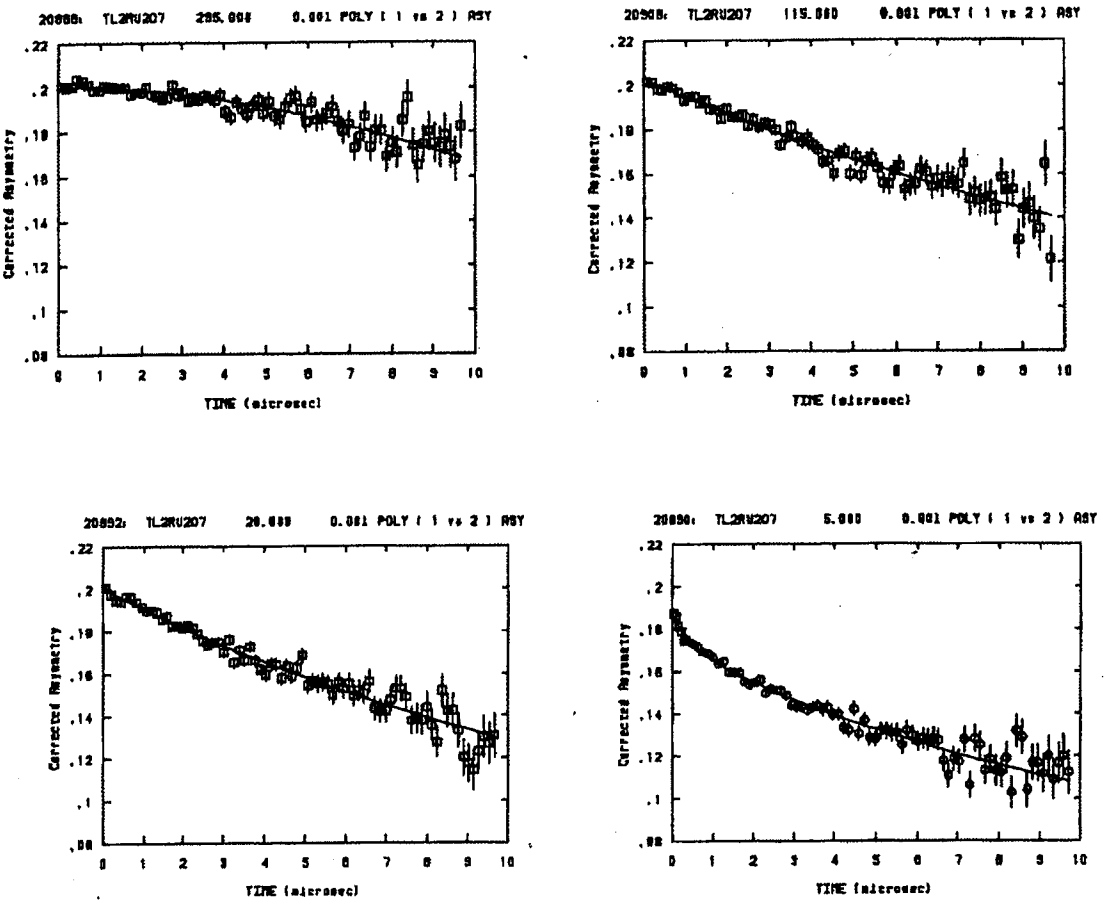

Fig. 6-8 ZF-μSR spectra for $Tl_2Ru_2O_7$ [5].

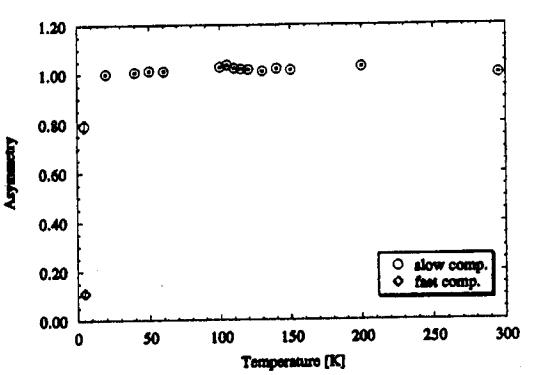

Fig. 6-9 Temperature dependence of the asymmetry for $Tl_2Ru_2O_7$ [5].

Both Mössbauer and μSR study showed that the transition at 120 K does not accompany any strong magnetic correlation, and these results are consistent with the neutron diffraction results that Tl plays an important role in metallic-semiconducting transition.

Previously, the electronic structure estimated by XPS, UPS and HREELS showed the 6*s* or 6*p* orbitals of *A* ion are close to E_F for $Pb_2Ru_2O_{6.5}$ and $Bi_2Ru_2O_7$ [6, 7, 8]. In thallim pyrochlore, there is a possibility that the Tl 6*s* or 6*p* orbitals are close to E_F because Tl has metallic property. Band calculations for $Tl_2Ru_2O_7$ and $Y_2Ru_2O_7$ were performed [9] by Ishii *et al.* by the Local Density Approximation (LDA) method. Figure 6-10 shows the total and partial density of state of $Tl_2Ru_2O_7$ and $Y_2Ru_2O_7$. The Ru *d* (t_{2g}) and O*p* antibonding state was observed near E_F in both calculations. Figure 6-11 shows the partial density of state in Tl and Y site. While the Tl-O-Ru antibonding state which is derived from Tl-6*s* orbital was observed near E_F for $Tl_2Ru_2O_7$, no such antibonding state was found for $Y_2Ru_2O_7$. These results indicate that Tl-6*s* orbital is located near E_F and metallic-semiconduicting transition is suggested to be caused by the splitting of this band.

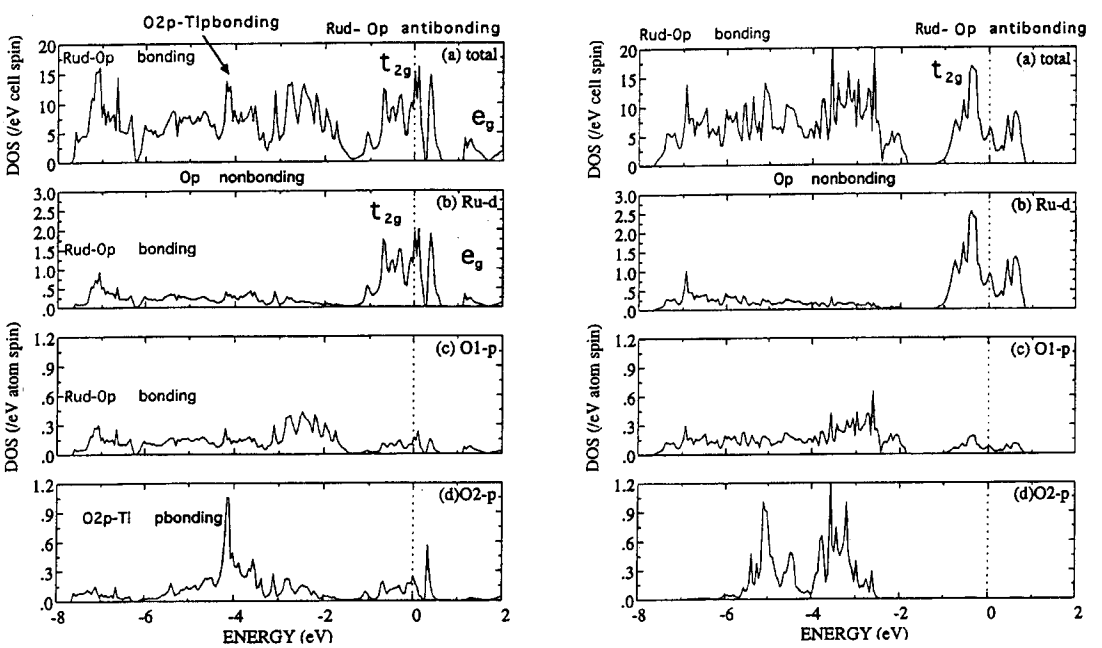

Fig. 6-10 The total density of state of $Tl_2Ru_2O_7$ and of $Y_2Ru_2O_7$. The Ru, O(1), and O(2) partial density of state are also shown [9].

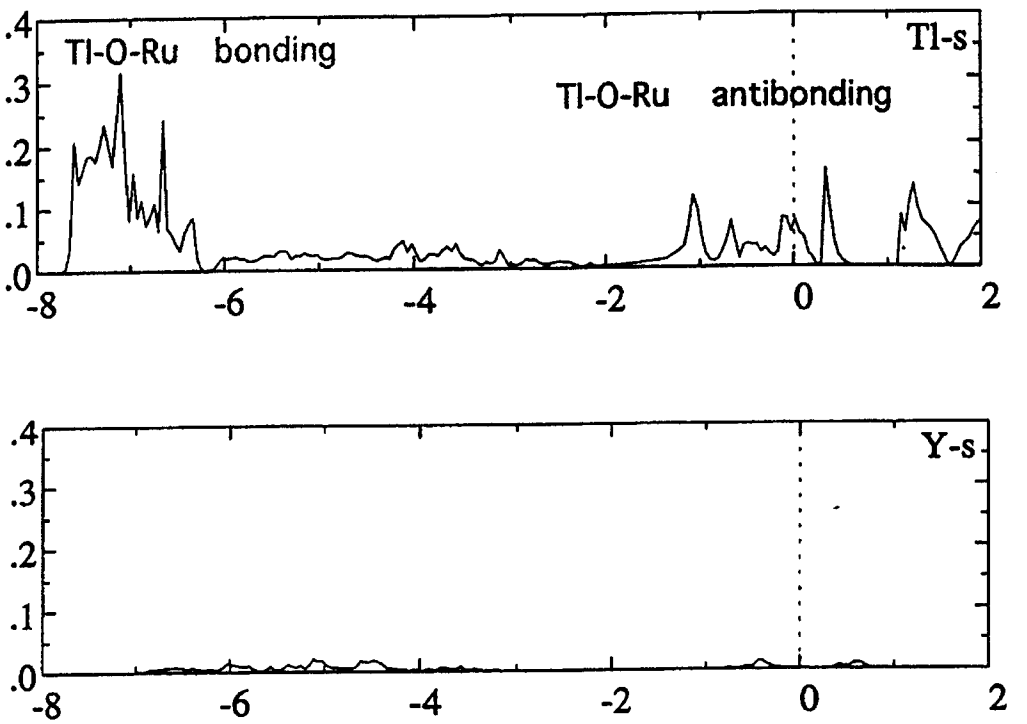

Fig. 6-11 The partial density of state in Tl site of $Tl_2Ru_2O_7$ and Y site of $Y_2Ru_2O_7$ [9].

Ultraviolet Photoemission Spectroscopy (UPS) and Bremsstrahlung Isochromat Spectroscopy (BIS) were performed for $Tl_2Ru_2O_7$ to study the band structure [10]. The valence band near the E_F is observed by UPS, and the conduction band is measured by BIS, respectively. Figure 6-12 shows the UPS and BIS spectra for $Tl_2Ru_2O_7$. The density of state decreased with decreasing temperature from 140 K to 50 K for UPS, and from 300 K to 80 K for BIS, successively. These results are consistent with the metallic-semiconducting transition observed by electrical conductivity measurements.

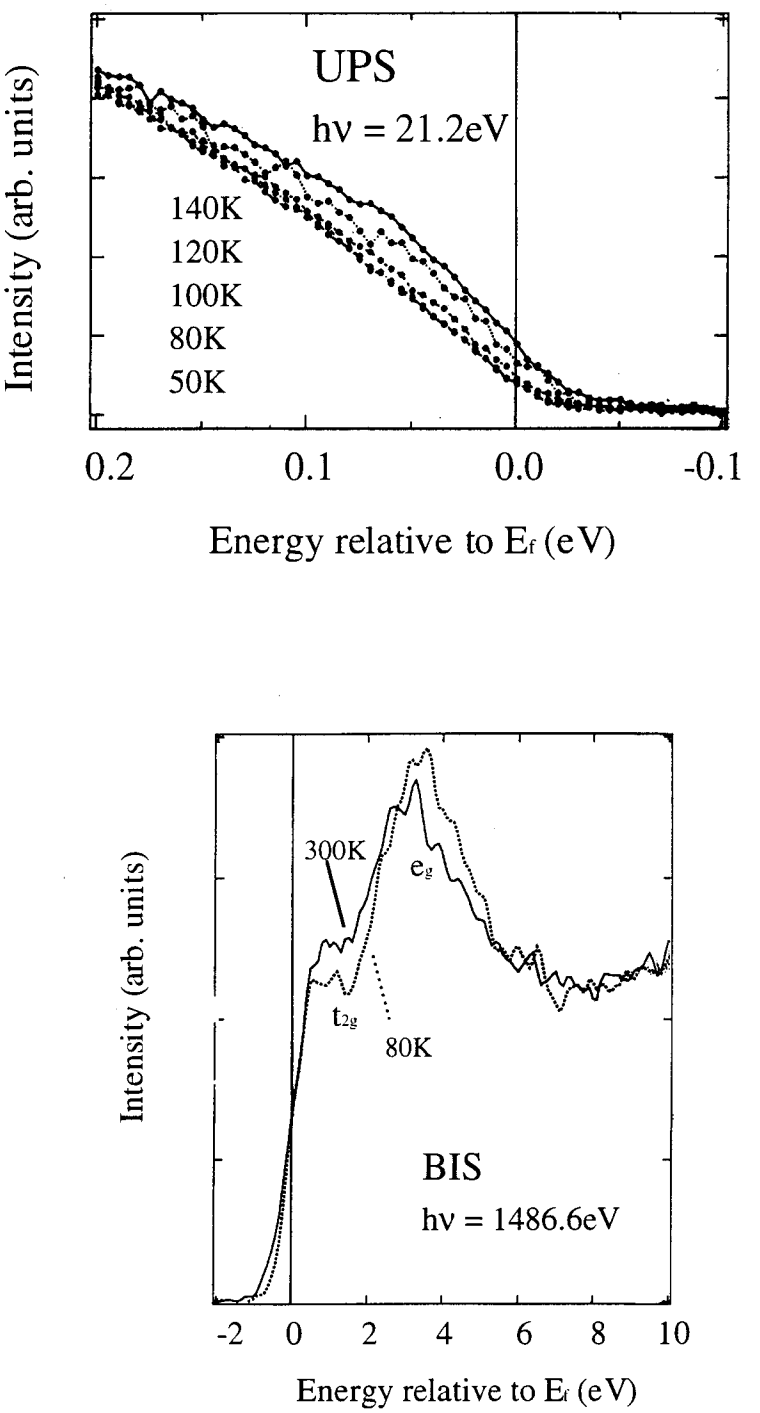

Fig. 6-12 UPS and BIS spectra for $Tl_2Ru_2O_7$. The spectra are ranged from the top (140K) to the bottom (50K) for UPS [10].

References

[1] M. Nagata, H .Kobayashi, R. Kanno, Y. Kawamoto, M. Takano, Abstract of the Physical Society of Japan, 49, Part 3, 470 (1994)

[2] G. Ferey, M. Leblanc, and R. De Pape, *J. Solid State Chem.*, **40**, 1 (1981)

[3] G. Ferey, M. Leblanc, R. De Pape, and J. Pannetier, *Solid State Commun.*, **53**, 559 (1985).

[4] M. O'Keeffe, "EUTAX", Version 1.3" EMlab Software, Phoenix, AZ, 1993

[5] K. Kakuta, K. Ohishi, H . Takagiwa, T. Yokoo, J. Akimitsu, W. Higemoto, R. Kadono, T. Takeda, R. Kanno, and M. Takano, Meeting Abstract of the Physical Society of Japan, 54, Issue 2, Part 3, 367 (1999)

[6] P. A. Cox, J. B. Goodenough, P. J. Tavener, D. Telles, and R. G. Egdell, *J. Solid State Chem.*, **62**, 360 (1986)

[7] P. A. Cox, R. G. Egdell, J. B. Goodenough, A. Hamnett, and C. C. Naish, *J. Phys. C*, **16**, 6221 (1983)

[8] W. Y. Hsu, R. V. kasowski, T. Miller, and T-C Chiang, *Appl. Phys. Lett.*, **52**, 792 (1988)

[9] F. Ishii, and T. Oguchi, Meeting Abstract of the Physical Society of Japan, 53, Issue 1, Part 3, 632 (1998)

[10] J. Okamoto, A. Fujimori, T. Takeda, R. Kanno, F. Ishii, and T. Oguchi, Meeting Abstract of the Physical Society of Japan, 54, Issue 2, Part 3, 449 (1999)

Chapter 7

Spin-glass like behavior in ruthenium containing pyrochlore

7-1 Introduction

Thallium pyrochlore $Tl_2Ru_2O_{6.96}$ with a small amount of oxygen vacancy shows the metallic–semiconsucting transition and spin-glass like behavior at 50 K. Pyrochlore structure is composed of three dimensional tetrahdra corner sharing network. Therefore, there is a possibility for frustration, just as 2D triangular, Kagomé, and 3D spinel structure. Indeed, some pyrochlore oxides show spin-glass like behavior (1, 2, 3) and short range magnetic interaction was observed by neutron diffraction measurements.

In the present study, low-temperature neutron diffraction measurements were performed to study the spin-glass like behavior. Furthermore, the relationship between oxygen vacancies and spin-glass like behavior, and the properties of $Y_2Ru_2O_7$, which has no magnetic contribution from *A* site, were studied.

7-2 Neutron diffraction at low temperatures

Neutron diffraction data were taken at 100 K and 2 K on an angle dispersion neutron powder diffractometer, D2B, at the ILL. At 100 K, the structure model $Fd\bar{3}m$ was used. The site ocuppation parameters, *g*, of the O(2) were refined to be 0.951(6). This is consistent with the result [g=0.96(3)] obtained from TOF neutron diffraction data at room temperature. Examination of the diffraction pattern at 2 K showed no evidence of superlattice reflections which indicated symmetry changes at the transition temperature, and no magnetic ordering was observed either. Table 7-1 lists final *R* factors, lattice and structural parameters with their estimated standard deviations in parentheses. Table 7-2 gives interatomic distances and bond angles. Figure 7-1 illustrates the profile fit and difference patterns for both samples. Figure 7-2 shows the temperature dependence of the lattice parameters for $Tl_2Ru_2O_{6.95}$. The results were obtained from both X-ray and neutron diffraction data. The parameters determined

using the neutron and X-ray diffraction data are consistent with each other. With decreasing temperature, the Tl-O(1) and Tl-O(2) distances decrease from 2.535(3) and 2.2047(1) Å (300 K) to 2.5172(7) and 2.2017(1) Å (2 K), respectively, while the Ru-O distance increases slightly from 1.9543(17) Å (300 K) to 1.9598(4) Å (2K). The Ru-O-Ru angle decrease from 134.2(2)° (300 K) to 133.07(5)° (2 K). These structural changes are consistent with the property change from metallic to semiconducting with decreasing temperature, and these changes are similar to those observed for other $A_2Ru_2O_7$ pyrochlores [4, 5].

Reimer *et al.* found short range magnetic ordering for the pyrochlores, $Tb_2Mo_2O_7$ and $Y_2Mo_2O_7$ [3], using the difference plots of the neutron diffraction data between the high temperature non-magnetic state and the low-temperature magnetic ordering state. Similar plots were examined using the diffraction data at 100 K and 2 K. However, no significant peaks were observed in the difference plots.

Table 7-1(a) Structural parameters for $Tl_2Ru_2O_{7-\delta}$ in $Fd\bar{3}m$ at 100 K
(synthesized under high pressure, metallic-semiconducting transition at 50 K)
(a=10.17179(3) Å, R_{wp}=3.75%, R_p=2.80%, R_I=2.61%, R_F=1.90, S=R_{wp}/R_e=1.54)

Atom	Site	g	x	y	z	B_{eq} / Å^2
Tl	16*d*	1.0	1/2	1/2	1/2	0.36
Ru	16*c*	1.0	0.0	0.0	0.0	0.36
O(1)	48*f*	1.0	0.3263(4)	1/8	1/8	0.51
O(2)	8*b*	0.951	3/8	3/8	3/8	0.43
Atom	U_{11} / Å^2	U_{22} / Å^2	U_{33} / Å^2	U_{12} / Å^2	U_{13} / Å^2	U_{23} / Å^2
Tl	0.0045(3)	= U_{11}	= U_{11}	0.0003(11)	= U_{12}	= U_{12}
Ru	0.0045(3)	= U_{11}	= U_{11}	-0.0005(15)	= U_{12}	= U_{12}
O(1)	0.011(2)	0.0044(12)	= U_{22}	0	0	-0.0017(16)
O(2)	0.0043(8)	= U_{11}	= U_{11}	0	0	0

Table 7-1(b) Structural parameters for $Tl_2Ru_2O_{7-\delta}$ in $Fd\bar{3}m$ at 2 K
(synthesized under high pressure, metallic-semiconducting transition at 50 K)
(a=10.16730(3) Å, R_{wp}=3.62%, R_p=2.78%, R_I=2.58%, R_F=2.21, S=R_{wp}/R_e=1.55)

Atom	Site	g	x	y	z	B_{eq} / Å^2
Tl	16*d*	1.0	1/2	1/2	1/2	0.20
Ru	16*c*	1.0	0.0	0.0	0.0	0.31
O(1)	48*f*	1.0	0.3268(4)	1/8	1/8	0.47
O(2)	8*b*	0.951	3/8	3/8	3/8	0.43
Atom	U_{11} / Å^2	U_{22} / Å^2	U_{33} / Å^2	U_{12} / Å^2	U_{13} / Å^2	U_{23} / Å^2
Tl	0.0025(11)	= U_{11}	= U_{11}	0.0010(11)	= U_{12}	= U_{12}
Ru	0.0040(9)	= U_{11}	= U_{11}	-0.0007(14)	= U_{12}	= U_{12}
O(1)	0.011 (2)	0.0034(11)	= U_{22}	0	0	0.0011(15)
O(2)	0.0043(8)	= U_{11}	= U_{11}	0	0	0

Note. Numbers in parentheses are estimated standard deviations of the last significant digit.
The form of the anisotropic temperature factor is

$$\exp\left[-2\pi^2\left(h^2a^{*2}U_{11}+k^2b^{*2}U_{22}+l^2c^{*2}U_{33}+2hka^*b^*U_{12}+2hla^*c^*U_{13}+2klb^*c^*U_{23}\right)\right].$$

Table 7-2 Interatomic distances and bond angles for $Tl_2Ru_2O_{6.95}$

Coordinate triplets: i)x, y+1/2, z+1/2; ii)x-1/4, y+1/4, -z;
iii)-x+1/4, -y+1/4, z; iv)-x+1/4, y, -z+1/4; v)-x, -y+3/4, -z+3/4
vi)x, y-1/2, z-1/2; vii)-x+3/4, y, -z+3/4; viii)-z, x-1/4, y-1/4

Temperature	100 K	2 K
Distances	d / Å	
Tl-O(1^{i}) (×6)	2.535(3)	2.530(3)
Tl-O(2) (×2)	2.2047(1)	2.2054(1)
Ru-O(1^{ii}) (×6)	1.9543(17)	1.9586(18)

Angles	θ / °	
Ru^{iii}-O(1)-Ru^{iv}	134.2(2)	133.7(2)
Tl^{v}-O(1)-Tl^{iv}	90.48(14)	90.78(15)
Tl^{v}-O(2)-Tl^{vii}	109.4712	109.4712
O(1^{ii})-Ru-O(1^{viii})	94.75(15)	95.09(17)

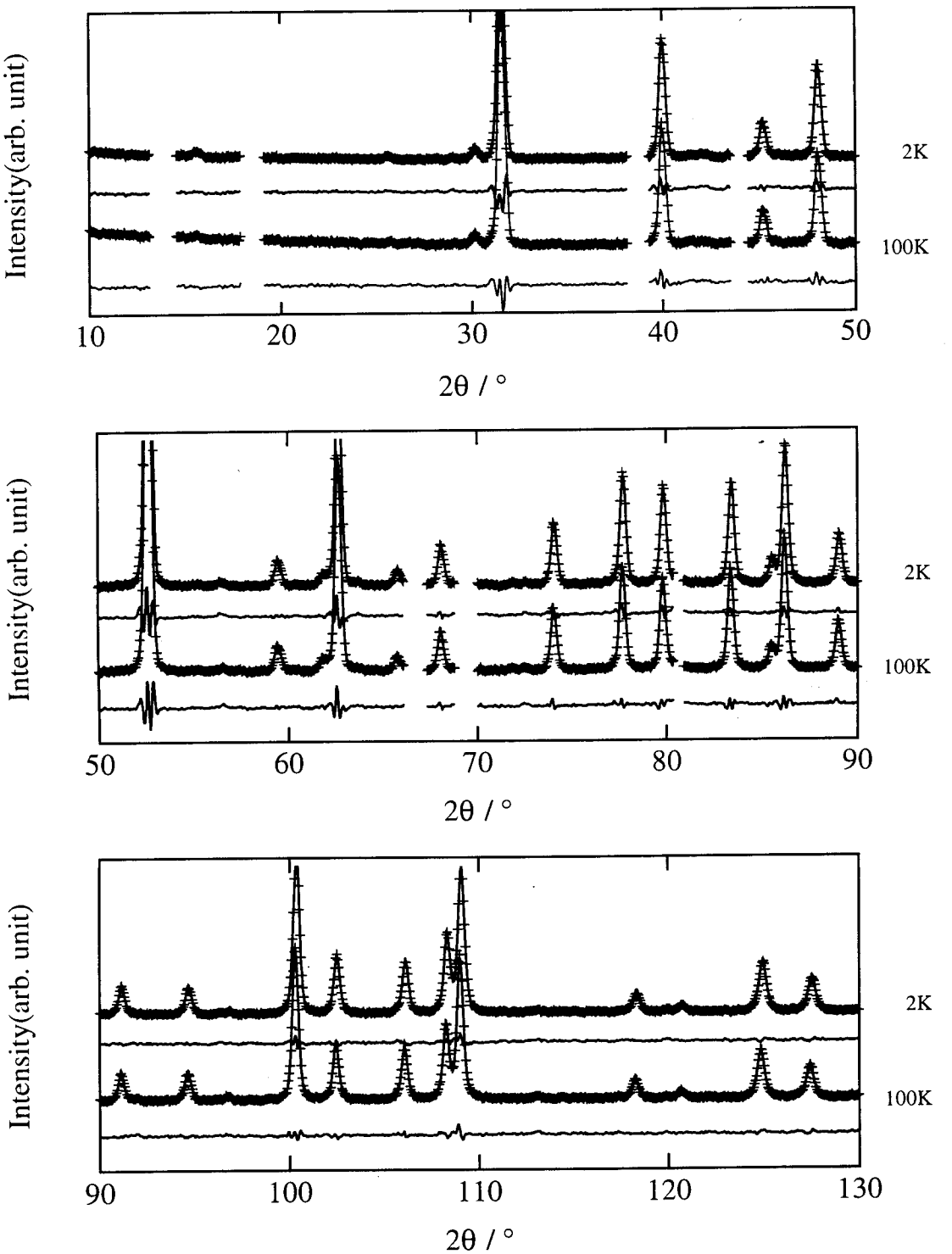

Fig. 7-1 Observed, calculated, and difference plots fors the neutron Rietveld analysis for $Tl_2Ru_2O_{6.95}$ at 100 K , and 2 K.

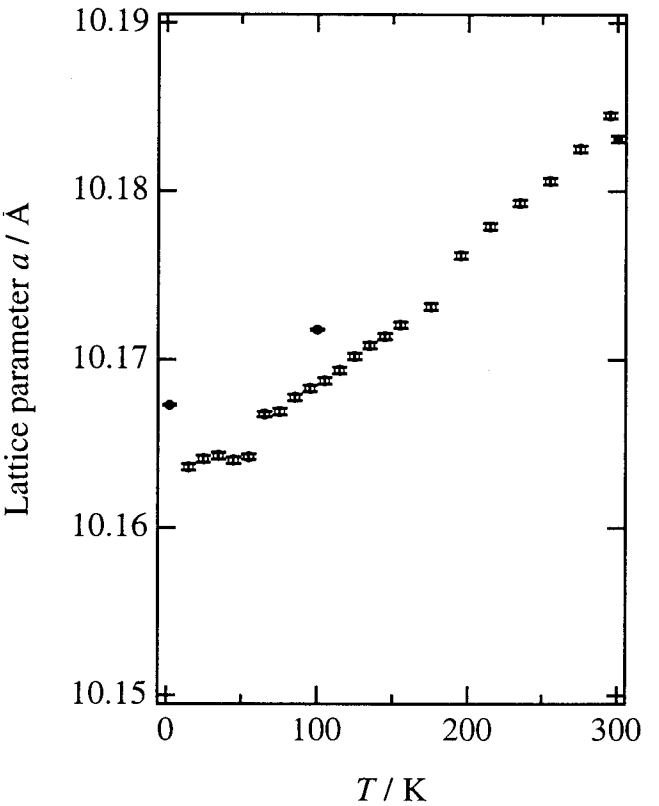

Fig. 7-2 Temperature dependence of the lattice parameter determined by the X-ray (○) and neutron (●).

7-3 Spin-glass like behavior in thallium pyrochlore

Although the pyrochlore with a small amount of oxygen vacancy showed spin-glass like behavior, the effect of the oxygen vacancy on the structure disorder to the spin-glass transition is not clear. To elucidate the relationship between oxygen vacancy and spin-glass like behavior, magnetic susceptibility measurements were performed for the ruthenium pyrochlores synthesized using ambient pressure, and stoichiometric pyrochlore synthesized under high oxygen pressure.

Figure 7-3 shows the temperature dependence of the magnetic susceptibility for these pyrochlores. High temperature phase showed no difference in M / H between fc and zfc measurement. Low temperature phase showed the difference in M / H between in zfc and fc at 40 K together with a M / H value decrease at 120 K. Although the

metallic-semiconducting transition was not observed for this sample by electrical conductivity measurement, the magnetic anomaly corresponding to the metallic-semiconducting transition was observed. This indicates that the sample is

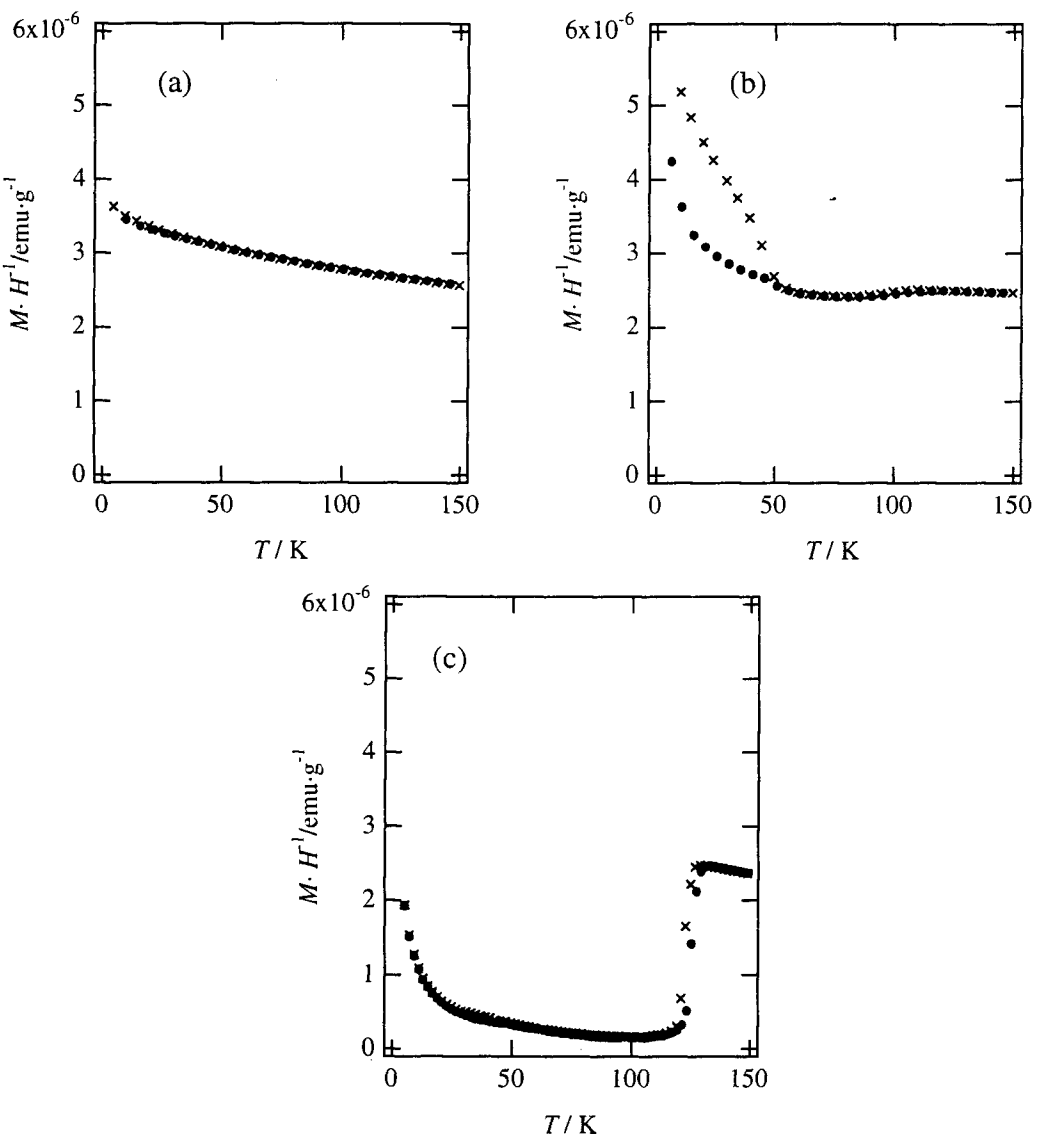

Fig. 7-3 Temperature dependence of the magnetic susceptibility for thallium pyrochlores synthesized under ambient pressure, high temperature phase (a), low temperature phase (b), and high oxygen pressure (c). ●zero field cooled ×field cooled

stoichiometric, and only a small domain of the sample may behave a semiconducting phase without long range ordering of the charge disproportionation of Tl. High oxygen pressure phase showed a slight difference between zfc and fc in the M/H curve around 40 K together with the magnitization drop corresponding to the metallic semiconducting transition at 120 K. These results indicated that the thallium pyrochlores with a small amount of oxygen vacancy and no oxygen vacancy show spin-glass like behavior.

To elucidate the relationships between oxygen vacancy and spin-glass like behavior, the oxygen deficient thallium pyrochlores $Tl_2Ru_2O_{7-\delta}$ was synthesized under high pressure in reducing condition using Ru metal. The nominal oxygen composition was varied from 6.9 to 6.5. Figure 7-4 shows the X-ray diffraction patterns for the oxygen deficient thallium pyrochlores $Tl_2Ru_2O_{7-\delta}$. For the sample with composition $Tl_2Ru_2O_{6.8}$, RuO_2 and an unknown phase were observed. Figure 7-5 shows the composition dependence of the lattice parameter obtained from Rietveld refinement. The lattice parameter increased with oxygen content from 7.0 to 6.7, corresponding to the increase in the oxygen vacancy. However, no change was observed between δ=0.3 and 0.5. Figure 7-6 shows the temperature dependence of the magnetic susceptibility for the oxygen deficient thallium pyrochlores $Tl_2Ru_2O_{7-\delta}$. Figure 7-7 shows the oxygen content dependence of the transition temperature. In the region $0.1 \leq \delta \leq 0.25$, spin-glass like behavior was observed, and the transition temperature decreased with oxygen deficiency. In the region $0.3 \leq \delta \leq 0.5$, no maganetic transition was observed. These results indicated that the thallium pyrochlores show spin-glass like behavior, the transition temperature decreases with increasing oxygen vacancy and disappears at δ = 0.3. However, these results are not consistent with the magnetic behavior observed in 2D triangular lattice [6], in which the transition temperature decreases with decreasing non-stoichiometry.

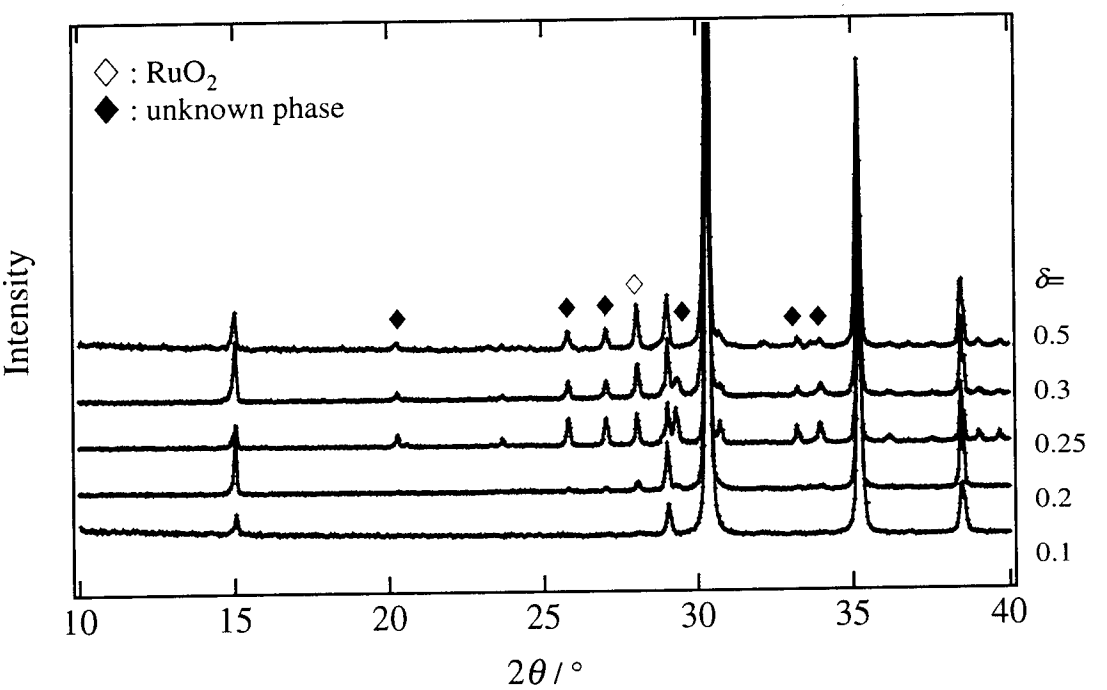

Fig. 7-4 X-ray diffraction patterns for oxygen deficient thallium pyrochlores $Tl_2Ru_2O_{7-\delta}$.

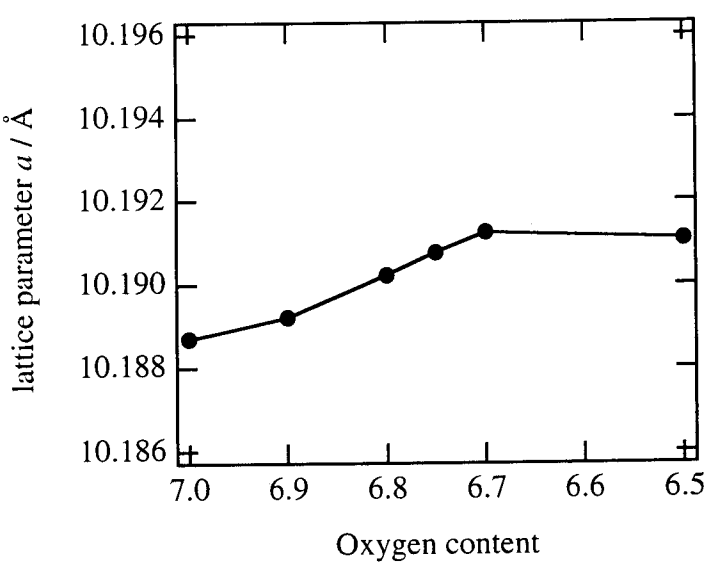

Fig. 7-5 Oxygen content dependence of the lattice parameter.

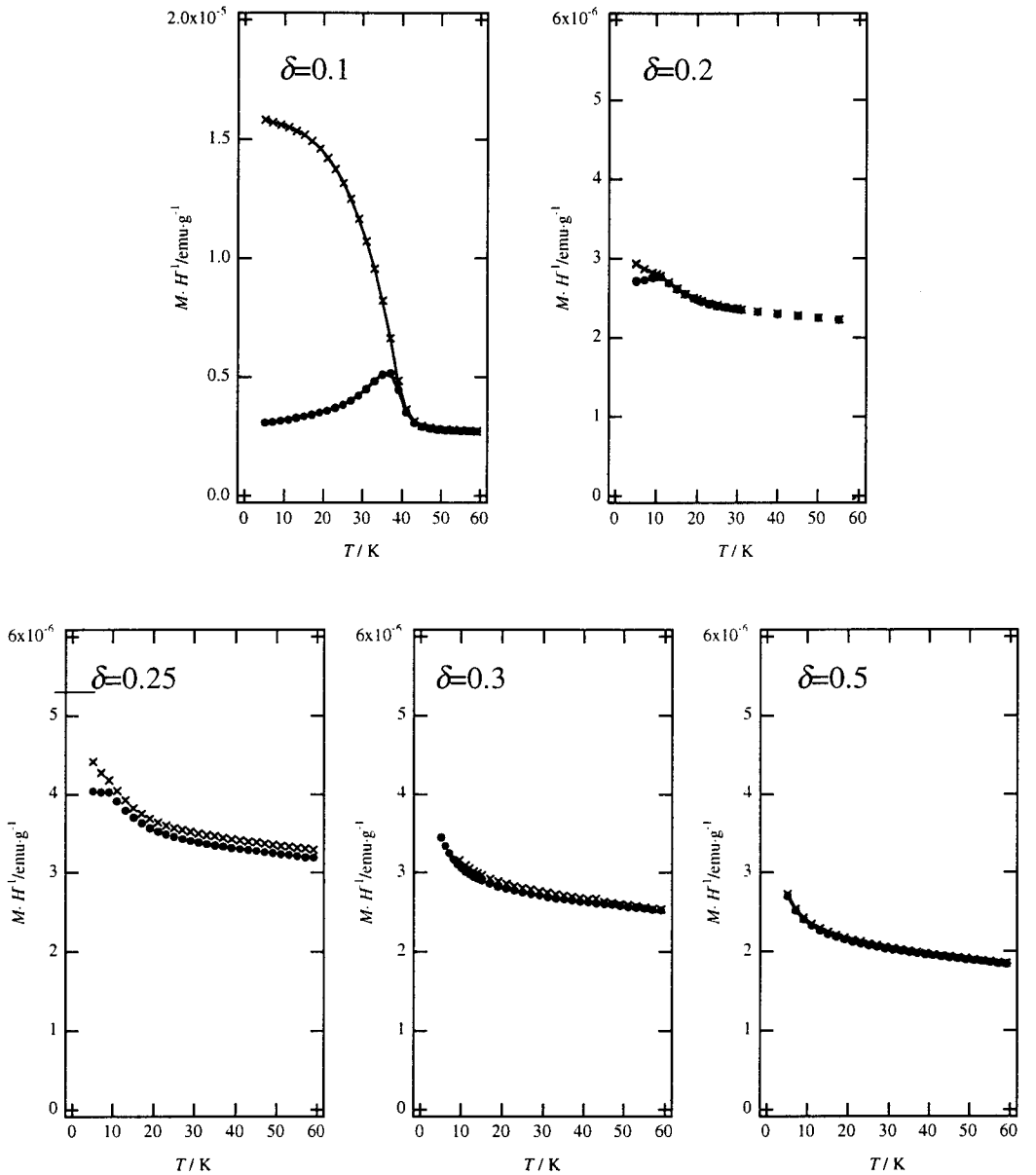

Fig. 7-6 Temperature dependence of the magnetic susceptibility for the oxygen deficient thallium pyrochlores $Tl_2Ru_2O_{7-\delta}$.

"":Nominal composiotion ●zero field cooled ×field cooled

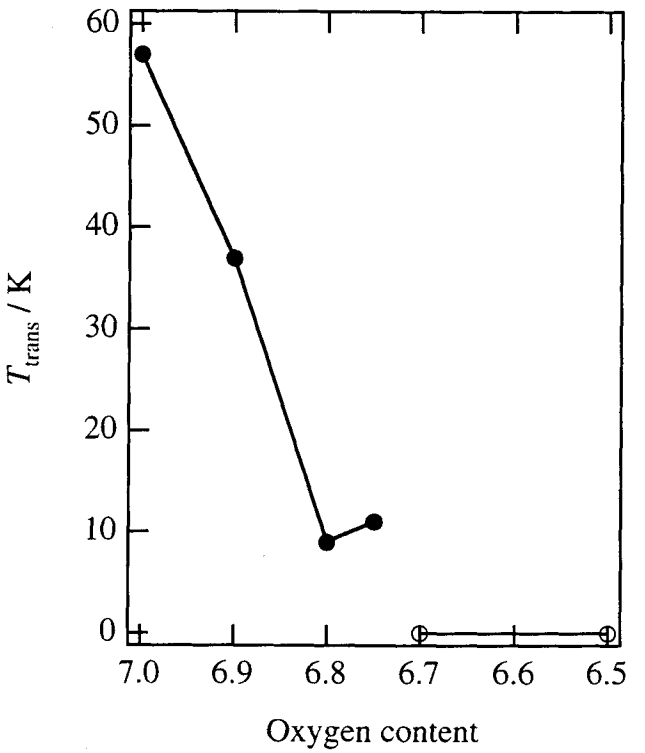

Fig. 7-7 Oxygen content dependence of the transition temperature.

7-4 Properties of $Y_2Ru_2O_7$

The electronic property of the thallium pyrochlore is affectecd by the Ru 4*d* and Tl 6*s* band and the band overlap of Tl 6*s* band is significant in its metallic conduction. On the other hand, the spin-glass like behavior is also observed for the thallium pyrochlores. The origin of the spin glass-like behavior might be (i) the ruthenium lattice with electrons from Ru 4*d* band, (ii) band overlap between Ru 4*d* and Tl 6*s* which is the same as its electronic conduction. Therefore, it is important to clalify the magnetic property of the ruthenium pyrochlore which has no contribution from *A* ion. $Y_2Ru_2O_7$ is reported to be semiconducting [7], where Y^{3+} has no *f*-electrons. In this study, the structure was determined using neutron diffraction and magnetic properties were examined. Neutron diffraction data was collected at room temperature on a time-of-flight (TOF) neutron powder diffractometer, SEPD, at IPNS.

The refinement results are indicated in Table 7-3. Bond distances and angles are shown in Table 7-4. Figure 7-8 illustrates the profile fit and difference pattern. Figure 7-9 shows the temperature dependence of the electrical conductivity and magnetic susceptibility for $Y_2Ru_2O_7$. Semiconducting behavior and spin-glass behavior at 80 K were observed. These results indicated that the origin of the spin-glass like behavior is the Ru tetrahedra in the ruthenium pyrochlores.

Table 7-3 Structural parameters for $Y_2Ru_2O_7$ in $Fd\bar{3}m$ at RT
(a=10.14020(15) Å, R_{wp}=6.19%, R_p=4.11%, S=R_{wp}/R_e=1.498)

Atom	Site	g	x	y	z	B_{eq} / Å^2
Tl	16*d*	1.0	1/2	1/2	1/2	0.64
Ru	16*c*	1.0	0.0	0.0	0.0	0.44
O(1)	48*f*	1.0	0.33543(6)	1/8	1/8	0.65
O(2)	8*b*	1.0	3/8	3/8	3/8	0.40
Atom	U_{11} / Å^2	U_{22} / Å^2	U_{33} / Å^2	U_{12} / Å^2	U_{13} / Å^2	U_{23} / Å^2
Tl	0.00640(15)	= U_{11}	= U_{11}	-0.00084(18)	= U_{12}	= U_{12}
Ru	0.00437(12)	= U_{11}	= U_{11}	-0.00001(18)	= U_{12}	= U_{12}
O(1)	0.0060(2)	0.0068(17)	= U_{22}	0	0	0.0025(2)
O(2)	0.0040(2)	= U_{11}	= U_{11}	0	0	0

Note. Numbers in parentheses are estimated standard deviations of the last significant digit.
The form of the anisotropic temperature factor is

$$\exp\left[-2\pi^2\left(h^2a^{*2}U_{11}+k^2b^{*2}U_{22}+l^2c^{*2}U_{33}+2hka^*b^*U_{12}+2hla^*c^*U_{13}+2klb^*c^*U_{23}\right)\right].$$

Table 7-4 Interatomic distances and bond angles for $Y_2Ru_2O_7$

Coordinate triplets: i)x, y+1/2, z+1/2; ii)x-1/4, y+1/4, -z; iii)-x+1/4, -y+1/4, z; iv)-x+1/4, y, -z+1/4; v)-x, -y+3/4, -z+3/4 vi)x, y-1/2, z-1/2; vii)-x+3/4, y, -z+3/4; viii)-z, x-1/4, y-1/4	
Distances	d / Å
Y-O(1^{i}) (×6)	2.4496(4)
Y-O(2) (×2)	2.19543(2)
Ru-O(1^{ii}) (×6)	1.9906(3)
Angles	θ / °
Ru^{iii}-O(1)-Ru^{iv}	128.45(3)
Y^{v}-O(1)-Y^{iv}	94.07(2)
Y^{v}-O(2)-Y^{vii}	109.4712
O(1^{ii})-Ru-O(1^{viii})	98.53(2)

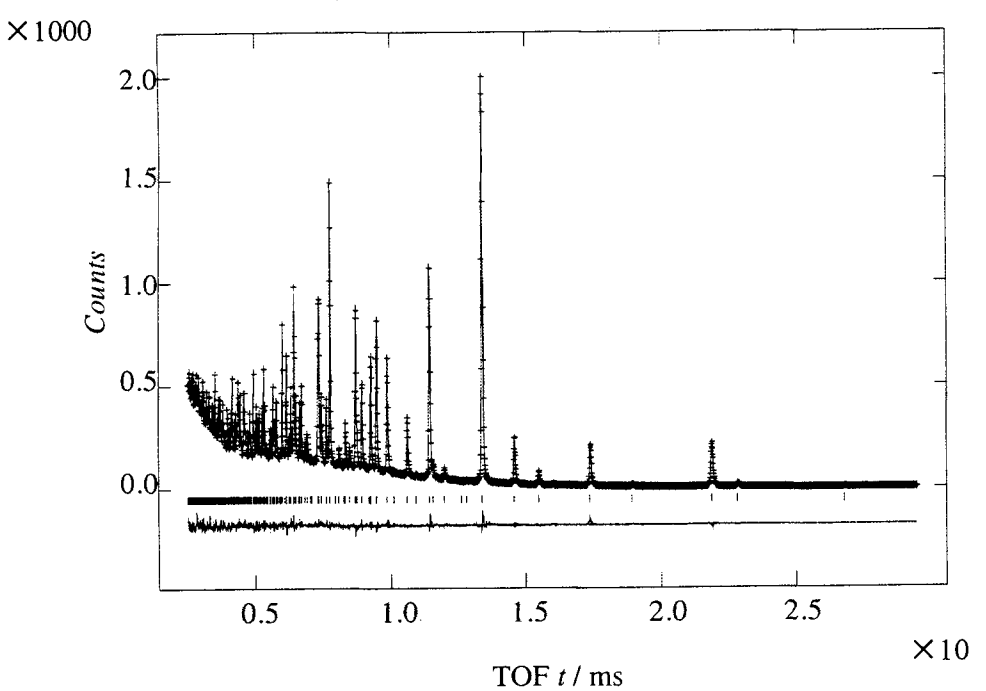

Fig. 7-8 Observed, calculated, and difference plots for the neutron Rietveld analysis for $Y_2Ru_2O_7$ at RT.

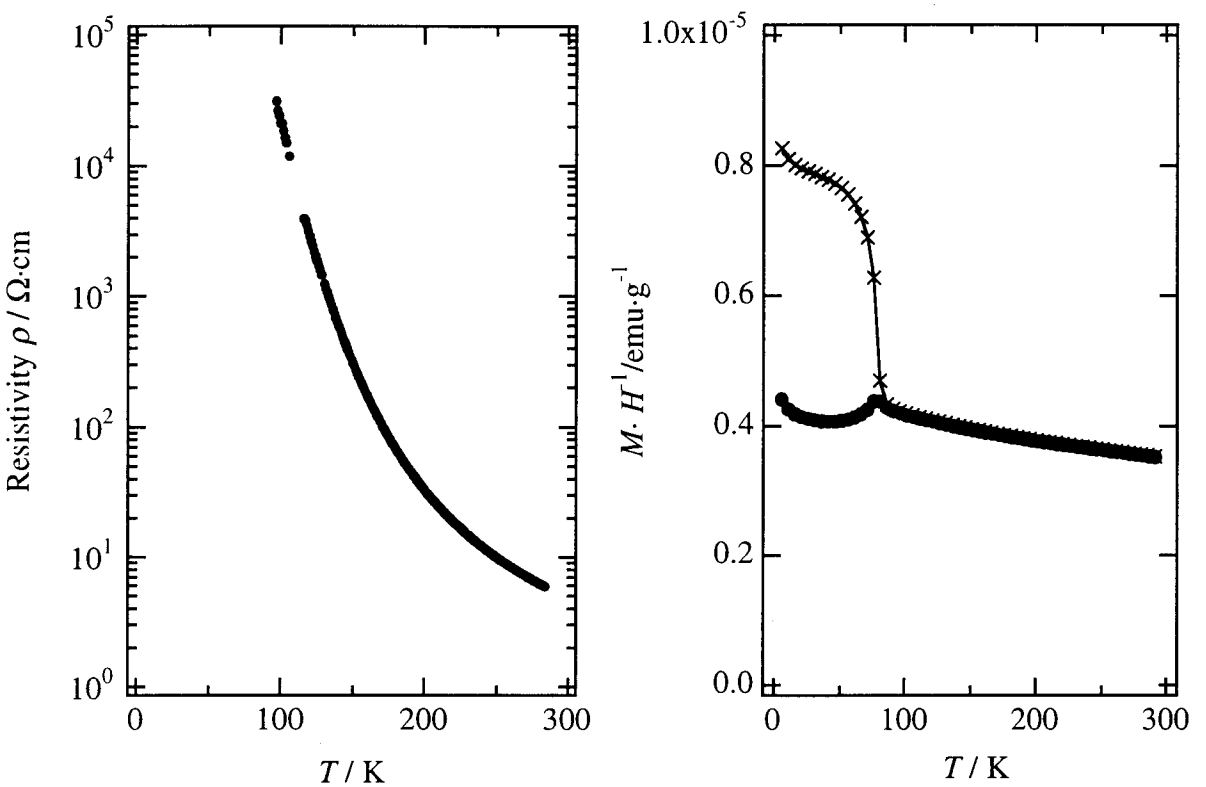

Fig. 7-9 Temperature dependence of the electrical conductivity and magnetic susceptibility for $Y_2Ru_2O_7$. ●zero field cooled ×field cooled

References

[1] J. S. Gardner, B. D. Gaulin, S. –H. Lee, C. Broholm, N. P. Raju, and J. E. Greedan, *Phys. Rev. Lett.*, **83**, 211 (1999)

[2] N. P. Raju, M. Dion, M. J. P. Gingras, T. E. Mason, and J. E. Greedan, *Phys. Rev. B*, **59**, 14489 (1999)

[3] J. E. Greedan, J. N. Reimers, C. V. Stager, and S. L. Penny, *Phys. Rev. B*, **43**, 5682 (1991)

[4] Y. Yamamoto, R. Kanno, Y. Takeda, O. Yamamoto, Y. Kawamoto, and M. Takano, *J. Solid State Chem.*, **109**, 372 (1994)

[5] H. Kobayashi, R. Kanno, Y. Kawamoto, T. Kamiyama, F. Izumi, and A. W. Sleight, *J. Solid State Chem.*, **114**, 15 (1995)

[6] H. Hirakawa, H. Kadowaki, and K. Ubukoshi, *J. Phys. Soc. Jpn.*, **54**, 3526 (1985)

[7] R. Kanno, Y. Takeda, T. Yamamoto, Y. Kawamoto, and O. Yamamoto, J. *Solid State Chem.* **102**, 106 (1993)

Chapter 8

Electrode properties of ruthenium oxides for Solid Oxide Fuel Cell

8-1 Introduction

Solid Oxide Fuel Cells (SOFCs) are of great interest because of the simplicity of system design and availability of high quality by-product heat. Yttria Stabilized Zirconia (YSZ) has been used as the oxygen ion electrolyte. YSZ works well at high temperature (0.1 $S \cdot cm^{-1}$ at 1000 °C). Other material (cathode, anode and, interconnector) have to endure high temperature. Although cerium oxides [1] and gallium oxides [2] have been studied as the oxygen ion conductor, YSZ is still the best material because of its stability and high oxygen ion conductivity.

There are some basic requirements for cathode material: high electron conductivity, thermal and chemical stability, sufficient porosity, good adherence at the surface of the electrolyte and the catalytic activity for the oxygen decomposition. 3*d*-transition metal perovskites $LaMO_3$ (M = Cr, Mn, Fe, Co) and their solid solution with alkaline earth metals in La site $La_{1-x}A_xMO_3$ have been studied [3]. $La_{1-x}Sr_xCoO_3$ system [4] showed the highest catalytic activity and electron conductivity. However, it reacts with YSZ to form the low-conductivity products. $La_{1-x}Sr_xMnO_3$ system [5] has been also studied extensively due to their stability at high temperatures and thermal expansion compatibility with YSZ. However, during long annealing times, a pyrochlore forms at the boundary between perovskite and the YSZ. Therefore, better electrodes that are less reactive with YSZ and have high stability at high temperatures are required.

In the present study, ruthenium pyrochlore and perovskite oxides were studied as the cathode materials for SOFC. The synthesis of their electrode, their catalytic activity, and physical and chemical properties were investigated.

8-2 Synthesis of electrode

$Pb_2Ru_2O_{6.5}$, $Bi_2Ru_2O_7$, $CaRuO_3$, and $SrRuO_3$ were prepared by heating appropriate molar ratios of PbO, Bi_2O_3, $CaCO_3$, $SrCO_3$, and RuO_2. They were mixed, pelleted and calcined at 600°C for pyrochlores and at 950°C for perovskites, respectively. After regrinding, they were pressed into pellets again, and fired at 900°C for pyrochlores and at 1200°C for perovskites, respectively. Pyrochlore and perovskite thin films were prepared on one side of 8YSZ tablet by the RF-sputtering, and fired at 900 – 1000°C. For $Pb_2Ru_2O_{6.5}$, the sample heated at 900°C showed the pattern of a pyrochlore structure with a small amount of impurity phases, RuO_2 and an unknown phase. At 1000°C, $Pb_2Ru_2O_{6.5}$ decomposed and only the RuO_2 phase appeared. For $Bi_2Ru_2O_7$, the X-ray diffraction patterns of the sample heated at 900 – 1000°C indicated the pyrochlore structure and no decomposition was observed. For $CaRuO_3$ and $SrRuO_3$, the perovskite phases appeared after these materials were heated at 1000°C. The SEM measurements of the electrodes baked on a YSZ disk indicated a porous surface, and the electrode were about 3 μm thick, which was estimated by the weight change during the sample preparation.

8-3 Catalytic activity

The cathodic polarization was measured at 700 - 900°C for pyrochlores and 800 - 1000°C for perovskites, respectively. Figure 8-1 shows the cathodic polarization curves for these electrodes. Table 8-1 summarizes the values of the cathodic overpotential. The lead pyrochlore shows excellent cathodic properties even at the low temperature of 800°C, and the overpotentials are comparable to the lanthanum cobalt perovskite. The bismuth ruthenium pyrochlore showed slightly higher overpotentials than the lead pyrochlore. However, both perovskites showed much higher overpotentials even at 1000°C than the pyrochlores.

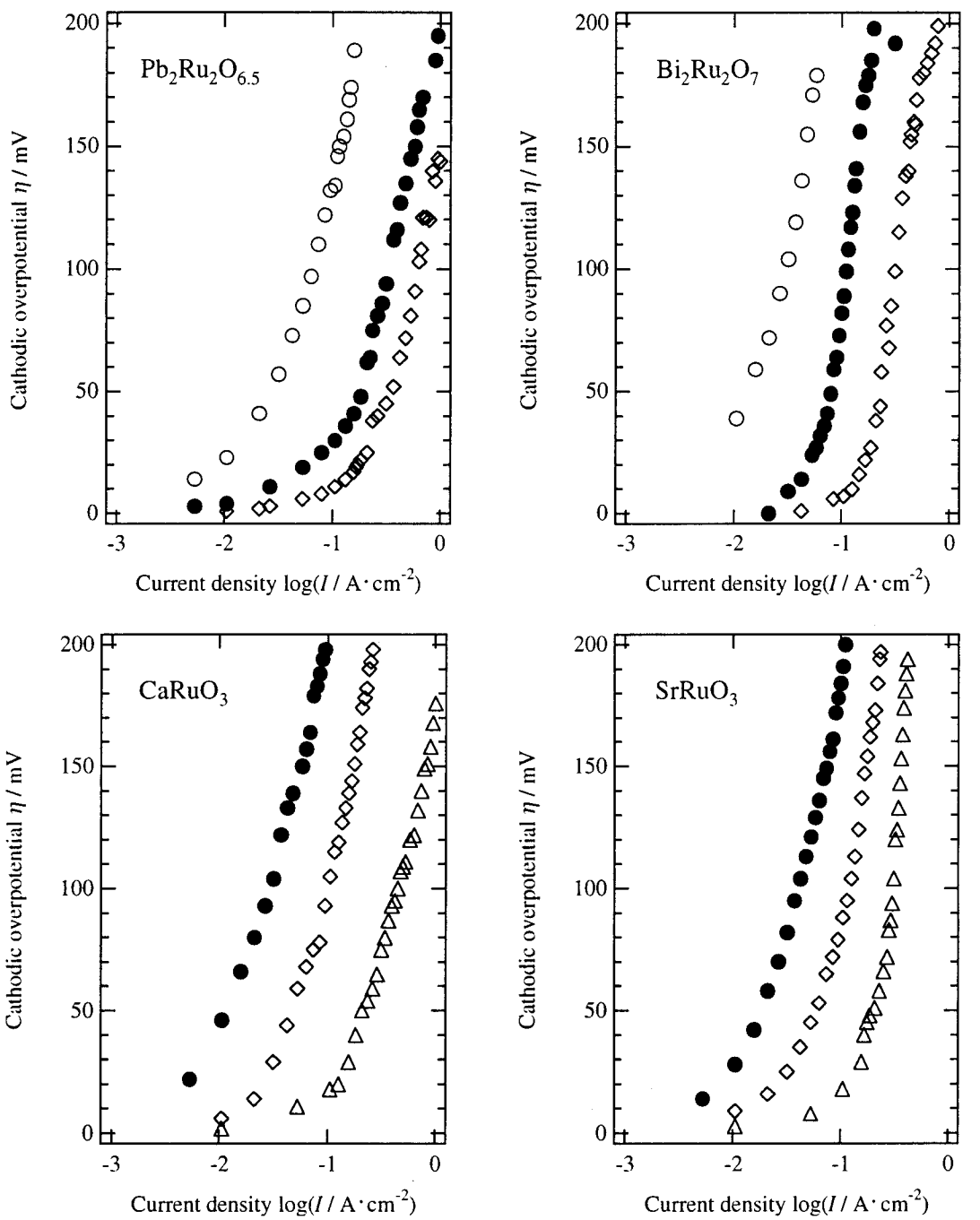

Fig. 8-1 Cathodic overpotential cureves for the ruthenium pyrochlores and perovskites.

○:700°C, ●:800°C, ◇:900°C, △:1000°C

Table 8-1 Cathodic overpotential (η / mV) of the pyrochlores and perovskits

The values of the overpotential are at a current density of 100 $mA \cdot cm^{-2}$.

Phase	700°C	800°C	900°C	1000°C
$Pb_2Ru_2O_{6.5}$	161	30	11	-
$Bi_2Ru_2O_7$	250	89	7	-
$CaRuO_3$	-	205	105	18
$SrRuO_3$	-	191	88	18
$La_{0.7}Sr_{0.3}CoO_{3-z}$ (2)	-	4	-	-
$La_{0.5}Sr_{0.5}MnO_{3-z}$ (2)	-	55	-	-

8-4 Electrical conductivity

Figure 8-2 shows the temperature dependence of the conductivity for the pyrochlores and perovskites measured from room temperature to 900°C in air. The samples show metallic behavior with almost temperature independent conductivity. The pyrochlores showed higher conductivity than the perovskites, with the highest conductivity of $\sigma = 10^2 - 10^3$ $S \cdot cm^{-1}$ for $Pb_2Ru_2O_{6.5}$. No significant changes in the conductivity curves in the temperature range examined indicated that no reaction or phase transition occur at high temperature. The conductivity value of the lead and bisumuth pyrochlores are comparable to those of the perovskites, $La_{1-x}Sr_xMnO_3$ (10^2 $S \cdot cm^{-1}$) and acceptable as cathodes in SOFC.

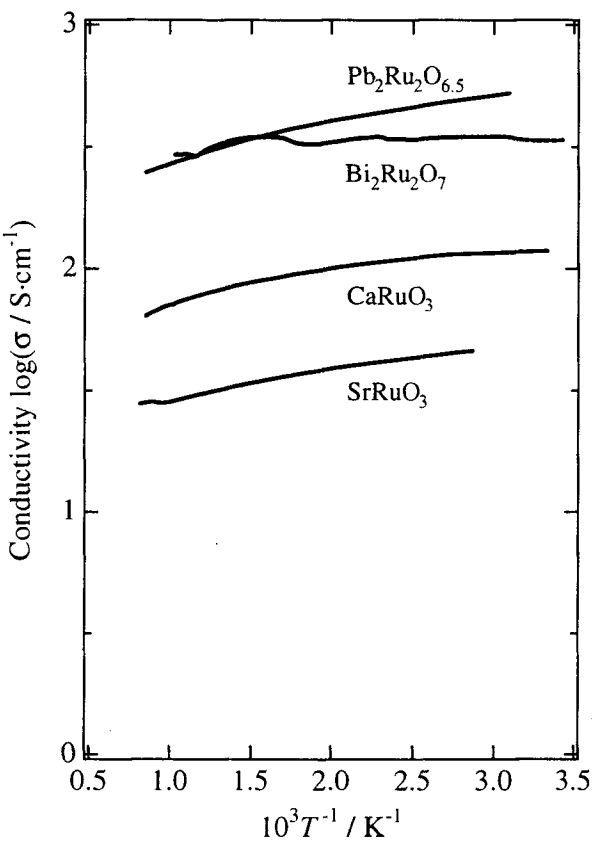

Fig.8-2 Temperature dependence of electrical conductivity for $Pb_2Ru_2O_{6.5}$, $Bi_2Ru_2O_7$, $CaRuO_3$ and $SrRuO_3$.

8-5 Reactivity

The reactivity tests of the pyrochlores and perovskites with 8YSZ were carried out for 96 h at 900 and 1000°C, respectively. Figure 8-3 shows the X-ray diffraction patterns of the pyrochlores with 8YSZ after being annealed at 900°C. No significant changes in the diffraction patterns for the lead pyrochlore were observed and are an indication of no reaction between the lead pyrochlore and 8YSZ. For bismuth pyrochlore, synthesis with the stoichiometric ratio of the starting materials leads to the samples containing an impurity phase ($Bi_{12}Ru_{0.15}O_{18.3}$). After the reaction test using

this sample, the monoclinic zirconia phase appeared. This might be caused by a reaction between the impurity phase and the yittria in the 8YSZ, and the cubic zirconia changed to a monoclinic phase. However, reaction using single phase pyrochlore, which was synthesized as $Bi_2Ru_{2.2}O_7$, led to no changes in the diffraction patterns.

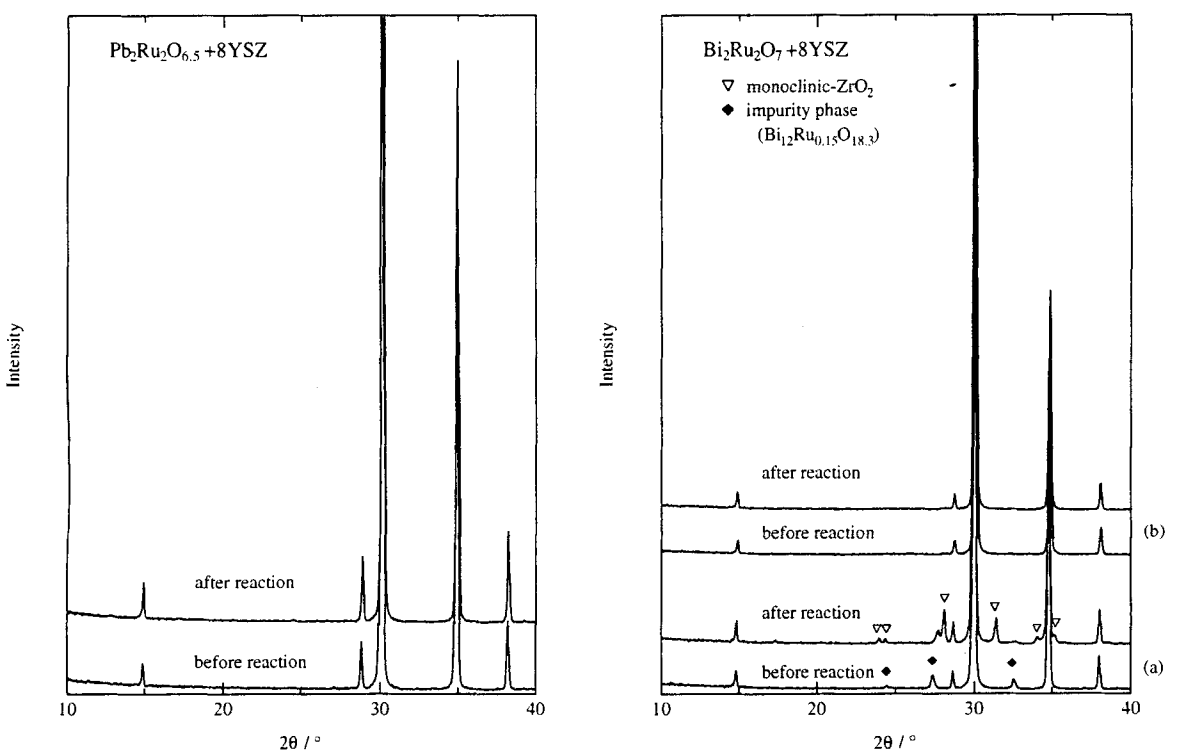

Fig. 8-3 X-ray diffraction patterns of a mixture of the pyrochlore and YSZ (lower), and the sample annealed at 900°C for 96 h (upper). For $Bi_2Ru_2O_7$, the sample with the pyrochlore containing impurity phase (a) and that with the single phase pyrochlore (b) are shown.

Figure 8-4 shows the X-ray diffraction patterns of a mixture of the perovskite and the 8YSZ at 1000 °C. For $SrRuO_3$, a small amount of the reaction product was observed, while no reaction was observed for $CaRuO_3$.

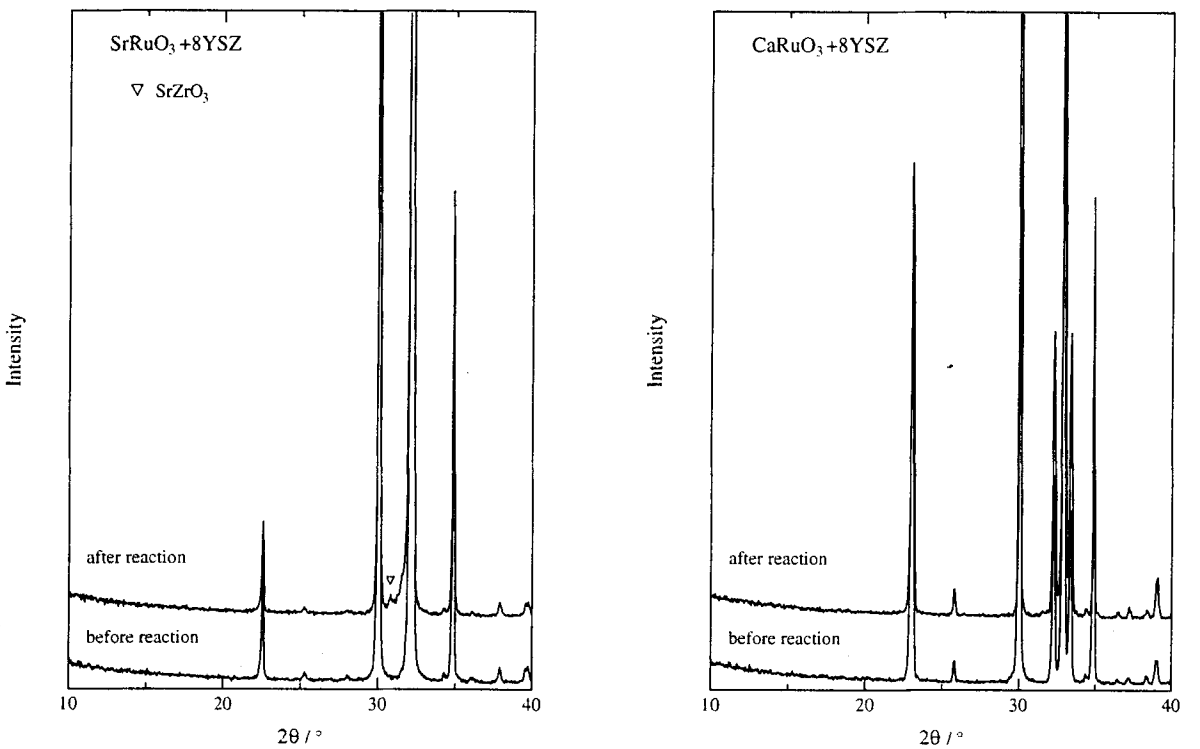

Fig. 8-4 X-ray diffraction patterns of a mixture of the perovskites and YSZ (lower), and the sample annealed at 1000°C for 96 h (upper).

8-6 Thermal expansion

Figure 8-5 shows the temperature dependence of the thermal expansion of the pyrochlores. The thermal expansion of 8YSZ is also indicated with a dashed line. The expansion of the pyrochlores is almost linear in the temperature range examined. The coefficient values of 0.99 - 1.00 x 10^{-5} K^{-1} for the bismuth pyrochlore at 700 - 900°C are almost comparable to those of 1.02 x 10^{-5} K^{-1} for the 8YSZ. On the other hand, the lead pyrochlore showed a slightly higher expansion coefficient of 1.10 - 1.21 x 10^{-5} K^{-1} at 700 - 900°C compared to the bismuth pyrochlore.

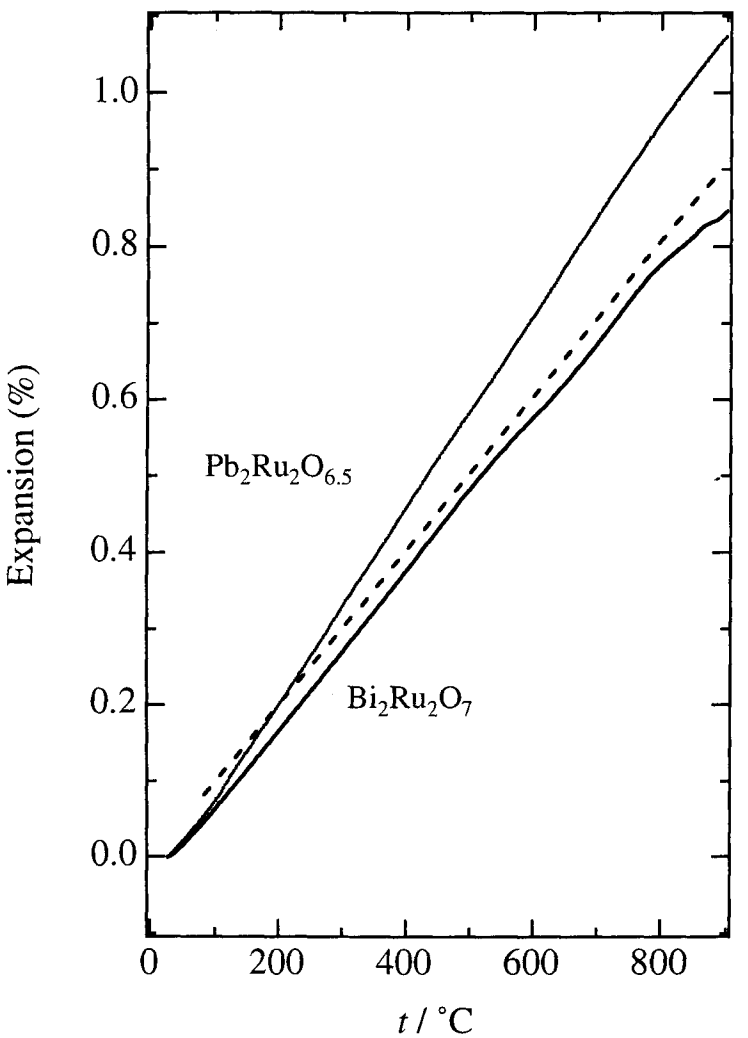

Fig. 8-5 The thermal expansion of $Pb_2Ru_2O_{6.5}$ and $Bi_2Ru_2O_7$. The expansion data of 8YSZ (-- - - --) is indicated as a comparison.

8-7 Conclusion

The lead and bismuth pyrochlores, $Pb_2Ru_2O_{6.5}$ and $Bi_2Ru_2O_7$, showed excellent cathodic polarization behavior for the SOFC electrode. These systems do not reacted with 8YSZ at 900°C and the thermal expansions of $Pb_2Ru_2O_{6.5}$ and $Bi_2Ru_2O_7$ are almost comparable to the 8YSZ.

$La_{1-x}Sr_xMnO_3$ and its related oxides have been intensively studied. For example, $Gd_{1-x}A_xMnO_3$ (A = Ca, Sr) from the viewpoint of controlling the reaction with YSZ [6], and $La_{1-x}Sr_xMnO_3$ with highly dispersed Pt microcrystal to enhance the catalytic activity at low temperature [7]. Furthermore, Sr and Ni doped $LaCoO_3$ and $LaFeO_3$ have been reported recently [8]. Although the ruthenium pyrochlores are unstable at high temperature, pyrochlore oxides are reported to form solid solution with rare earth [9, 10, 11], and the thermal expansion and thermal stability might be varied with the solid solution formation.

References

[1] B. C. H. Steel, Proc. 1st European SOFC Forum, p. 375 (1994)

[2] T. Ishihara, H. Matsuda, and Y. Takita, *J. Electrochem. Soc.*, **141**, 3444 (1994)

[3] Y. Takeda, R. Kanno, M. Noda, Y. Tomida, and Y. Yamamoto, *J. Electrochem. Soc.*, **134**, 2656 (1987)

[4] O. Yamamoto, Y. Takeda, R. Kanno, and M. Noda, Solid State Ionics, **22**, 241 (1987)

[5] O. Yamamoto, Y. Takeda, R. Kanno, and T. Kojima, in Solid Oxide Fuel Cells, S. C. Singhal, Editor, PV 89-11, p. 242, The Electrochemical Society Proceedings Series, Pennington, NJ (1989)

[6] O. Yamamoto, S. Watanabe, H. Ueno, N. Imanishi, Y. Takeda, N. Sammes, and M. B. Phillipps, in Solid Oxide Fuel Cells Ⅳ, Ed. M. Dokiya, O. Yamamoto, H. Tagawa, and S. C. Singhal (The Electrochemical Society), p. 415 (1995)

[7] H. Uchida, A. Tsuno, and M. Watanabe, *Denki Kagaku*, **64**, 686 (1996)

[8] K. Huang, H. Y. Lee, J. B. Goodenough, *J. Electrochem. Soc.*, **145**, 3220 (1998)

[9] R. Kanno, Y. Takeda, T. Yamamoto, Y. Kawamoto, and O. Yamamoto, *J. Solid State Chem.*, **102**, 106 (1993)

[10] T. Yamamoto, R. Kanno, Y. Takeda, O. Yamamoto, Y. Kawamoto, and M. Takano, *J. Solid State Chem.*, **109**, 372 (1994)

[11] H. Kobayashi, R. Kanno, Y. Kawamoto, T. Kamiyama, F. Izumi, and A. W. Sleight, *J. Solid State Chem.*, **114**, 15 (1995)

Chapter 9

Summary

In the present study, the iron-containing perovskites, and ruthenium-containing pyrochlores were synthesized under high pressure, and their structures and physical properties were investigated. Furthermore, ruthenium-containing pyrochlores and perovskites were studied as the cathode materials for SOFC.

In chapter 3, the solid solution $Ca_{1-x}Sr_xFeO_3$ which shows charge disproportionation (CD), $2Fe^{4+} \rightarrow Fe^{3+} + Fe^{5+}$, were studied. $Ca_{1-x}Sr_xFeO_3$ was synthesized under high oxygen pressure by using brownmillerite, perovskite $Ca_{1-x}Sr_xFeO_{2.5+\delta}$. Structural studies showed the bend of the FeO_6 octahedra connection increased from 160° to 180° with Sr substitution. These corresponded to semiconducting to metallic change, and CD behavior. CD was observed by slope change in electrical resisitivity and magnetic susceptibility measurements.

In chapter 4, the structural change in CD transition was clarified by low temperature neutron diffraction study. The structure changed from orthorhombic to monoclinic. The average iron-oxygen distances split into two, longer Fe(1)-O and shorter Fe(2)-O, which corresponded to the lower and higher oxidation states of iron.

In chapter 5, thallium pyrochlore $Tl_2Ru_2O_{7-\delta}$ was synthesized under high pressure, and two categories of electrical properties were found: metallic-semiconducting transition at 120K (high oxygen pressure synthesis), and metallic-semiconducting transition at 50K (high pressure synthesis). Neutron diffraction study clarified the compositions and structures for both samples. While a small amount of oxygen vacancy ($Tl_2Ru_2O_{6.96}$) was observed for the sample synthesized under high pressure, the stoichiometric composition ($Tl_2Ru_2O_7$) was found for the sample synthesized under high oxygen pressure. The metallic to semiconducting property changes corresponded to structural changes with the increase in Ru-O distance, the increase in O-Ru-O angle, the decrease in Ru-O-Ru angle, and the decrease in Tl-O distance.

In chapter 6, the structural change in metallic-semiconducting transition at 120 K was clarified by low temperature neutron diffraction study. The structure changed

from cubic to orthorhombic. The calculated average bond distances and valence bond sums indicated that thallium plays an important role in metallic-semiconducting transition.

In chapter 7, the spin-glass like behavior in ruthenium containing pyrochlore was studied. No structural change was found at the spin-glass transition. The spin-glas transition is derived from Ru tetrahedra, and the transition temperature decreased with increasing oxygen vacancy.

In chapter 8, ruthenium-containing pyrochlores and perovskites were studied as the cathode materials for SOFC. Ruthenium-containing pyrochlores, especially, $Pb_2Ru_2O_{6.5}$ showed excellent cathodic properties even at the low temperature of 800°C. Electrical conductivity, thermal expansion and reactivity also showed suitability for electrode except for stability at high temperatures.

Acknowledgement

The author would like to express his appreciation to Associated Professor Ryoji Kanno of Kobe University for his continuous guidance and valuable discussions on this thesis and wish to thanks Professor Yoji Kawamoto of Kobe University for his encouragement.

The author greatly wishes to thank Dr. Fujio Izumi of NIRIM for providing the program RIETAN for X-ray and neutron Rietveld analysis, and Dr. Takashi Kamiyama of University of Tsukuba, Dr. Alan W. Hewat of ILL, Dr. Brian J. Mitchell of IPNS for neutron powder diffraction measurements at KENS, ILL, and IPNS, and Mr. Kazuyoshi Sangen for high pressure synthesis.

The author especially wishes to thank Professor Mikio Takano of Kyoto University, Professor Arthur W. Sleight of Oregon State University, and Professor Yasuo Takeda of Mie University,

The author thanks to Dr. Masaki Azuma, Dr. Syuji Kawasaki, Mr. Takahiro Yamada of Kyoto University for Mössbauer and magnetic measurements, Mr. Jun Okamoto of Tokyo University for XPS measurement, Dr. Kazuyuki Kakuta of Aoyama Gakuin University for μSR measurement, and Mr. Fumiyuki Ishii of Hiroshima University for band calculation.

Finally, the author would like to express his sincere gratitude to his parents Mr. Kenji Takeda and Mrs. Katsumi Takeda, for their support, understanding, and encouragement.

Takashi TAKEDA

January 2000